PHYSICAL REVIEW D **80,** 124039 (2009)

Conformally curved binary black hole initial data including tidal deformations and outgoing radiation

Nathan K. Johnson-McDaniel,[1] Nicolás Yunes,[2] Wolfgang Tichy,[3] and Benjamin J. Owen[1,4]

[1]*Institute for Gravitation and the Cosmos, Center for Gravitational Wave Physics, Department of Physics, The Pennsylvania State University, University Park, Pennsylvania 16802, USA*

[2]*Department of Physics, Princeton University, Princeton, New Jersey 08544, USA*

[3]*Department of Physics, Florida Atlantic University, Boca Raton, Florida 33431, USA*

[4]*Max Planck Institut für Gravitationsphysik (Albert Einstein Institut), Callinstr. 38, 30167 Hannover, Germany*

(Received 7 July 2009; published 28 December 2009)

By asymptotically matching a post-Newtonian (PN) metric to two perturbed Schwarzschild metrics, we generate approximate initial data (in the form of an approximate 4-metric) for a nonspinning black hole binary in a circular orbit. We carry out this matching through $O(v^4)$ in the binary's orbital velocity v, and thus the resulting data, like the $O(v^4)$ PN metric, are conformally curved. The matching procedure also fixes the quadrupole and octupole tidal deformations of the holes, including the 1PN corrections to the quadrupole fields. Far from the holes, we use the appropriate PN metric that accounts for retardation, which we construct using the highest-order PN expressions available to compute the binary's past history. The data set's uncontrolled remainders are thus $O(v^5)$ throughout the time slice; we also generate an extension to the data set that has uncontrolled remainders of $O(v^6)$ in the purely PN portion of the time slice (i.e., not too close to the holes). This extension also includes various other readily available higher-order terms. The addition of these terms decreases the constraint violations in certain regions, even though it does not increase the data's formal accuracy. The resulting data are smooth, since we join all the metrics together by smoothly interpolating between them. We perform this interpolation using transition functions constructed to avoid introducing excessive additional constraint violations. Because of their inclusion of tidal deformations and outgoing radiation, these data should substantially reduce both the high- and low-frequency components of the initial spurious (''junk'') radiation observed in current simulations that use conformally flat initial data. Such reductions in the nonphysical components of the initial data will be necessary for simulations to achieve the accuracy required to supply Advanced LIGO and LISA with the templates necessary for parameter estimation.

DOI: 10.1103/PhysRevD.80.124039 PACS numbers: 04.25.dg, 04.25.Nx, 04.30.Db

I. INTRODUCTION

A. Motivation and overview of results

At present, several years after the initial breakthroughs in the evolution of binary black hole spacetimes [1–3], numerical relativity has matured to the point where successful binary black hole simulations are now commonplace (see, e.g., [4] for a review). Recent progress in the nonspinning case includes simulations of systems with mass ratios of up to 10:1 [5–7] and longer, more accurate simulations of equal-mass systems [8,9].

It is now time to consider what improvements need to be made to these simulations so they are accurate enough to provide gravitational wave detectors such as LIGO [10] with the model waveforms they need to detect and study binary black holes. The accuracy required of such waveforms has been studied by Lindblom, Owen, and Brown (LOB) [11]. Their results imply that current simulations are sufficiently accurate to supply the waveforms necessary for detection with either LIGO or LISA [12]. This conclusion is supported by the Samurai [13] and NINJA [14] projects, which indicate that currently used data analysis pipelines (including some not based on matched filtering) can detect a wide variety of numerical relativity waveforms at comparable levels in stationary Gaussian noise. The Samurai project also performs a more detailed comparison of a subset of waveforms for parameter estimation, and finds that—modulo possible systematic errors in sky position and arrival time—they are all indistinguishable if used for estimation of intrinsic parameters (i.e., not sky position or arrival time) at a signal-to-noise ratio (SNR) of less than 14 (25 if one eliminates the code that disagrees the most with the others).

However, Advanced LIGO may detect binary black hole signals with SNRs of order 100 [11]. According to LOB [11], if a waveform's phase error (suitably averaged in the frequency domain) is less than 0.007 radians, then it is suitable for use in parameter estimation with Advanced LIGO with such an SNR. But even the Caltech/Cornell group's simulations (which are arguably the most accurate yet) have maximum phase errors (in the time domain) of order 0.01 radians or more (see [8,15] for some discussion of their error budget). Converting such error measures to the criteria of LOB is more subtle than it looks, and we do not attempt it here. (See [16] for a discussion of some possible pitfalls, along with suggestions for successful

applications of the standards from LOB.) Nevertheless, it seems likely that even the Caltech/Cornell group's simulations may not satisfy the LOB conditions for parameter estimation, at least for binaries whose masses place the worst phase error in the detector's most sensitive frequency band.

All current binary black hole simulations incur some error from the initial data used. These data sets' lack of astrophysical realism is clearly announced by the burst of spurious (or junk) radiation present at the beginning of these simulations. This junk radiation is also responsible for various deleterious effects on simulations. First, one wastes the computer time required for the spurious radiation to propagate off the computational grid. Second, the system that remains after that time has been perturbed by the spurious radiation. This radiation's most prominent effect is to increase the binary's eccentricity,[1] though it also slightly increases the masses of the holes; see [20]. Additionally, in the unequal-mass or spinning cases, the initial junk radiation is emitted anisotropically, giving the system a small "kick" (see, e.g., [21,22]). The high-frequency component of the spurious radiation is a particular problem for spectral codes. For instance, the Caltech/Cornell group finds that the high-frequency component of the initial pulse of spurious radiation generates secondary spurious waves that propagate throughout the computational domain for two light-crossing times after the initial junk radiation has exited [8,15]. (These effects can be reduced, though by no means eliminated, by appropriate choices for the constraint damping parameters [23].)

Currently employed initial data's omission of significant features of the spacetime can also be seen analytically. Except for occasional tests of initial data (discussed in Sec. I B), all current simulations use initial data sets that assume *conformal flatness* (i.e., that the spatial metric is a scalar multiple of the flat 3-metric). The assumption of conformal flatness is convenient, since it allows one to get simple, mostly analytic expressions for initial data that exactly solve the constraint equations and include orbiting black holes (see, e.g., [24,25] for reviews).

In general, these sets are geared either towards the puncture or excision approaches. The majority of the community uses punctures, with initial data stemming from [26]. These data are very flexible, as they contain parameters with which one can directly set the momentum and spin of each hole. For instance, for evolutions with spinning holes, one can simply set these parameters using post-Newtonian (PN) results as in [27–30]. For nonspinning configurations in a circular orbit, parameter choices based on the assumption of a helical Killing vector [31,32] are possible as well. The Caltech/Cornell and Princeton groups use excision [33,34], with initial data constructed using the conformal thin-sandwich method (see, e.g., [35]). These data are slightly harder to construct than puncture data are, since one has to solve a larger number of elliptic equations. However, excision data have the advantage of a direct connection to the isolated horizon formalism [36], which allows one to construct holes with well-defined masses and spins. Additionally, the excision approach is applicable to a wider array of initial data construction methods: It is used in all of the extant evolutions of superposed black hole data sets except for one specifically tailored to the puncture approach. (See Sec. I B for a discussion of these evolutions.) The data we present here also require evolutions using excision or the turducken approach [37].

Conformally flat initial data cannot accurately represent some features of a binary black hole spacetime, since the PN metric for a binary system stops being spatially conformally flat at $O(v^4)$, where v is the binary's orbital velocity in units of c, the speed of light (see Sec. IV A for discussion). The order at which this fundamental disagreement with PN predictions first occurs gives a rough indication of the error committed in using conformally flat initial data. At present, the simulation for which this error is the smallest is the longest of the Caltech/Cornell runs (in [8]), for which $v_{\text{initial}} \simeq 0.24$, where v_{initial} is the binary's initial orbital velocity. We expect the initial data's conformal flatness to only affect the waveform at $O(v_{\text{initial}}^4)$, which for this run is comparable to the phase error allowed for a waveform to be used for parameter estimation with Advanced LIGO. It is thus possible (though perhaps not likely) that conformally flat initial data would be suitable for use in the simulations that will generate such waveforms.

It is unlikely that conformally flat initial data can be used to generate the waveforms required for parameter estimation with LISA. Here, the required (appropriately averaged frequency domain) phase accuracy is 2×10^{-4} radians [11], ~21 times smaller than v_{initial}^4 for the longest of Caltech/Cornell's simulations. One can reduce the error in the initial data by starting the simulation with a larger separation. However, $v_{\text{initial}}^4 \simeq 2 \times 10^{-4}$ implies an initial (PN coordinate) separation of ~71 times the binary's mass, and thus a merger time that is over 400 times as long as the Caltech/Cornell group's longest simulations to date, which start from a (PN coordinate) separation of ~15.3 times the binary's mass. It is thus necessary to improve the accuracy of the initial data. Evolutions of more accurate initial data will also give a direct measure of the errors introduced in using current, conformally flat initial data.

This paper provides initial data that include more of the physics present in the binary's spacetime than any previous constructions. (For technical simplicity, we specialize to a nonspinning binary in a circular orbit. However, the construction generalizes straightforwardly to include either eccentricity or spin, though the algebraic complexity increases substantially, and not all the pieces are available in

[1] In practice, the eccentricity can be reduced by various means [17–19].

the spinning case to carry out the construction to the same order we have done here; see the discussion in Sec. IX B.) In particular, our data's accurate description of certain properties of the spacetime should substantially reduce *both* components of the aforementioned spurious radiation. These two components are thought to come from different physical effects. The long-wavelength component is thought to correspond to the initial data's lack of outgoing gravitational radiation, whose wavelength would be somewhat longer than the orbital separation. Of course, one expects the junk to be generated predominantly in the strong-field region near the holes, where the binary's gravitational radiation cannot be disentangled from the rest of its gravitational field. However, one also expects the pieces that one wants in the strong-field region to appear at $O(v^4)$, just as the true gravitational waves do in the radiation (or far) zone (defined in Sec. II); see Sec. IV B for some discussion. Our data include all the $O(v^4)$ terms in the strong- and weak-field regions. The short-wavelength component is thought to come from the holes' quasinormal modes ringing down, emitting gravitational radiation with wavelengths on the order of their masses, as they relax from their initial, close to spherical state to their desired tidally deformed state (see, e.g., [15]). Our data include the Newtonian quadrupole and octupole tidal deformations each hole induces on the other, as well as the 1PN corrections to the quadrupole deformations.

The tidal deformations are contained in perturbed Schwarzschild metrics, given (in the horizon-penetrating coordinate system we use) in Eqs. (3.2) and (3.3). The tidal fields are fixed by asymptotically matching these Schwarzschild metrics to an $O(v^4)$ PN metric, given in Eq. (4.1); expressions for the tidal fields around hole 1 are given in Eq. (B1). One also needs to introduce a coordinate transformation in order to put the black hole metrics in the same coordinate system as the PN metric. This transformation is also determined (perturbatively) by the matching; instructions for putting it together around hole 1 are given in Sec. V G. Instructions for converting all of these results to the region around hole 2 are given at the beginning of Sec. V A.

The PN metric mentioned above treats retardation perturbatively and thus becomes inaccurate far from the binary. In that region, we thus use a version of the PN metric that includes retardation explicitly (but also uses a multipolar decomposition, so it does not provide the desired accuracy closer to the holes). This metric is given in Eq. (6.4). Because of retardation, one needs to know the binary's past history accurately in order to obtain the far zone metric accurately far from the binary. This past history is computed in Sec. VI A to the highest PN order possible with current results. The contributions of these terms are of equal or higher order than some of our uncontrolled remainders, but their inclusion is necessary if one wishes to obtain, e.g., accurate phasing for the outgoing radiation.

We have also added other formally higher-order terms to the metrics, including all the readily available PN results, along with a resummation of the black hole backgrounds in the PN metric. We found that some of these terms improved the constraint violations in various regions; others of these additional terms are expected to improve evolutions of the data. The resummation is given in Sec. VIII A; all the remaining higher-order terms are discussed in Sec. VII.

The transition functions that we use to stitch the metrics together smoothly are given in Sec. VIII B. These functions satisfy the hypotheses of the two so-called Frankenstein theorems [38]; this guarantees that the resulting initial data will have constraint violations whose formal order is no larger than that of the constraint violations of the initial data obtained from the constituent metrics. In particular, the first theorem guarantees that the merged metric satisfies the Einstein equations to the same formal order as its constituent metrics, provided that the derivatives of the transition functions satisfy certain sufficient conditions (given in Sec. VIII B). The second theorem shows that the same conditions are sufficient to guarantee that the differences between an initial data set obtained from the merged 4-metric and one constructed by merging the initial data sets obtained from the constituent 4-metrics are contained in the uncontrolled remainders. (We followed the latter approach in obtaining the initial data used to generate the plots, but it is also possible to use the former approach and obtain initial data from our merged 4-metric directly. We also carried out the requisite differentiation numerically: The expressions for the relevant metrics are too complicated to make analytic expressions for the initial data practicable.) See Appendix D for the technical details of how we compute the metrics.

We have generated MAPLE scripts and *C* code (available at [39]) that produce initial data for a nonspinning binary in a quasicircular orbit. This binary can, in principle, have any mass ratio and initial separation, though the data will decrease in accuracy as the initial separation decreases, and will also likely lose accuracy as the mass ratio increases. (We expect the latter to occur, since there is evidence that the PN approximation converges more slowly for extreme mass ratios than for equal mass ratios; see, e.g., [40,41]. Additionally, the transition functions we give do not behave quite as well as might be desired for unequal mass systems.) We suggest using initial separations of less than about $10m$ (m is the binary's mass) with caution and strongly recommend using larger initial separations if at all possible: The data's constraint violations decrease dramatically with increasing initial separation, as discussed in Sec. VIII C; we expect a concomitant increase in the data's physical accuracy.

The constraint violations give a measure of how much more accurate this paper's data are compared with those constructed in previous papers (viz., [42,43], which we refer to as Papers I and II). We plot the constraint violations

of the three sets of data in Fig. 1. [See, e.g., Eqs. (14)–(15) in [24] for expressions for the constraint equations.] *Nota bene* (N.B.): While the Hamiltonian constraint violations of this paper's data are larger close to the hole than those of either of the previous papers' data, this is due to our inclusion of the full time dependence of the tidal fields, as discussed in Appendix D 1; the motivation for doing this, even at the cost of larger constraint violations, is given in Sec. VII. If one does not include these higher-order terms, then the new data's constraint violations are smaller close to the hole than those of either of the previous papers' data. See Sec. VIII C for a comparison of the constraint violations of the inner zone metric with and without full time dependence in the tidal fields.

For a simple, quantitative comparison of the overall constraint violations, we can consider their L^2 and sup norms. These are presented for all three sets of data in Table I and show, as expected, that the new data have smaller overall constraint violations than either of the previous papers' data. Of course, the L^2 norm of the new data's Hamiltonian constraint violations is only very slightly less than that of the data from Paper II, but this is probably to be expected; see Sec. VIII C for some discussion of this, as well as further details about the comparison plot and table.

B. Conformally curved initial data

The problems with conformally flat data have inspired a variety of constructions of conformally curved binary black hole data, for which there are two general approaches. One approach—the one we have taken—is primarily motivated by a desire for astrophysical realism, seeing the spurious radiation as an indicator of the failure of conformally flat initial data to model the desired spacetime accurately enough. These constructions so far have restricted their attention to nonspinning binaries and used the PN approximation to include the binary's physics. (Of course, true astrophysical binaries are expected to have significant spins, so the consideration of nonspinning binaries is merely a technical convenience appropriate for initial attempts at constructing astrophysically realistic data.) The other approach is primarily concerned with reducing the junk radiation in practice with relatively simple choices for initial data (viz., a superposition of boosted black holes). This approach is often geared primarily towards spinning black holes, since the amount of spurious radiation increases with the spin of the holes. (This is due to the nonexistence of a conformally flat slicing even of an isolated Kerr black hole with nonzero spin; see [44,45].)

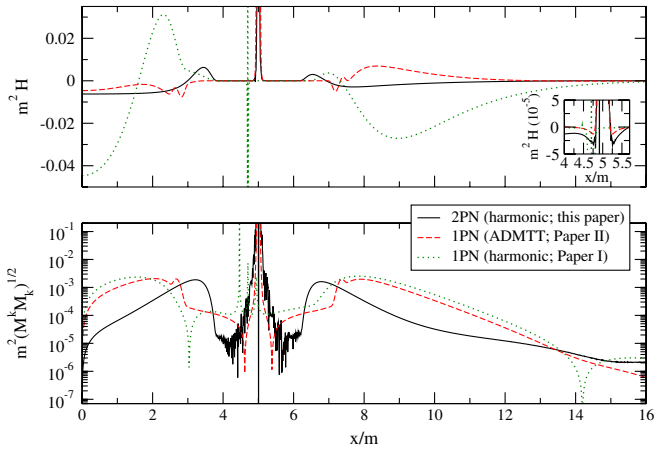

FIG. 1 (color online). The Hamiltonian constraint and norm of the momentum constraint along the x axis around hole 1 for this paper's data along with the data from Papers I and II. (In the norm of the momentum constraint, the index is raised using the metric in question.) All of these were computed for an equal-mass binary with a coordinate separation of 10 times its total mass, m. In the inset, we zoom in to show how the Hamiltonian constraint violations behave close to the horizon. Note that the data from Paper II are in a different coordinate system throughout, and that the black hole background in Paper I's data is in a different (and not horizon-penetrating) coordinate system.

Besides our present work, other constructions in the first category are this work's antecedents ([42,43,46], discussed in the next subsection), along with the approaches of Nissanke [47] and Kelly *et al.* [48]. (The latter two only use the PN approximation in their construction, so the resulting data cannot accurately describe the spacetime near the holes.) Nissanke, building on the work of Blanchet [49] (who constructed initial data for a head-on collision of initially stationary holes), obtains explicit analytic expressions for the 3-metric and extrinsic curvature from the 2PN metric. (N.B.: These constructions only use the version of the PN metric that treats retardation perturbatively, so the resulting data rapidly lose accuracy away from the binary.) Kelly *et al.* [48] extend the work of Tichy *et al.* [50] to give initial data from the 2.5PN Arnowitt-Deser-Misner transverse-traceless (ADMTT) metric that are valid through $O(v^4)$ wherever the PN approximation is and thus contain the binary's outgoing radiation in the far zone. (See Sec. IV B for a discussion of why gravitational radiation is present at that order.) In order to obtain these data, they have to evaluate an integral numerically, so their data are not completely analytic.

The most recent progress in the second category for nonspinning black holes is Lovelace's [51] construction and evolution of superposed Schwarzschild data for an orbiting binary. (There is a companion construction and evolution of superposed spinning black hole data for an orbiting binary in Lovelace *et al.* [52]. Additionally, two versions of the spinning data are evolved in head-on collisions in [22].) Lovelace uses the superposed black hole data as free data for a constraint solver and finds that the resulting data produce less spurious radiation than conformally flat data. There are also older constructions in a similar vein [53–55], though their data have only been

TABLE I. The L^2 and sup norms (denoted by $\|\cdot\|_2$ and $\|\cdot\|_\infty$, respectively) of the Hamiltonian and momentum constraints (H and $\vec{M}$) for an equal-mass binary with a coordinate separation of 10 times its total mass, m. (The norms of the momentum constraint include the L^2 3-vector norm $\sqrt{M^k M_k}$, where the index is raised using the metric under consideration.) These are computed along the x axis outside the unperturbed horizons of the holes but inside the interval $[-16.4m, 16.4m]$.

	$m^{3/2}\|H\|_2$ (10^{-2})	$m^2\|H\|_\infty$ (10^{-2})	$m^{3/2}\|\vec{M}\|_2$ (10^{-3})	$m^2\|\vec{M}\|_\infty$ (10^{-3})
This paper	1.565	0.631	2.973	1.879
Paper II	1.566	0.758	4.627	2.065
Paper I	9.149	4.466	5.837	2.531

evolved in head-on collisions without first solving the constraints [56] and did not reduce the spurious radiation. Hannam *et al.*'s Kerr puncture data [57] have been evolved, and found to reduce the spurious radiation, but they are only applicable to head-on collisions. Neither of the other conformally curved spinning data constructions [58,59] have been evolved, to our knowledge.

While several of the superposed data sets have been evolved, the only evolution of PN initial data of which we are aware is that of Kelly *et al.* [60]. They evolved the data they obtained in [48] (as well as the original version without waves from [50]) and found that the junk radiation was indeed reduced, compared to standard puncture data. However, as expected, the spurious radiation appears to be unchanged when the waves are added: We expect the junk to be generated primarily near the holes, and both data sets have the same accuracy in the strong-field region. In addition, Kelly *et al.* only find a reduction in the low-frequency component of the spurious radiation. This is again as expected, since their data do not include the tidal deformations on the holes.

As mentioned in the previous subsection, the data set we construct here should help reduce both components of the junk radiation, since it includes an accurate description of the spacetime near the holes (including the quadrupole and octupole tidal deformations), matched to the PN metric through $O(v^4)$. We also offer an extension to these data that are accurate through $O(v^5)$ in the PN portions of the time slice (i.e., not too close to the holes), allowing our data to be compared more directly with Kelly *et al.*'s.

C. Specifics of our approach and its relation to other work

With currently available technology, if one wishes to generate initial data that include the holes' tidal deformations or the binary's outgoing radiation, it is necessary to allow the initial data (as first constructed) to be merely an approximate solution of the constraint equations. (One can always use these approximate data as free data for a constraint solver and thus obtain an exact solution of the constraints, to numerical precision.) Since the post-Newtonian approximation has been developed to a very high order, it is an obvious choice for the description of the binary's spacetime. Indeed, an explicit expression for the metric to 2.5PN order (with a perturbative treatment of retardation) is given by Blanchet, Faye, and Ponsot (BFP) [61].

However, one cannot obtain accurate initial data throughout a time slice of the binary's spacetime using just the PN metric, since the PN approximation breaks down near the holes; the PN approximation is a weak-field approximation (due to the post-Minkowskian iteration in powers of G, Newton's gravitational constant), in addition to being a slow-motion approximation (the post-Newtonian expansion proper, which formally proceeds as an expansion in $1/c$, where c is the speed of light). Moreover, the standard PN approximation (as presented, e.g., in BFP) treats retardation perturbatively. It thus becomes inaccurate quite rapidly as one enters the radiation zone (i.e., when one is further than about a reduced gravitational wavelength away from the binary's center of mass).

The resolution of both of these problems is to realize that there is an appropriate approximate description of the spacetime in each of the regions where the standard PN metric breaks down: Near each of the holes, in the regions known as the *inner zones*, spacetime is well described by a perturbed black hole metric. (These zones, as well as the others we mention here, are defined more precisely in Sec. II.) In the radiation zone (or *far zone*), there is another version of the PN metric that incorporates retardation nonperturbatively. These are all readily available in the literature to the order we need them; see Sec. I C 1 for the details.

One then has to stitch all of these spacetimes—the far zone, inner zones, and the *near zone* where the standard PN metric is valid—together into one global approximate metric. (Of course, this metric will be global in space, but not in time—i.e., it will only be accurate in a temporal neighborhood of a time slice of the binary's spacetime.) This stitching together proceeds in two steps: First, one uses the technique of matched asymptotic expansions to match the metrics at a formal level. This puts all the metrics in the same coordinate system (up to uncontrolled

remainders) and fixes any previously undetermined parameters (e.g., the holes' tidal perturbations) so that the metrics are asymptotic to each other in their regions of mutual validity (the *buffer zones*). The final, numerical merging of the metrics is then effected by *transition functions* that smoothly interpolate between the metrics in their mutual buffer zones. The resulting merged metric is guaranteed to satisfy the Einstein equations to the same order as its constituent metrics if the transition functions are constructed to satisfy the hypotheses of the so-called Frankenstein theorems [38]. (We check that our transition functions satisfy these hypotheses in Sec. VIII C.)

Once one has obtained such approximate initial data, it is, of course, possible to use them as the input to a numerical constraint solver, and thus obtain an exact solution, to numerical precision. In fact, it is probably desirable to do so. The idea when doing this is that if the input to the constraint solver satisfies the constraints and describes the desired physics to some reasonably good tolerance, then the "exact" solution one obtains after solving the constraints will not differ too much from the input in its physical content. This is probably true regardless of how one chooses to produce the exact solution to the constraints, as long as the procedure modifies the initial guess in a reasonable way. One commonly used procedure is the York-Lichnerowicz decomposition [24]. Both Pfeiffer *et al.* [62] and Tichy *et al.* [50] have implemented this numerically without the assumption of conformal flatness. However, it is unclear exactly how the output from the York-Lichnerowicz procedure (or similar decompositions) relates to its input in physical content. It may thus be preferable to project the approximate initial data onto the closest "point" on the constraint hypersurface (as measured by some appropriate norm), possibly using the results of [63].

If one chooses to evolve without solving the constraints (as did Kelly *et al.* [60]), then one will not have a true vacuum evolution: The constraint violations will act as matter (which may not satisfy any of the standard energy conditions). For instance, Bode *et al.* [64] investigated the evolution of initial data that only approximately satisfied the Hamiltonian constraint (though the momentum constraint was satisfied exactly). They found that the holes accreted the negative Hamiltonian constraint violations that surrounded them, decreasing their masses.

1. Comparisons with similar constructions

All three of the previous constructions of matched initial data restricted their attention to the simplest case of nonspinning holes in a (quasi)circular orbit, as we do here: Alvi [46] made the first attempt, though his data were found to be unsuitable for numerical evolutions [65]. Yunes *et al.* [42] (Paper I) then revisited the problem, correcting various deficiencies in Alvi's method. Yunes and Tichy [43] (Paper II) then obtained a better numerical match (in the sense of smaller constraint violations) by using ADMTT PN coordinates (as opposed to the harmonic coordinates of all the other constructions) and some resummation. They also constructed horizon-penetrating coordinates to provide the first usable initial data constructed using this method. However, in all of these cases the initial data are only valid through $O(v^2)$, and the tidal fields are still just the lowest-order quadrupole ones Alvi had obtained.

The present calculation builds on all of these previous constructions, computing fully matched initial data through $O(v^4)$, in order to include the pieces of the PN metric that break conformal flatness (and contain gravitational radiation), and reading off the tidal fields from the matching. In addition, we include the radiation zone portion of the metric. This was done explicitly by Alvi and implicitly in Paper II, due to its use of the ADMTT PN metric, though neither of them included the effects of radiation reaction on the binary's past evolution in their far zone metric, as we do. We also employ background resummation (discussed in Sec. VIII A) in the near zone metric, inspired by similar resummations in Paper II. Additionally, we stay in inertial coordinates, while all of the previous versions use a corotating coordinate system.

While we only obtain fully matched initial data through $O(v^4)$, we actually have to carry out the matching of the 4-metric through $O(v^5)$ in order to do so: We need to match the $O(v^5)$ pieces of the spatiotemporal components of the 4-metrics in order to obtain the extrinsic curvature consistently [see the discussion after Eq. (2) in Paper I], and one needs to carry out the matching of all the components in order to obtain the $O(v^5)$ piece of the coordinate transformation.

Additionally, while our goal was simply to keep terms of quadrupole order overall in the multipole expansion, as was done previously, we found that it was necessary to match the lowest-order octupole pieces in order to match the 1PN corrections to the quadrupole pieces consistently. This is discussed in Sec. V A. In fact, we have carried out the matching of quadrupole pieces to the highest possible order to which it can be done consistently without the inclusion of the hexadecapole tidal fields. (These hexadecapole pieces can be included with input from nonlinear black hole perturbation theory, since carried out by Poisson and Vlasov [66].) We also obtained the 1PN correction to the electric octupole and the associated piece of the coordinate transformation as a further application of our matching procedure. However, we could not obtain the other $O(v^4)$ octupole pieces in the initial data (since they include the hexadecapole tidal fields), so our knowledge of these corrections does not allow us to increase the formal order to which our data are valid.

Building on the work done in Paper II, we have used horizon-penetrating coordinates for the black holes from the outset. This requirement of horizon penetration is necessary for numerical purposes. The coordinates need to be regular and the lapse positive in a neighborhood of the horizon: Even though the spacetime near the singularity will be excised or filled with matter, one needs to be able to evolve at least a small portion of the spacetime inside the horizon.

At the same time, we want the coordinates for the black hole and PN metric to agree as closely as possible before the matching has been performed; close agreement makes for simple matching algebraically and improves the numerical agreement of the resulting matched metrics, as was seen in Paper II. Ideally, the coordinates would agree exactly for an unperturbed black hole, though this is not compatible with the requirement of horizon penetration unless one transforms the PN metric's coordinates: Standard PN coordinates (harmonic or ADMTT) are not horizon penetrating. We decided to avoid the complications such a transformation would entail and thus attempted instead to obtain agreement between the two coordinate systems to as high a PN order as possible.

These desiderata are satisfied if we use the fully harmonic version of Cook-Scheel coordinates [67] for the black hole and standard (PN) harmonic coordinates for the PN metric[2]: Cook-Scheel coordinates are horizon penetrating, and in their fully harmonic version only differ from PN harmonic coordinates for an unperturbed Schwarzschild black hole at $O(v^4)$. See Appendix A for an explicit comparison. This agreement was the best of any of the horizon-penetrating coordinate systems present in the literature we consulted (even if we also consider ADMTT coordinates for the PN metric). Of course, we then adjust this coordinate system perturbatively so it agrees with the near zone coordinate system to the order we have matched. However, we have checked that this adjustment does not affect the coordinates' horizon penetration.

The other choices for our ingredients were made for computational ease. We selected Detweiler's perturbed black hole metric [68] instead of Poisson's [69], because Detweiler expresses the tidal fields in the Thorne-Hartle-Zhang (THZ) harmonic specialization of locally inertial coordinates [70,71]. This gauge choice agrees better with the PN metric in harmonic coordinates than does Poisson's light-cone gauge. For the far zone, the results from the direct integration of the relaxed Einstein equations (DIRE) approach were the obvious choice: Pati and Will [72,73] give an explicit recipe for computing the far zone metric to the order we need it (which, in the extension, is higher than the order to which Alvi [46] gives it), along with all of the necessary ingredients (except for a few that can be obtained from Will and Wiseman [74]). Even more conveniently, their expression is in the same (harmonic) coordinate system as BFP's PN metric, so we do not have to determine a coordinate transformation for the matching between the near and far zones. [We have checked explicitly that the near and far zone metrics match through $O(v^5)$ in all components.] One also needs to know the binary's past history in order to obtain the far zone metric accurately, due to retardation: We calculate this in the PN approximation using Blanchet's results [41].

2. Comparison with Taylor and Poisson's determination of the tidal fields

Our method for determining the tidal fields can be compared and contrasted with that employed in the recent calculation by Taylor and Poisson [75]. Most importantly, Taylor and Poisson's aims are more general: Their calculation matches a single nonrotating black hole to an arbitrary 1PN metric (expressed in terms of potentials). Our results extend to higher orders (particularly in the spatial components of the coordinate transformation) but are restricted to the case of a (post-Newtonian) binary in a (quasi)circular orbit. However, the pieces that we both computed agree exactly. See Appendix B 1 for a comparison, including explicit expressions for the tidal fields we obtained.

The details of the calculations share some similarities (e.g., both use THZ coordinates for the perturbation), though the primary methods of determining the tidal fields differ substantially. Most importantly, Taylor and Poisson specialize the coordinate transformation and perform a decomposition of the potentials before matching. Our approach is more "brute force," requiring no such specialization or decomposition, but relying heavily on the computer algebra system MAPLE and the associated tensor manipulation package GRTENSORII [76]. See Sec. V A for a detailed presentation of our algorithm.

D. Structure of the paper

We begin by giving an overview of asymptotic matching in Sec. II and then present the inner and near zone metrics to be matched in Secs. III and IV, respectively. In Sec. IV, we also consider two relevant aspects of the PN metric, viz., conformal flatness breaking and gravitational radiation effects. Next, we discuss the specifics of our matching

[2]We use the term *harmonic coordinates* to refer to *any* coordinates x^α that satisfy $\nabla_\alpha \nabla^\alpha x^\beta = 0$, not just PN harmonic coordinates. (Here, ∇_α is the covariant derivative associated with the metric under consideration, and indices are raised using that metric.) For an unperturbed Schwarzschild black hole of mass M, PN harmonic coordinates are obtained by transforming the Schwarzschild radial coordinate $\mathcal{P}$ to $R_{\rm PN} = \mathcal{P} - M$ and thus retain the coordinate singularity at the horizon present in Schwarzschild coordinates.

procedure and read off the matching parameters and coordinate transformation order-by-order in Sec. V. We compute the far zone metric in Sec. VI, where we also discuss the PN results we use to obtain the effects of radiation reaction on the binary's evolution. In Sec. VII, we give an overview of the construction of an extension of this data set that is valid through $O(v^5)$ in the near and far zones, in addition to including various other higher-order terms. Then, we stitch the metrics together numerically in Sec. VIII, first resumming the near zone metric to improve its strong-field behavior (and thus the numerical agreement of the metrics), then constructing transition functions to stitch all of the metrics together smoothly, and finally considering the constraint violations of the resulting merged metric. Lastly, we conclude and summarize in Sec. IX.

We present various ancillary results and technical details in the appendices: Appendix A compares Cook-Scheel and PN harmonic coordinates. We provide explicit expressions for the tidal fields and some related discussion in Appendix B, along with the calculation of the fourth-order pieces of the octupole tidal fields and the polynomial part of the associated coordinate transformation. In Appendix C, we give the details of our calculation of the far zone metric used in the higher-order extension to the data, and in Appendix D the precise details of how the metrics are implemented numerically.

E. Notation and conventions

Units: We use geometrized units with $G = c = 1$ almost exclusively. (G is Newton's constant, and c is the speed of light.) The only exception to this comes when we are describing certain post-Newtonian expansions. Here, in keeping with the standard formal approach to the post-Newtonian approximation (see, e.g., [41]), we shall use G and $1/c$ as convenient bookkeeping parameters. For instance, we may refer to some term as being $O(c^{-n})$, or describe an expansion as proceeding in powers of G, though we shall not display these constants in any other context.

Binary parameters: The binary's orbital velocity is v, its orbital angular velocity is ω, and its coordinate separation is b. The masses of the holes are m_1 and m_2; their total mass is $m := m_1 + m_2$.

Indices: We use the standard convention that Greek letters denote spacetime indices, while lowercase Roman letters denote spatial indices. The uppercase indices A and B label the holes, as well as (by extension) the zones into which we divide the data's time slice. We use Q to denote a multi-index [see, e.g., the discussion following Eq. (2.14) in Pati and Will [72] for a definition].

Index operations: Except where otherwise noted (e.g., in Secs. IV A, VI, and VIII), spacetime indices are raised and lowered using the Minkowski metric $\eta_{\alpha\beta}$, so spatial indices are raised and lowered using the Kronecker delta δ_{kl}. We may even freely raise and lower spatial indices within expressions for notational convenience, particularly in Sec. IV. The summation convention is always in force, and may even be applied to spatial indices that are at the same level, particularly in Sec. VI. Parentheses, square brackets, and angle brackets on indices denote symmetrization, antisymmetrization, and the symmetric trace-free projection, respectively. We use vertical bars to exclude indices from these operations. The notation "$+(1 \leftrightarrow 2)$" denotes that the preceding expression is to be added to itself with the labels 1 and 2 switched.

Arrays: In addition to the ordinary three-dimensional Kronecker delta, we also define a "lowered four-dimensional Kronecker delta," $\Delta_{\alpha\beta} := \mathrm{diag}(1, 1, 1, 1)$. Our conventions for the three- and four-dimensional Levi-Civita symbols ϵ_{klp} and $\epsilon_{\alpha\beta\gamma\delta}$ are that $\epsilon_{123} = \epsilon_{0123} = 1$.

Metrics: As is usual, $\eta_{\alpha\beta}$ denotes the Minkowski metric; our signature is $(-, +, +, +)$. In Secs. IV and V (and Appendix B) $g_{\alpha\beta}$ denotes the near zone (PN) metric, and $h_{\alpha\beta}$ denotes the inner zone (perturbed black hole) metric. In Sec. VIII A and Appendix A, $g_{\alpha\beta}$ (sometimes with decorations) is also used for the unperturbed Schwarzschild metric. In Sec. VI (and the associated Appendix C), $g_{\alpha\beta}$ denotes the far zone metric, and $h_{\alpha\beta}$ its associated metric perturbation.

Coordinates: Cook-Scheel coordinates (used in the inner zone) are $X^\alpha = (T, X^k) = (T, X, Y, Z)$, with $R := \sqrt{X_k X^k}$. PN harmonic coordinates (used in the near and far zones) are $x^\alpha = (t, x^k) = (t, x, y, z)$, with $r := \sqrt{x_k x^k}$; r^α denotes just the spatial coordinates [i.e., $r^\alpha = (0, x^k)$]. Unit vectors are denoted by "hats." For instance, $\hat{t}^\alpha$, $\hat{x}^\alpha$, $\hat{y}^\alpha$, and $\hat{z}^\alpha$ are the Cartesian PN coordinate basis vectors corresponding to indices 0, 1, 2, and 3, respectively. We also define "tilded" coordinates $\tilde{x}^\alpha := x^\alpha - (m_2/m) b \hat{x}^\alpha$, $\tilde{x} := x - (m_2/m) b$, $\tilde{r} := \sqrt{\tilde{x}_k \tilde{x}^k}$, and $\tilde{r}^\alpha := r^\alpha - (m_2/m) b \hat{x}^\alpha$. Spatial vectors (or the spatial parts of spacetime vectors) will be denoted either with an arrow or a spatial index.

Norms: The Euclidean norm for spatial vectors is denoted by $\| \cdot \|$ (so, e.g., we could write the definition of R above as $R := \|\vec{X}\|$).

Derivatives: All partial derivatives are taken with respect to harmonic PN coordinates, so $\partial_\alpha := \partial/\partial x^\alpha$. Overdots on the tidal fields denote differentiation with respect to Cook-Scheel time T, but all other overdots denote differentiation with respect to PN harmonic time t. We use the shorthand $\partial_{\alpha\beta} := \partial_\alpha \partial_\beta$.

Order notation: We use $(\cdot)_j$ to denote the coefficient of $(m_2/b)^{j/2}$ in the (asymptotic) power series expansion of its argument. As discussed in Sec. V A, this includes multipoles through octupole order for $j \in \{2, 3\}$ but only through quadrupole order for $j \in \{4, 5\}$. (In principle, we

include all of the multipoles for $j \in \{0, 1\}$, since there are only monopole contributions.) Similarly, $(\cdot)_{j,n}$ and $(\cdot)_{j,\leq n}$ denote the 2^nth multipole-order and multipoles-up-to-2^n-order pieces of $(\cdot)_j$, respectively.

Polynomial and nonpolynomial parts: The superscripts P and NP denote the polynomial (in $\tilde{x}^\alpha$) and nonpolynomial parts of the object to which they are attached. See Sec. V A for a more precise definition of the nonpolynomial part.

References: [42,43] will be referred to as Papers I and II, respectively.

II. ASYMPTOTIC MATCHING

The technique of asymptotic matching is a standard one in the analysis of multiscale and singular perturbation problems, allowing one to relate and combine approximate solutions that are valid on different scales [77]. It has been used in general relativity to obtain, e.g., PN equations of motion—[75] contains the most recent of these calculations—and the radiation zone metric of a binary system [78]. (See Paper I and [75] for further discussion and references.) Here, we specialize our discussion to the case of a black hole binary.

A time slice of a binary black hole spacetime divides naturally into four primary zones and three secondary buffer zones; see Fig. 2 for an illustration. In practical work, the boundaries of all of these zones are necessarily only given approximately, since we do not currently possess sharp estimates for the error bars of the approximations used to describe this spacetime. There are two inner zones around the black holes, given by $r_A \ll b$, where r_A is the distance from (the point particle associated with) hole A, and b is the initial (PN coordinate) separation of the binary: In each of these, the spacetime is well described by a perturbed black hole. Surrounding (and partially overlapping) the inner zones is the near zone, where the standard (harmonic coordinate) PN metric is valid—i.e., not too close to the holes, yet not so far away that retardation cannot be treated perturbatively. This is given by $r_A \gg m_A$ and $r \lesssim \lambda\!\!\!^{-}$, where m_A is the mass of hole A, r is the distance from the system's center of mass, and $\lambda\!\!\!^{-} = b/2v$ is the reduced characteristic wavelength of the binary's gravitational radiation. Finally, the remainder of the time slice (including a small amount of the outer portion of the near zone) comprises the far zone, given by $r \gtrsim \lambda\!\!\!^{-}$, where retardation can no longer be treated perturbatively, and spacetime is described by a separate PN metric that accounts for this. (N.B.: Different relations were given for the outer edge of the near zone and inner edge of the far zone in Papers I and II, but the ones used here are more accurate.) The boundaries of the zones for an equal-mass binary are discussed quantitatively in Sec. VIII B.

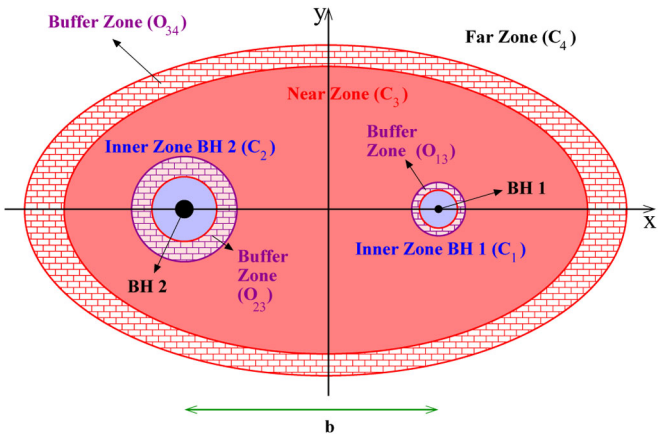

FIG. 2 (color online). A diagram of the zones into which we divide the binary black hole time slice. The two black holes (BH 1 and BH 2, denoted by filled-in circles) lie on the x axis, surrounded by their respective inner zones (C_1 and C_2) and inner-to-near buffer zones (O_{13} and O_{23}). (In actuality, the black holes should be tidally distorted, along with their associated inner and buffer zones. We neglect this distortion in the above diagram for simplicity.) The near zone, C_3, covers the orbit of the binary and is surrounded by the far zone, C_4, and the near-to-far buffer zone, O_{34}.

The three buffer zones are the portions of the time slice where the preceding four regions overlap. (Because of the "fuzziness" inherent in $\lesssim$ and $\gtrsim$, the near and far zone can have a substantial overlap, despite formal appearances.) We restrict our attention to cases in which the specified zones overlap in the manner we shall describe, but in no other fashion (e.g., we do not want the two inner zones to overlap). There are two buffer zones where the two inner zones overlap the near zone, and they are given by $m_A \ll r_A \ll b$. The third buffer zone is given by the intersection of the near and far zones. It is thus very roughly a shell whose radius and thickness are both of order $\lambda\!\!\!^{-}$. (The order of the thickness of the shell is our choice; see Sec. VIII B: All that is required formally is that it increase as v decreases, corresponding to a larger realm of validity of the near zone metric's perturbative treatment of retardation. Additionally, as is indicated in the figure, this buffer zone would not be spherical in a more nuanced description.) These buffer zones are where we perform the formal matching that determines the coordinate transformation and relations between parameters as well as where we stitch the metrics together numerically.

This matching and stitching relies on the observation that if the metrics that are valid in the various zones are all to be different approximations to the same (unknown) global exact metric, then, considered as abstract tensors, they should agree with each other in their realms of mutual validity. More specifically, assume that there exists a buffer zone in which two approximate metrics $\mathbf{g}^{(1)}$ and $\mathbf{g}^{(2)}$ are

both valid. (We write these metrics without indices to emphasize that they are currently being considered as abstract tensors.) Take their associated small parameters to be ϵ_1 and ϵ_2, respectively. (The buffer zone is then defined to be the region in which these parameters are indeed small.) Then make a bivariate expansion of the metrics in both small parameters. That is, take $\mathbf{g}^{(1)}$, which is already an expansion in ϵ_1, and expand it in ϵ_2 as well; similarly, expand $\mathbf{g}^{(2)}$ in ϵ_1. The coefficients of both bivariate expansions, considered as abstract tensors, should then be equal if the metrics describe the same spacetime. The resulting equations relate the parameters of the two metrics.

While the statement of this result in terms of abstract metrics is simple, in practice one works with the metrics' coordinate components. In general, the coordinate systems in which the metrics' components are known will not agree, so one first chooses the coordinate system in which one of the metrics is expressed to be the primary coordinate system. (For us, this will be the near zone's PN harmonic coordinate system.) One then applies an arbitrary coordinate transformation to the other metric in order to put it in the same coordinate system as the first (to the order one matches). Equating coefficients of the bivariate expansions of the components of the metrics (including the coordinate transformation) is then equivalent to equating the coefficients of the expansions of the abstract tensors. In this case, the resulting equations will determine not only the relations between the metrics' parameters, but also the arbitrary coordinate transformation (though there may be some freedom at each order).

III. INNER ZONE METRIC

In Detweiler's perturbed black hole metric [68], the tidal perturbations are encoded by symmetric trace-free electric and magnetic tidal fields $\mathcal{E}_{kl}$ (electric quadrupole), $\mathcal{E}_{klp}$ (electric octupole), $\mathcal{B}_{kl}$ (magnetic quadrupole), and $\mathcal{B}_{klp}$ (magnetic octupole). These come from the THZ harmonic specialization of locally inertial coordinates (from [70,71]), which Detweiler uses to express the perturbation of Minkowski space that his metric approaches in the buffer zone. [N.B.: Detweiler made a tacit gauge transformation away from the pure THZ gauge to obtain the compact expressions for the metric perturbation he gives [79]. This only affects the portion of the perturbation involving the time derivatives of the tidal fields, as can be seen by comparing his Eq. (53) to his Eqs. (56)–(57).]

Detweiler derives his metric under the slow-motion and weak-curvature assumptions of Thorne and Hartle [70]. With these assumptions, the time derivative of a quadrupole field is of octupole order. Since one is only able to include quadrupole and octupole perturbations in linear black hole perturbation theory, the time dependence of the tidal fields in the metric is restricted to the quadrupole fields, and even there it is only linear.

Detweiler [68] presents the metric perturbation in Schwarzschild coordinates, which we denote by $\mathcal{X}^\alpha = (\mathcal{T}, \mathcal{X}^k)$, with a radial coordinate of $\mathcal{P} := \sqrt{\mathcal{X}_k \mathcal{X}^k}$. He gives the portion involving the quadrupole fields, including their time derivatives (which are actually of octupole order), in his Eqs. (G.6)–(G.11), and the portion with the octupole fields in his Eq. (58). The quadrupole tidal fields depend (linearly) on the null ingoing Eddington-Finkelstein coordinate $V := \mathcal{T} + \mathcal{P} + 2M\log(\mathcal{P}/2M - 1)$. (The octupole fields are treated as constants, since their time derivatives are of hexadecapole order.) We have converted his metric to the quasi-Cartesian form of Cook-Scheel harmonic coordinates (from [67]), which we denote by $X^\alpha = (T, X^k)$, with $R := \sqrt{X_k X^k}$. The transformation is given by

$$\mathcal{T} = T - 2M\log\left|\frac{R-M}{R+M}\right|, \qquad \mathcal{X}^k = \left[1 + \frac{M}{R}\right]X^k, \tag{3.1}$$

so $\mathcal{P} = R + M$. Here, M is the mass of the hole. This comes from Cook and Scheel's Eqs. (20), (41), and (43) upon noting that Boyer-Lindquist coordinates reduce to Schwarzschild coordinates for a Schwarzschild hole. (This transformation is for an unperturbed black hole, so the resulting metric will not be in harmonic coordinates, in general, even though the perturbation is in asymptotically harmonic coordinates.) The resulting line element (including the unperturbed Schwarzschild metric) is

$$\begin{aligned} h_{\alpha\beta}dX^\alpha dX^\beta = {} & -H_{T^2}dT^2 + H_{RT}dRdT \\ & + \frac{16}{3}\frac{M^2}{R}\left[1 + \frac{M}{R} - \frac{2}{3}\frac{M^2}{R^2} - \frac{2}{3}\frac{M^3}{R^2(R+M)}\right] \\ & \times \dot{\mathcal{C}}_{klp}X^l X^p dX^k dT \\ & + H_k^{[1]}dX^k\left[\left(1 - \frac{M^2}{R^2}\right)dT - 4\frac{M^2}{R^2}dR\right] \\ & + H_k^{[2]}dX^k dR + H_{R^2}dR^2 + H_{\mathrm{trc}}dX_s dX^s \\ & + O(R^4/\mathcal{R}^4), \end{aligned} \tag{3.2}$$

where

$$H_{T^2} := \frac{R-M}{R+M} + \left[1-\frac{M}{R}\right]^2\left[(\mathcal{E}_{kl}+T\dot{\mathcal{E}}_{kl})X^kX^l + \frac{1}{3}\mathcal{E}_{klp}X^kX^lX^p\right] + \frac{4M^2}{(R+M)^2}\left[R-\frac{5}{3}\frac{M^2}{R}\right]\dot{\mathcal{E}}_{kl}X^kX^l, \tag{3.3a}$$

$$H_{RT} := \frac{8M^2}{(R+M)^2} + 8\frac{M^2}{R^2}\frac{R-M}{R+M}\left[(\mathcal{E}_{kl}+T\dot{\mathcal{E}}_{kl})X^kX^l + \frac{1}{3}\mathcal{E}_{klp}X^kX^lX^p\right] - \left[\frac{4}{3}R + \frac{14}{3}M + \frac{8}{3}\frac{M^2}{R} - 2\frac{M^3}{R^2} - \frac{104}{3}\frac{M^4}{R^2(R+M)} + \frac{80}{3}\frac{M^5}{R^2(R+M)^2} + \frac{32}{3}\frac{M^6}{R^2(R+M)^3}\right]\dot{\mathcal{E}}_{kl}X^kX^l, \tag{3.3b}$$

$$H^{[1]}_k := \frac{2}{3}\left[1+\frac{M}{R}\right]\left[2(\mathcal{C}_{klp}+T\dot{\mathcal{C}}_{klp})X^lX^p + \left(1-\frac{1}{3}\frac{M}{R}\right)\mathcal{C}_{klps}X^lX^pX^s\right], \tag{3.3c}$$

$$H^{[2]}_k := \left[\frac{R}{3} + 2M + \frac{16}{3}\frac{M^2}{R} + \frac{26}{3}\frac{M^3}{R^2} - 11\frac{M^4}{R^3} - \frac{32}{3}\frac{M^5}{R^3(R+M)} - \frac{64}{9}\frac{M^6}{R^3(R+M)^2}\right]\dot{\mathcal{C}}_{klp}X^lX^p, \tag{3.3d}$$

$$H_{R^2} := \sum_{n=1}^{3}\left(\frac{2M}{R+M}\right)^n - \frac{2M}{R} - \frac{M^2}{R^2} + \left[2\frac{M}{R} + 3\frac{M^2}{R^2} - \frac{M^4}{R^4} - \frac{16M^4}{R^2(R+M)^2}\right](\mathcal{E}_{kl}+T\dot{\mathcal{E}}_{kl})X^kX^l + \left[\frac{1}{3}\frac{M}{R} + \frac{1}{3}\frac{M^2}{R^2} - \frac{2}{5}\frac{M^3}{R^3} - \frac{7}{15}\frac{M^4}{R^4} - \frac{1}{15}\frac{M^5}{R^5} - \frac{16}{3}\frac{M^4}{R^2(R+M)^2}\right]\mathcal{E}_{klp}X^kX^lX^p + \left[\frac{16}{3}\frac{M^2}{R} + \frac{80}{3}\frac{M^3}{R^2} + 28\frac{M^4}{R^3} + \frac{40}{3}\frac{M^5}{R^4} - \frac{176}{3}\frac{M^6}{R^4(R+M)} + \frac{72M^7}{R^4(R+M)^2} - \frac{32}{3}\frac{M^8}{R^4(R+M)^3} - \frac{32}{3}\frac{M^9}{R^4(R+M)^4}\right] \times \dot{\mathcal{E}}_{kl}X^kX^l, \tag{3.3e}$$

$$H_{\rm trc} := \left[1+\frac{M}{R}\right]^2\left[1-\left(1+2\frac{M}{R}-\frac{M^2}{R^2}\right)(\mathcal{E}_{kl}+T\dot{\mathcal{E}}_{kl})X^kX^l - \frac{1}{3}\left(1+\frac{M}{R}-\frac{M^2}{R^2}-\frac{1}{5}\frac{M^3}{R^3}\right)\mathcal{E}_{klp}X^kX^lX^p - 4\frac{M^2}{R^2}\left(R+2M-\frac{2}{3}\frac{M^2}{R+M}\right)\dot{\mathcal{E}}_{kl}X^kX^l\right], \tag{3.3f}$$

and $\mathcal{R}$ is a length scale characterizing the strength of the perturbation (see Thorne and Hartle [70] for further discussion). We have defined $\mathcal{C}_{klp} := \epsilon_{kls}\mathcal{B}^s{}_p$ and $\mathcal{C}_{klps} := \epsilon_{klu}\mathcal{B}^u{}_{ps}$, for convenience, as the magnetic tidal fields only appear in the perturbation in these dual forms. Here, ϵ_{klp} is the three-dimensional Levi-Civita symbol, with $\epsilon_{123}=1$.

We include the $\dot{\mathcal{B}}_{kl}$ contributions here, even though they do not increase the formal accuracy of our initial data: We fix the lowest-order piece of $\dot{\mathcal{B}}_{kl}$ when we read off the 1PN correction to the electric octupole (in Appendix B 2) as an application of our matching procedure. Additionally, we have used the fact that $\mathcal{E}_{kl}$ and $\mathcal{C}_{klp}$ only depend linearly on V (to the multipolar order we are considering) to express their T dependence explicitly (where the logarithm in the definition of V cancels one appearing in the Schwarzschild coordinate expression for the metric): An overdot denotes a derivative with respect to T, and all of the symbols for the tidal fields denote constants, so, e.g., $\mathcal{E}_{kl}$ and $\dot{\mathcal{E}}_{kl}$ are treated formally as independent tidal fields, despite the notation. That is, $\mathcal{E}_{kl}$ just denotes the constant part of $\mathcal{E}_{kl}(T) = \mathcal{E}_{kl} + T\dot{\mathcal{E}}_{kl}$. Finally, despite appearances, this expression for the metric is in fact in a quasi-Cartesian form: dR should just be considered a shorthand for $X_k dX^k/R$.

IV. NEAR ZONE METRIC

We take the harmonic coordinate metric from Eqs. (7.2) in BFP [61] and specialize it to a circular orbit, obtaining

$$g_{00}+1 = \frac{2m_1}{r_1} + \frac{m_1}{r_1}[4v_1^2 - (\hat{n}_1\cdot\vec{v}_1)^2] - 2\frac{m_1^2}{r_1^2} - m_1m_2\left[\frac{2}{r_1r_2} + \frac{r_1}{2b^3} - \frac{r_1^2}{2r_2b^3} + \frac{5}{2r_2b}\right] + (1\leftrightarrow 2) + O(v^6), \tag{4.1a}$$

$$g_{0k} = -\frac{4m_1}{r_1}v_1^k - \left\{\frac{m_1^2}{r_1^2}(\hat{n}_1\cdot\vec{v}_1) + \frac{m_1m_2}{S^2}[16(\hat{n}_2\cdot\vec{v}_1) - 12(\hat{n}_2\cdot\vec{v}_2)]\right\}n_1^k - m_1m_2\left\{4\frac{\hat{n}_1\cdot\vec{v}_1}{b^2} - 12\frac{\hat{n}_1\cdot\vec{v}_1}{S^2}\right\}n_{12}^k + \left\{\frac{m_1}{r_1}[2(\hat{n}_1\cdot\vec{v}_1)^2 - 4v_1^2] + \frac{m_1^2}{r_1^2} + \frac{m_1m_2}{b^3}[3r_1 - 2r_2] - m_1m_2\left[\frac{r_2^2}{r_1b^3} + \frac{3}{r_1b} - \frac{8}{r_2b} + \frac{4}{bS}\right]\right\}v_1^k + (1\leftrightarrow 2) + O(v^6), \tag{4.1b}$$

$$g_{kl}-\delta_{kl} = \left\{2\frac{m_1}{r_1} - \frac{m_1}{r_1}(\hat{n}_1\cdot\vec{v}_1)^2 + \frac{m_1^2}{r_1^2} + m_1m_2\left[\frac{2}{r_1r_2} - \frac{r_1}{2b^3} + \frac{r_1^2}{2r_2b^3} - \frac{5}{2r_1b} + \frac{4}{bS}\right]\right\}\delta_{kl} + 4\frac{m_1}{r_1}v_1^kv_1^l + \frac{m_1^2}{r_1^2}n_1^kn_1^l - m_1m_2\left[\frac{4}{S^2} + \frac{4}{bS}\right]n_{12}^kn_{12}^l + 4\frac{m_1m_2}{S^2}[n_1^{(k}n_2^{l)} + 2n_1^{(k}n_{12}^{l)}] + 8\frac{m_1m_2}{b^2}n_{12}^{(k}v_{12}^{l)} + (1\leftrightarrow 2) + O(v^6). \tag{4.1c}$$

(N.B.: We use more of the metric than we give here in the O5 and ALL data sets, discussed in Sec. VII. In fact, the ALL data set includes the full metric that BFP present. We have chosen only to present the portion of the metric that we use in the matching, doing so for reference and to fix notation.) Here, $\vec{x}_A(t)$, $A \in \{1, 2\}$ denotes the position of (the point particle associated with) hole A.[3] Thus $\vec{r}_A := \vec{x} - \vec{x}_A(t)$ gives the displacement from hole A, with $r_A := \|\vec{r}_A\|$ giving the distance from hole A and $\hat{n}_A := \vec{r}_A/r_A$ the associated unit vector. Similarly, $\vec{v}_A := \dot{\vec{x}}_A$ denotes the velocity of hole A. The displacement vector from hole B to hole A is given by $\vec{r}_{AB} := \vec{r}_A - \vec{r}_B$, with an associated unit vector of $\hat{n}_{AB} := \vec{r}_{AB}/\|\vec{r}_{AB}\|$. Thus, specializing to a (quasi)circular orbit, $\|\vec{r}_{12}\| = b$, where b is the separation of the holes and is therefore constant up to orbital shrinkage (which we can neglect when performing the matching, given the order to which we are calculating, though we include it when implementing the metrics numerically; see Sec. VI A). Additionally, we shall usually use the shorthand $\vec{b} := \vec{r}_{12}$. (We do not use it in the above expression for the metric, since $\vec{r}_{12}$ changes sign under $1 \leftrightarrow 2$, while $\vec{b}$ does not.) Similarly, $\vec{v}_{AB} := \vec{v}_A - \vec{v}_B$; we also have $S := r_1 + r_2 + b$. Finally, the notation "$+(1 \leftrightarrow 2)$" denotes that the preceding expression is to be added to itself with the labels 1 and 2 switched.

For a circular orbit, we have $\ddot{\vec{b}} = -\omega^2\vec{b}$, by definition, where

$$\omega = \sqrt{\frac{m}{b^3}}\left[1 + \frac{m}{2b}(\eta - 3) + O\left(\frac{m^2}{b^2}\right)\right] \tag{4.2}$$

is the (harmonic coordinate) angular velocity [obtained from Eq. (8.6) in [61]], and $\eta := m_1 m_2/m^2$ is the symmetric mass ratio. Since we assume a (quasi)circular orbit, the separation vector of the point particles is orthogonal to their velocities up to $O(v^5)$ radiation reaction effects. We have thus taken $\hat{n}_{12} \cdot \hat{v}_1 = \hat{n}_{12} \cdot \hat{v}_2 = \hat{n}_{12} \cdot \hat{v}_{12} = O(v^5)$ in obtaining the expression for the metric given in Eqs. (4.1). We take the explicit expression for the orbit to be $\vec{b} = b(\hat{x}\cos\omega t + \hat{y}\sin\omega t)$. From the definition of the center-of-mass coordinates used in the PN metric, the positions of (the point particles associated with) the holes are given, to the order we need them, by

$$\vec{x}_1 = \frac{m_2}{m}\vec{b}, \qquad \vec{x}_2 = -\frac{m_1}{m}\vec{b}. \tag{4.3}$$

[For a circular orbit, the first PN corrections to these are $O(v^4)$ and are thus not needed here.] The expressions for the holes' velocities are obtained by taking a time derivative.

[3]We shall henceforth refrain from belaboring the distinction between the PN point particles and true black holes, except where we feel that it is important to emphasize this point.

A. The PN metric and conformal flatness

At $O(v^4)$, the spatial PN metric is no longer conformally flat; that is, there does not exist a coordinate system in which the 3-metric can be written as $g_{kl} = \Psi\delta_{kl}$. This can be guessed from a cursory inspection of the PN metric, as nondiagonal spatial components first appear at $O(v^4)$, but was established more firmly in [80], and then further studied in [81]. In both cases, this result was an offshoot of a comparison of the predictions of a post-Newtonian analysis of the Isenberg-Mathews-Wilson approximation [82,83] with those of the full PN approximation: They were found to differ starting at $O(v^4)$. Such a comparison gives the desired result, because the Isenberg-Mathews-Wilson approximation assumes spatial conformal flatness (along with maximal slicing—i.e., a vanishing trace of the extrinsic curvature) in an attempt to remove the dynamical degrees of freedom from the gravitational field.

It is also possible to demonstrate this lack of spatial conformal flatness directly, and we shall do so here. In four or more dimensions, the Weyl tensor settles questions of conformal flatness: It vanishes if and only if a space is conformally flat [84]. However, in three dimensions, the Weyl tensor vanishes identically, and its analogue for settling questions of conformal flatness is the Bach or Cotton-York tensor C_{kl}. This is defined (with indices raised by the 3-metric) by

$$C_{kl} := 2\epsilon_k{}^{ps}\nabla_s R_{lp} - \frac{1}{2}\epsilon_{kl}{}^p\nabla_p R. \tag{4.4}$$

Here, ∇_k, R_{kl}, and R are, respectively, the (three-dimensional) covariant derivative, Ricci tensor, and Ricci scalar associated with g_{kl}. In fact, the nonvanishing of the Cotton-York tensor is a necessary and sufficient condition to render its associated 3-metric nonconformally flat [44,84] (for a proof, see Chap. VI, Sec. 5 in [85]).

We have computed the $O(v^4)$ pieces of this tensor symbolically (using MAPLE and GRTENSORII) for the PN spatial metric in harmonic coordinates and verified that certain components are nonvanishing at various points of the time slice. As an illustration, we have plotted the lowest-order piece of the norm of the Cotton-York tensor $\sqrt{\delta^{kp}\delta^{ls}C_{kl}C_{ps}}$ along the axis passing through the holes in Fig. 3 for the standard equal-mass test system of $m_1 = m_2 = m/2$, $b = 10m$. As expected, the values are largest in the region around the holes, showing that this is the region in which the largest perturbation would be required to make the 2PN metric conformally flat.

There is, however, a more intuitive way of understanding the breaking of spatial conformal flatness of the PN metric (here returning to the ADMTT slicing). This approach relates explicitly to the failure of the PN metric to be manifestly conformally flat at $O(v^4)$ and comes from the

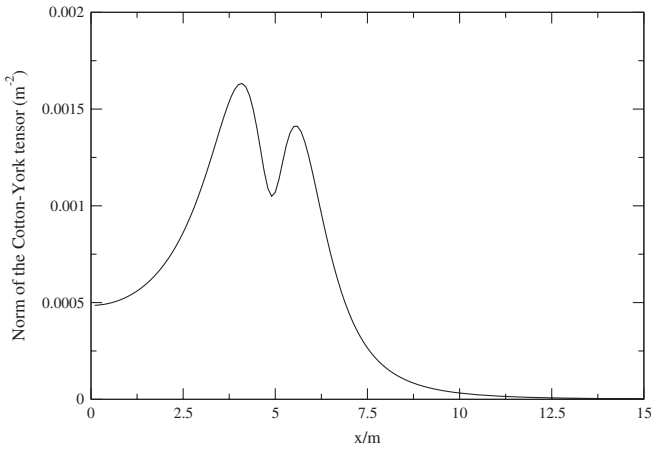

FIG. 3. The norm of the Cotton-York tensor for the test system $m_1 = m_2 = m/2$, $b = 10m$ along the x axis (i.e., the axis passing through both holes). (We only show it around hole 1, because it is symmetric about $x = 0$.)

work of Nissanke [47].[4] From the study of PN theory in the canonical ADM formalism [87], one knows that the PN metric can be rewritten as

$$g_{kl} = \Psi \delta_{kl} + h_{kl}, \tag{4.5}$$

where Ψ is some conformal factor, while h_{kl} is not proportional to the flat metric. In fact, h_{kl} must be symmetric and trace-free and contains a piece that is proportional to

$$\frac{\partial^2}{\partial x_1^{<k} \partial x_2^{l>}} \log S, \tag{4.6}$$

where S was defined in the above discussion of the metric, and the angle brackets stand for the symmetric trace-free projection. [See, e.g., Eq. (3.1) in [47]; we have left off pieces of the form $v_1^{<k} v_1^{l>}$.] This is clearly not a manifestly conformally flat contribution to the metric, so we can use it to connect with the heuristic that "the 2PN metric is not spatially conformally flat, because it contains various pieces that are not manifestly conformally flat."

To do so, we shall demonstrate how the presence in h_{kl} of the term given in Eq. (4.6) prevents the obvious sort of coordinate transformation from rendering g_{kl} conformally flat. For the purposes of illustration, we take our coordinate transformation to be of the form $x^k \to x'^k = x^k + \xi^k$, where $\xi^k = O(v^4)$, and ask that it remove the h_{kl} piece from the 3-metric. (Of course, in general the coordinate transformation would just need to turn h_{kl} into a scalar multiple of δ_{kl} and would not have to be of the form above, but our assumptions suffice for a heuristic argument.) Thus, ξ^k should satisfy

$$\partial_{(k} \xi_{l)} = -\tfrac{1}{2} h_{kl}, \tag{4.7}$$

but this equation has no solution when the right-hand side is given by Eq. (4.6). To show that this is the case, it is sufficient [by the gauge invariance of the linearized Riemann tensor—see the discussion surrounding Eq. (5.5)] to show that the (three-dimensional) flat-space linearized Riemann tensor associated with h_{kl} does not vanish. We have computed this tensor [with h_{kl} given by Eq. (4.6)] and verified that several components are indeed generically nonzero.

[4]This argument was suggested to one of us by Luc Blanchet [86].

B. Gravitational radiation in the PN metric

The order at which the effects of gravitational radiation appear in the PN metric is different for different effects, which can easily lead to confusion. We thus offer a brief discussion of these orders here. To avoid even further confusion, since we shall discuss some pieces that are not dimensionless, we shall describe all orders in terms of the formal slow-motion expansion in $1/c$, as do BFP [61]. [Since the metric is dimensionless, an $O(c^{-n})$ contribution to it can be unambiguously identified as $O(v^n)$.] It is well known that the effects of gravitational radiation reaction first enter the equations of motion at $O(c^{-5})$ for a circular orbit. [See, e.g., Eq. (189) in Blanchet [41].] This is also the leading order of the binary's gravitational wave luminosity. [See, e.g., Eq. (171) in Blanchet [41].] However, the lowest-order "quadrupole formula" piece of the gravitational waveform appears in the PN far zone metric at one order lower, viz., $O(c^{-4})$. This can be seen in Blanchet's Eq. (238) [41]; his x variable (not to be confused with our x coordinate) is $O(c^{-2})$. The explanation for the factor-of-c discrepancy is given by Blanchet in [88].

Our initial data will thus contain at least the lowest-order piece of the binary's outgoing gravitational radiation (whether one uses the extension that adds on various higher-order terms or not), since we have included all the $O(v^4)$ pieces in the spatial metric, along with the matching $O(v^5)$ pieces in the extrinsic curvature. In fact, one can see the lowest-order piece of the waveform explicitly in our expression for the far zone spatial metric in Eq. (6.4c): The relevant terms are the final two in the curly brackets. [These terms are presented in Eqs. (6.10) and (6.11a) of [74] in a form that allows for a more direct comparison with our expression, though without the explicit factors of c^{-1} that Blanchet provides.]

V. THE MATCHING CALCULATION

A. The setup

By symmetry, we can concentrate on performing the matching around hole 1: The transformed metric around hole 2 can be obtained from that around hole 1 by taking $m_1 \leftrightarrow m_2$ and making the coordinate transformation $(t, x, y, z) \to (t, -x, -y, z)$ (i.e., rotating by π radians about the z axis).

Since our matching calculation will determine the coordinate transformation, the relations between the metrics'

mass parameters, and the inner zone metric's tidal fields, we need to posit expansions for all of these. For the coordinate transformation, we make nearly the same ansatz as in Papers I and II, viz.,

$$X^\alpha(x^\beta) = \sum_{j=0}^{5}\left(\frac{m_2}{b}\right)^{j/2}(X^\alpha)_j(x^\beta) + O(v^6). \tag{5.1}$$

(This is slightly more general than the ansatz used in the previous papers, because we do not fix the zeroth-order coordinate transformation from the outset.) We choose $\sqrt{m_2/b}$ as our expansion parameter, because it makes for slightly simpler notation than either $v = \sqrt{m/b}$ or $\sqrt{m_1/b}$ when expanding in the buffer zone around hole 1, as we are doing here. We can make this choice without loss of generality: The resulting coordinate transformation will be the same regardless of which of these three possibilities we choose to use as our expansion parameter, though the coefficients of the expansion parameter will differ by ratios of the masses. As in the previous papers, we implicitly assume that $(X_\alpha)_j$ is a power series in $\tilde{r}/b$, including negative powers—i.e., a Laurent series—so we can write, e.g., $m_2/\tilde{r} = (m_2/b)(b/\tilde{r})$. However, $(X_\alpha)_j$ should not depend on m_2/b, by definition.

We also need to worry about the multipole expansion of each $(X_\alpha)_j$. This would seem to be straightforward, since we only want to keep terms through quadrupole order overall. However, the structure of the inner zone metric creates some complications: In order to obtain data that include all the quadrupole $[O([\tilde{r}/b]^2)]$ pieces at fourth and fifth orders,[5] one needs to obtain the octupole $[O([\tilde{r}/b]^3)]$ pieces of the coordinate transformation when matching at second and third orders. This is due to the appearance of $b/\tilde{r}$ terms in $(h_{\alpha\beta})_j$ for $j \geq 2$. These enter the fourth and fifth order coordinate transformation equations, where they multiply the second and third order pieces of the coordinate transformation and thus produce quadrupole contributions from octupole pieces of the coordinate transformation. The octupole fields themselves also enter, as they are multiplied by $b/\tilde{r}$ in the fourth and fifth order pieces of the inner zone metric.

This increase in the number of multipoles that have to be kept as one proceeds to higher and higher orders in v is a general feature of the matching of these two metrics. It is thus a source of significant technical difficulty: One would need to include the hexadecapole pieces in the matching calculation if one wanted to include all of the quadrupole pieces at sixth and higher orders. This follows, since at sixth order, the hexadecapole pieces start to be multiplied by $b^2/\tilde{r}^2$, making them of quadrupole order. (It would still be possible to, e.g., obtain all the dipole-and-lower pieces at sixth order if one had an expression for the near zone metric through sixth order, but one would not be able to include any new higher-order corrections to the tidal fields this way.)

We posit the same expansion in $\sqrt{m_2/b}$ for the mass parameter of the inner zone metric, M_1, as we did for the coordinate transformation, so

$$M_1 = \sum_{j=0}^{3}\left(\frac{m_2}{b}\right)^{j/2}(M_1)_j + O(v^4). \tag{5.2}$$

However, it will turn out that we did not need to allow this freedom, as we shall find that the mass parameters of the two metrics agree to the highest order to which our matching fixes them—i.e., $M_1 = m_1 + O(v^4)$. Similarly, we asymptotically expand the tidal fields in $\sqrt{m_2/b}$, so

$$\begin{aligned}
\mathcal{E}_{kl} &= \frac{m_2}{b^3}\sum_{j=0}^{3}\left(\frac{m_2}{b}\right)^{j/2}(\bar{\mathcal{E}}_{kl})_j + O(v^6),\\
\dot{\mathcal{E}}_{kl} &= \frac{m_2}{b^3}\sum_{j=1}^{2}\left(\frac{m_2}{b}\right)^{j/2}(\dot{\bar{\mathcal{E}}}_{kl})_j + O(v^5),\\
\mathcal{E}_{klp} &= \frac{m_2}{b^4}\sum_{j=0}^{2}\left(\frac{m_2}{b}\right)^{j/2}(\bar{\mathcal{E}}_{klp})_j + O(v^5),\\
\mathcal{B}_{kl} &= \left(\frac{m_2}{b}\right)^{3/2}\frac{1}{b^2}\sum_{j=0}^{2}\left(\frac{m_2}{b}\right)^{j/2}(\bar{\mathcal{B}}_{kl})_j + O(v^6),\\
\dot{\mathcal{B}}_{kl} &= \left(\frac{m_2}{b}\right)^{2}\frac{1}{b^2}(\dot{\bar{\mathcal{B}}}_{kl})_1 + O(v^5),\\
\mathcal{B}_{klp} &= \left(\frac{m_2}{b}\right)^{3/2}\frac{1}{b^3}\sum_{j=0}^{1}\left(\frac{m_2}{b}\right)^{j/2}(\bar{\mathcal{B}}_{klp})_j + O(v^5).
\end{aligned} \tag{5.3}$$

[The expansions of the duals of the magnetic fields—e.g., $\mathcal{C}_{klp}$—are defined analogously. Additionally, the tidal fields and their time derivatives—e.g., $\mathcal{E}_{kl}$ and $\dot{\mathcal{E}}_{kl}$—are treated as formally independent.] The overbars on the tidal fields appearing in the right-hand sides of these expressions indicate that we have taken out the fields' overall scaling, as given in, e.g., Eqs. (2.1) and (2.2) in [75] (though we take the time derivatives of the tidal fields to scale the same way as the fields themselves when doing this, for clarity). We do not include the $O(v^5)$ pieces of the octupole tidal fields here, because we did not fix them in the matching: We only had to match the octupole fields through $O(v^3)$ to obtain initial data with formal uncontrolled remainders of $O(v^5)$ and $O([\tilde{r}/b]^3)$ (i.e., octupole order). We also chose to read off the $O(v^4)$ pieces of the octupole fields separately (in Appendix B 2), but did not do so for the $O(v^5)$ parts.

In order to read off the matching parameters (and any undetermined pieces of the lower-order coordinate transformations) as efficiently as possible, we note that all of our equations for the coordinate transformation at orders beyond the zeroth will be of the form

[5]We count orders using our primary expansion in v (or, equivalently, $\sqrt{m_2/b}$).

$$\partial_{(\alpha} X_{\beta)} = S_{\alpha\beta} \equiv S_{(\alpha\beta)}. \tag{5.4}$$

Here, $\partial_\alpha := \partial/\partial x^\alpha$ (i.e., all partial derivatives are taken with respect to PN harmonic coordinates), X^α is a function of x^α, and $S_{\alpha\beta}$, the equation's source, is some (symmetric) matrix function of x^α (either explicitly, or implicitly though X^α) which is C^2 in the buffer zone. The integrability condition for this equation is that the flat-space linearized Riemann tensor associated with $S_{\alpha\beta}$ vanish, i.e., that we have

$$\mathcal{I}_{\alpha\beta\gamma\delta} := \partial_{\alpha\beta} S_{\gamma\delta} + \partial_{\gamma\delta} S_{\alpha\beta} - \partial_{\alpha\delta} S_{\gamma\beta} - \partial_{\gamma\beta} S_{\alpha\delta} = 0. \tag{5.5}$$

[N.B.: For convenience, we have defined $\mathcal{I}_{\alpha\beta\gamma\delta}$ with a slightly different index ordering than the linearized Riemann tensor—given for flat space in, e.g., Eq. (5.44) of [89]—and without the factor of $1/2$.] This follows from the gauge invariance of the linearized Riemann tensor. (See, e.g., Sec. 4.1 in Straumann [90] for a proof and discussion of that result. In [91], Blanchet and Damour use this gauge invariance for the same purpose we do.)

For future use, we note that the homogeneous equation, $\partial_{(\alpha} X_{\beta)} = 0$, is the flat-space Killing equation, and its most general solution is given by

$$X_\alpha = F_{\beta\alpha} x^\beta + C_\alpha, \tag{5.6}$$

where $F_{\alpha\beta} \equiv F_{[\alpha\beta]}$ and C_α are arbitrary constant matrices. See, e.g., Sec. 13.1 in Weinberg [92] for a proof. (Our X_α, $F_{\alpha\beta}$, and C_α correspond to Weinberg's ξ_α, $b_{\beta\alpha} = -b_{\alpha\beta}$, and a_α, respectively.) We shall primarily employ this result tacitly at each order beyond the zeroth to ensure that we have the most general expression for that order's contribution to the coordinate transformation.

Our general approach to the nontrivial matching that occurs at second order and beyond will be as follows: We first use the above integrability condition to read off the matching parameters, exploiting the linear independence of various terms to simplify the process and justify our claims of uniqueness. We start with the nonpolynomial terms, which determine many of the previously undetermined parts of the coordinate transformation from two orders lower, as well as the inner zone mass parameter; the polynomial part then determines the tidal fields.[6] [The nonpolynomial part consists of all the terms that are not polynomials in $\tilde{x}^\alpha := x^\alpha - (m_2/m) b \hat{x}^\alpha$. For this calculation, these are all of the form of a polynomial in $\tilde{x}^\alpha$ multiplied by $\tilde{r}^n$, where $n \in \mathbb{Z}\backslash\{0, 2, 4, 6, \cdots\}$.] After we have fixed all the parameters that can be fixed at a given order, we then solve for that order's contribution to the coordinate transformation (and the polynomial part can be solved for separately from the nonpolynomial part that first appears at fourth order). In all of this, MAPLE and GRTENSORII proved very helpful: They work extremely well for all aspects of the polynomial part, while requiring more care when applied to the nonpolynomial part.

[6]It is intuitively reasonable that the polynomial and nonpolynomial parts should determine the parameters that they do: If one neglects all gauge subtleties and the like, then the nonpolynomial terms can be thought of as being those associated with hole 1, and the polynomial terms with (the tidal fields of) hole 2. We discuss this more fully in Sec. V G.

B. Zeroth order $[O([m_2/b]^0)]$

At lowest (zeroth) order in $(m_2/b)^{1/2}$, we find that the coordinate transformation is a (general) Poincaré transformation—i.e., not necessarily one continuously connected to the identity—since the lowest-order piece of either metric is the Minkowski metric. For simplicity, we shall take this lowest-order piece to be the expected translation due to the position of m_1 at $t = 0$, viz.,

$$(X_\alpha)_0 = \tilde{x}_\alpha := x_\alpha - (m_2/m) b \hat{x}_\alpha. \tag{5.7}$$

In fact, one can show that matching through third order requires that the spatial part of the translation be as given above (though the temporal part can still be freely specified). Similarly, that matching requires the Lorentz transformation portion of the Poincaré transformation to differ from the identity only by a possible rotation about the y axis, along with possible spatial and temporal reflections. These are combined with a rotation that takes $+y$ to $-y$ if we have an odd number of reflections. We thus conjecture that matching at higher orders will further constrain this lowest-order coordinate transformation to be as given above. At the very least, the matching at fourth and fifth orders is independent of the remaining freedom.

C. First Order $[O(\sqrt{m_2/b})]$

Since $(g_{\alpha\beta})_1 = (h_{\alpha\beta})_1 = 0$, our equation is just the homogeneous one whose solution is given in Eq. (5.6). We thus have

$$(X_\alpha)_1 = (F_{\beta\alpha})_1 \tilde{x}^\beta + (C_\alpha)_1, \tag{5.8}$$

where we have written this in terms of $\tilde{x}^\alpha := x^\alpha - (m_2/m) b \hat{x}^\alpha$, because $\tilde{r}/b := \sqrt{\tilde{x}_k \tilde{x}^k}/b$ is one of our small parameters. We can do this without loss of generality, as it simply entails a different value for C_α.

This result differs from that given in Eq. (21) of Paper I; the latter suffers from some sign errors introduced during transcription. However, this does not affect that paper's final coordinate transformation, as the relevant constants were all taken to be zero. This is appropriate for Papers I and II, since they were using a corotating coordinate system: The boost encoded in our $(F_{\alpha\beta})_1$ [seen in Eq. (5.20)] would thus not be expected to appear in the coordinate transformation.

D. Second order $[O(m_2/b)]$

Proceeding to the next order, we have, recalling that $(\dot{\bar{\mathcal{E}}}_{kl})_0 = 0$,

$$(h_{\alpha\beta})_2 = \left[\frac{2(M_1)_0}{m_2}\frac{b}{(R)_0} - \frac{(\bar{\mathcal{E}}_{kl})_0}{b^2}(X^k)_0(X^l)_0 - \frac{(\bar{\mathcal{E}}_{klp})_0}{3b^3}(X^k)_0(X^l)_0(X^p)_0\right]\Delta_{\alpha\beta}. \tag{5.9}$$

Similarly, noting that $(\dot{b}_k)_0 = 0$,

$$(g_{\alpha\beta})_2 = \left[\frac{2m_1}{m_2}\frac{b}{(r_1)_0} + 2 - \frac{2}{b}\{(\vec{r}_1)_0\cdot(\hat{b})_0\} + \frac{1}{b^2}\{3[(\vec{r}_1)_0\cdot(\hat{b})_0]^2 - [(r_1)_0]^2\} + \frac{1}{b^3}\{3[(r_1)_0]^2[(\vec{r}_1)_0\cdot(\hat{b})_0] - 5[(\vec{r}_1)_0\cdot(\hat{b})_0]^3\}\right]\Delta_{\alpha\beta}. \tag{5.10}$$

Here, $\Delta_{\alpha\beta} := \mathrm{diag}(1, 1, 1, 1)$ is the lowered four-dimensional Kronecker delta. Also, we have $(\hat{b}_k)_0 = \hat{x}_k$ and $(r_1^k)_0 = \tilde{r}^k$. Thus, at this order, the source of the differential equation [cf. Equation (5.4)] is given by

$$2(S_{\alpha\beta})_2 = 2(A_{(\alpha\beta)})_2 = (g_{\alpha\beta})_2 - (h_{\alpha\beta})_2 - (F_\alpha{}^\gamma)_1(F_{\beta\gamma})_1, \tag{5.11}$$

where $A_{\alpha\beta} := \partial_\alpha X_\beta$.

We now apply the integrability condition from Eq. (5.5) and focus on the nonpolynomial piece of $(S_{\alpha\beta})_2$; here, this is the one that diverges [as $(R)_0 = (r_1)_0 = \tilde{r} \to 0$]. It must satisfy the integrability condition independently of the other pieces, by linear independence, and [considering, e.g., $(\mathcal{I}_{kl00})_2$] gives $(M_1)_0 = m_1$, as expected. The polynomial piece of the integrability conditions tells us that

$$(\bar{\mathcal{E}}_{kl})_0 = \delta_{kl} - 3\hat{x}_k\hat{x}_l, \qquad (\bar{\mathcal{E}}_{klp})_0 = 15\hat{x}_k\hat{x}_l\hat{x}_p - 9\delta_{(kl}\hat{x}_{p)}, \tag{5.12}$$

using linear independence to read off the quadrupole and octupole tidal fields separately. Solving for the coordinate transformation, we obtain

$$(X_\alpha)_2 = \left[1 - \frac{\tilde{x}}{b}\right]\Delta_{\alpha\beta}\tilde{x}^\beta + \frac{\Delta_{\beta\gamma}\tilde{x}^\beta\tilde{x}^\gamma}{2b}\hat{x}_\alpha - \frac{1}{2}(F_\alpha{}^\gamma)_1(F_{\beta\gamma})_1\tilde{x}^\beta + (F_{\beta\alpha})_2\tilde{x}^\beta + (C_\alpha)_2. \tag{5.13}$$

E. Third order $[O([m_2/b]^{3/2})]$

At this order, the inner zone metric is

$$(h_{00})_3 = \frac{2(M_1)_0}{m_2}b\left(\frac{1}{R}\right)_1 + \frac{2(M_1)_1}{m_2}\frac{b}{(R)_0} - 2\frac{(\bar{\mathcal{E}}_{kl})_0}{b^2}(X^k)_0(X^l)_1 - \frac{(\bar{\mathcal{E}}_{kl})_1}{b^2}(X^k)_0(X^l)_0 - \frac{(\dot{\bar{\mathcal{E}}}_{kl})_1}{b^2}(T)_0(X^k)_0(X^l)_0 - \frac{(\bar{\mathcal{E}}_{klp})_0}{b^3}(X^k)_0(X^l)_0(X^p)_1 - \frac{(\bar{\mathcal{E}}_{klp})_1}{3b^3}(X^k)_0(X^l)_0(X^p)_0, \tag{5.14a}$$

$$(h_{0k})_3 = \frac{2}{3}\frac{(\bar{\mathcal{C}}_{klp})_0}{b^2}(X^l)_0(X^p)_0 + \frac{1}{3}\frac{(\bar{\mathcal{C}}_{klps})_0}{b^3}(X^l)_0(X^p)_0(X^s)_0 - \frac{2}{3}\frac{(\dot{\bar{\mathcal{E}}}_{lp})_1}{b^2}(X^l)_0(X^p)_0(X_k)_0, \tag{5.14b}$$

$$(h_{kl})_3 = (h_{00})_3\delta_{kl}, \tag{5.14c}$$

and the near zone metric is

$$(g_{00})_3 = \frac{2m_1}{m_2}b\left(\frac{1}{r_1}\right)_1 - \frac{2}{b}[(\vec{r}_1)_0\cdot(\hat{b})_1] + \frac{2}{b^2}\{3[(\vec{r}_1)_0\cdot(\hat{b})_1]\times[(\vec{r}_1)_0\cdot(\hat{b})_0] - (\vec{r}_1)_1\cdot(\vec{r}_1)_0\} + \frac{6}{b^3}[(\vec{r}_1)_0\cdot(\vec{r}_1)_1]\times[(\vec{r}_1)_0\cdot(\hat{b})_0], \tag{5.15a}$$

$$(g_{0k})_3 = 4\frac{m_1}{m}\left\{1 - \frac{b}{(r_1)_0} - \frac{1}{b}[(\vec{r}_1)_0\cdot(\hat{b})_0] + \frac{1}{2b^2}[3\{(\vec{r}_1)_0\cdot(\hat{b})_0\}^2 - \{(r_1)_0\}^2] + \frac{1}{2b^3}[3\{(r_1)_0\}^2\{(\vec{r}_1)_0\cdot(\hat{b})_0\} - 5\{(\vec{r}_1)_0\cdot(\hat{b})_0\}^3]\right\}\times(\dot{b}_k)_1, \tag{5.15b}$$

$$(g_{kl})_3 = (g_{00})_3\delta_{kl}. \tag{5.15c}$$

Here, we have $(\vec{b})_1 = \sqrt{m/m_2}t\hat{y}$, so $(\vec{r}_1)_1 = -(m_2/m)\times(\vec{b})_1 = -\sqrt{m_2/m}t\hat{y}$, and thus $(\vec{r}_1)_1\cdot(\hat{b})_0 = 0$. Additionally, $(\hat{b})_1 = \sqrt{m/m_2}(t/b)\hat{y}$ and $(\dot{b}_k)_1 = \sqrt{m/m_2}\hat{y}_k$. We also have

$$\left(\frac{1}{R}\right)_1 = -\frac{1}{(R)_0}\frac{(X_k)_0(X^k)_1}{[(R)_0]^2} = -\frac{\tilde{r}^k[(F_{\alpha k})_1\tilde{x}^\alpha + (C_k)_1]}{\tilde{r}^3}, \tag{5.16}$$

and

$$\left(\frac{1}{r_1}\right)_1 = -\frac{1}{(r_1)_0}\frac{(\vec{r}_1)_0\cdot(\vec{r}_1)_1}{[(r_1)_0]^2} = \sqrt{\frac{m_2}{m}}\frac{yt}{\tilde{r}^3}, \tag{5.17}$$

where $\tilde{r}^\alpha := r^\alpha - (m_2/m)b\hat{x}^\alpha$.

At this order, the equations for the coordinate transformation are

$$2(S_{\alpha\beta})_3 = 2(A_{(\alpha\beta)})_3 = (g_{\alpha\beta})_3 - (h_{\alpha\beta})_3 - 2(h_{(\alpha|\gamma})_2(F_{|\beta)}{}^{\gamma})_1 - 2(F_{(\alpha|}{}^{\gamma})_1(A_{|\beta)\gamma})_2, \tag{5.18}$$

recalling that $(h_{\alpha\beta})_1 = 0$ and utilizing our lower-order results. To obtain $(F_{\alpha\beta})_1$, we look at the $\tilde{r}^{-7}$ piece of $(I_{kl00})_3$. Such a piece can only come from two spatial derivatives both acting on $\tilde{r}^{-3}$ in the $\tilde{r}^{-3}$ pieces of $(S_{00})_3$; those pieces, in turn, only come from $(1/R)_1$ and $(1/r_1)_1$. Therefore, using Eqs. (5.16) and (5.17), the integrability conditions require that we have

$$\tilde{r}^{\,k}[(F_{\alpha k})_1\tilde{x}^{\alpha} + (C_k)_1] = -\sqrt{\frac{m_2}{m}}yt, \tag{5.19}$$

from which we immediately see that

$$(C_k)_1 = 0, \qquad (F_{\alpha\beta})_1 = 2\sqrt{\frac{m_2}{m}}\hat{t}_{[\alpha}\hat{y}_{\beta]}, \tag{5.20}$$

using the antisymmetry of $F_{\alpha\beta}$. (Recall that $\hat{t}_0 = -1$.) By similar logic, the $\tilde{r}^{-5}$ piece of $(I_{kl00})_3$ only comes from the $(M_1)_1$ piece of $(h_{00})_3$ and gives us $(M_1)_1 = 0$. The remaining nonpolynomial pieces cancel, so we have extracted all the information we can from the nonpolynomial part of the integrability condition.

From the polynomial part of the integrability conditions, we first read off the octupole parts of the tidal fields, which are

$$(\dot{\bar{\mathcal{E}}}_{kl})_1 = -\frac{6}{b}\sqrt{\frac{m}{m_2}}\hat{x}_{(k}\hat{y}_{l)}, \qquad (\bar{\mathcal{E}}_{klp})_1 = 0, \qquad (\bar{\mathcal{B}}_{klp})_0 = \frac{9}{2}\sqrt{\frac{m}{m_2}}[5\hat{x}_{(k}\hat{x}_l\hat{z}_{p)} - \delta_{(kl}\hat{z}_{p)}], \tag{5.21}$$

and then the quadrupole parts, which are

$$(\bar{\mathcal{E}}_{kl})_1 = 0, \qquad (\bar{\mathcal{B}}_{kl})_0 = -6\sqrt{\frac{m}{m_2}}\hat{x}_{(k}\hat{z}_{l)}. \tag{5.22}$$

The third order coordinate transformation is thus

$$(X_\alpha)_3 = \sqrt{\frac{m}{m_2}}\Bigg\{-\frac{yt}{b^2}\Delta_{\alpha\beta}\tilde{x}^{\beta} + \Bigg[\frac{\tilde{x}_\mu\tilde{x}^\mu - 4\tilde{x}^2}{2b^2} + \left(2 - \frac{m_2}{m}\right)\times\frac{\tilde{x}}{b} + \left(2 + \frac{1}{2}\frac{m_2}{m}\right)\frac{m_2}{m}\Bigg]y\hat{t}_\alpha + 2\left[1 - \frac{m_2}{m}\right]\frac{yt}{b}\hat{x}_\alpha + \left[\frac{3\tilde{r}^2 + t^2}{6b^2} + \left(\frac{m_2}{m} - 2\right)\frac{\tilde{x}}{b} + \frac{1}{2}\left(\frac{m_2}{m}\right)^2 + 4\right]t\hat{y}_\alpha\Bigg\} + \Bigg\{\sqrt{\frac{m_2}{m}}[\hat{y}_{(\alpha}(F_{\beta)0})_2 - \hat{t}_{(\alpha}(F_{\beta)2})_2] + (F_{\beta\alpha})_3\Bigg\}\tilde{x}^{\beta} + (C_\alpha)_3 + \frac{1}{2b^3}\sqrt{\frac{m}{m_2}}\tilde{x}y(4\tilde{x}^2 - y^2 - z^2)\hat{t}_\alpha, \tag{5.23}$$

where the octupole part is the final term.

F. Fourth and fifth orders [$O([m_2/b]^2)$ and $O([m_2/b]^{5/2})$]

The matching at fourth and fifth orders proceeds in the same way as it did at lower orders, though the algebraic complexity increases substantially. We shall thus give far fewer details of the calculations than we did before, and mostly concern ourselves with pointing out the new features of the calculation that arise at these orders. The most prominent new feature, and the one responsible for much of the algebraic complexity, is the presence of a nonpolynomial part in the coordinate transformation. We know to expect this at fourth order, because the transformation between Cook-Scheel and PN harmonic coordinates is nonpolynomial, and its lowest-order piece is $O(v^4)$; see Sec. V G. However, there are various other nonpolynomial pieces present in the coordinate transformation at fourth and fifth orders. We have to solve for these nonpolynomial parts of the coordinate transformation by inspection (though we can still use MAPLE to obtain the polynomial part). It is reasonably easy to do so if one first breaks the source into pieces by multipolar order.

The other subtleties involve the multipole expansion and are best illustrated by giving two examples: $(h_{00})_4$ contains the terms $-2(\bar{\mathcal{E}}_{kl})_0(X^k)_0(X^l)_{2,0}/b^2$ and $(2/3)[(M_1)_0/m_2]\times(\bar{\mathcal{E}}_{klp})_0(X^k)_0(X^l)_0(X^p)_0/b^2(R)_0$. The first of these reflects the necessity of avoiding "hidden octupole" pieces (i.e., pieces of octupole order that arise when multiplying together pieces of lower multipolar order) when looking at corrections to lower-order terms: The dipole piece of $(X^k)_2$ would give an octupole contribution to $(\bar{\mathcal{E}}_{kl})_0(X^k)_0\times(X^l)_2/b^2$, so we only include the monopole piece, denoted by $(X^k)_{2,0}$. Contrariwise, as illustrated by the second term, we do not want to leave out any terms of quadrupole order, even if they arise from, e.g., octupole tidal fields.

These subtleties arise in a slightly different form in the equation for the fifth order piece of the coordinate transformation. Here, we have to avoid hidden octupole terms in many of the contractions: For instance, we only want the quadrupole-and-lower pieces of $(A_{(\alpha|\gamma})_2(A_{|\beta)}{}^{\gamma})_3$, which are given by $(A_{(\alpha|\gamma})_2(A_{|\beta)}{}^{\gamma})_{3,\le 1} + (A_{(\alpha|\gamma})_{2,0}(A_{|\beta)}{}^{\gamma})_{3,2}$. However, it is also necessary to split up the inner zone metric's contributions into polynomial and nonpolynomial parts to keep from excluding quadrupole pieces as well [since the nonpolynomial parts of the second and third order pieces of the inner zone metric are all $O(b/R)$]. In fact, this behavior means that we need to include the octupole part of the third order piece of coordinate transformation [in $(h^{\rm NP}_{(\alpha|\gamma})_2\times(A_{|\beta)}{}^{\gamma})_{3,\le 3}$]. (One would also need to include the octupole part of the second order piece of the coordinate transformation, but it vanishes.)

The rest of the calculation proceeds as before, with the same general results: We obtain the next two orders' contributions to the matching parameters, with the nonpolynomial pieces giving $(F_{\alpha\beta})_2 = 0$ and

$$(F_{\alpha\beta})_3 = \left[\left(\frac{m_2}{m}\right)^{3/2} + 3\sqrt{\frac{m_2}{m}} + 5\sqrt{\frac{m}{m_2}}\right]\hat{t}_{[\alpha}\hat{y}_{\beta]}, \quad (5.24)$$

along with $(C_k)_j = 0$ and $(M_1)_j = 0$ for $j \in \{2, 3\}$. Similarly, the polynomial pieces give

$$(\bar{\mathcal{E}}_{kl})_2 = \frac{1}{2}\left[3\hat{x}_k\hat{x}_l - \delta_{kl} + \frac{m}{m_2}(4\hat{x}_k\hat{x}_l - 5\hat{y}_k\hat{y}_l + \hat{z}_k\hat{z}_l)\right],$$
$$(\bar{\mathcal{B}}_{kl})_2 = \left[5\left(\frac{m}{m_2}\right)^{3/2} + 7\sqrt{\frac{m}{m_2}} - 3\sqrt{\frac{m_2}{m}}\right]\hat{x}_{(k}\hat{z}_{l)}, \quad (5.25)$$

along with $(\bar{\mathcal{B}}_{kl})_1 = (\bar{\mathcal{E}}_{kl})_3 = 0$. The fourth-order piece of the coordinate transformation is

$$(X_\alpha)_4 = -(\mathcal{A}_t)_4\hat{t}_\alpha + \frac{1}{2}\frac{m_1}{m_2}\frac{\tilde{x}}{b}\left[5\frac{\tilde{x}^2}{b\tilde{r}} - 6\frac{\tilde{x}}{\tilde{r}} - \frac{\tilde{r}}{b}\right]\tilde{r}_\alpha + (\mathcal{A}_x)_4\hat{x}_\alpha + (\mathcal{A}_y)_4\hat{y}_\alpha + (\mathcal{A}_z)_4\hat{z}_\alpha + \left\{\sqrt{\frac{m_2}{m}}[\hat{y}_{(\alpha}(F_{\beta)0})_3 - \hat{t}_{(\alpha}(F_{\beta)2})_3] + (F_{\beta\alpha})_4\right\}\tilde{x}^\beta + (C_\alpha)_4, \quad (5.26)$$

where

$$(\mathcal{A}_t)_4 := 4\frac{m_1^2}{m_2^2}\frac{b^2}{\tilde{r}} + t\left[\frac{t^2}{6b^2} + \frac{5(y^2 - \tilde{x}^2) + z^2}{2b^2} + 2\frac{m}{m_2}\frac{\tilde{x}^2 - y^2}{b^2} - \left(\frac{1}{2}\frac{m_2}{m} + \frac{m}{m_2} - 2\right)\frac{\tilde{x}}{b} + 1 + \frac{m}{2m_2} + \frac{3}{2}\frac{m_2}{m} + \frac{5}{8}\left(\frac{m_2}{m}\right)^2\right],$$
$$(\mathcal{A}_x)_4 := \frac{1}{2}\frac{m_1}{m_2}\left[\frac{\tilde{r}^2}{b^2} - 5\frac{\tilde{x}^2}{b^2} + 6\frac{\tilde{x}}{b} + 4\right]\tilde{r} + \left[\left(\frac{t^2 - z^2}{b^2} + \frac{m}{m_2}\frac{z^2 - y^2}{b^2} + 4 - \frac{7}{2}\frac{m}{m_2}\right)\tilde{x} + \left(\frac{m}{2m_2} - 1\right)\frac{\tilde{x}^2}{b} + \left(\frac{m_2}{m} - \frac{m}{2m_2}\right)\frac{y^2}{b} - \left(1 + \frac{3}{2}\frac{m}{m_2} - \frac{m_2}{m}\right)\frac{t^2}{b} + \left(2 - \frac{3}{2}\frac{m}{m_2}\right)\frac{z^2}{b}\right],$$
$$(\mathcal{A}_y)_4 := y\left[\frac{m_1}{m_2}\frac{3\tilde{x}^2 - y^2}{b^2} - \left(\frac{1}{2}\frac{m_2}{m} + 2\frac{m}{m_2} - 2\right)\frac{\tilde{x}}{b} + \frac{5}{2}\frac{m}{m_2} - \frac{9}{2} - \frac{m_2}{2m} - \frac{5}{8}\left(\frac{m_2}{m}\right)^2\right],$$
$$(\mathcal{A}_z)_4 := z\left[\frac{t^2 + z^2 + 3y^2 - 5\tilde{x}^2}{2b^2} + \frac{m}{m_2}\frac{\tilde{x}^2 - y^2}{b^2} + \frac{m}{2m_2} - \frac{1}{2}\right]. \quad (5.27)$$

The fifth order piece is

$$(X_\alpha)_5 = (\mathcal{A}_t)_5\hat{t}_\alpha - \left\{\mathcal{M}_0\left(6, \frac{1}{2}\right)\frac{\tilde{x}yt}{b^2\tilde{r}} + \mathcal{K}\left[3 - \frac{5}{2}\frac{\tilde{x}}{b}\right]\frac{\tilde{x}^2yt}{b\tilde{r}^3}\right\}\tilde{r}_\alpha + \frac{5}{2}\mathcal{K}\frac{\tilde{x}^2t}{b^2\tilde{r}}\epsilon_{0\alpha k3}\tilde{r}^k + (\mathcal{A}_x)_5\hat{x}_\alpha + (\mathcal{A}_y)_5\hat{y}_\alpha + \frac{yzt}{2b^2}\mathcal{M}(3, 3, -5)\hat{z}_\alpha + \left\{\sqrt{\frac{m_2}{m}}[\hat{y}_{(\alpha}(F_{\beta)0})_4 - \hat{t}_{(\alpha}(F_{\beta)2})_4] + (F_{\beta\alpha})_5\right\}\tilde{x}^\beta + (C_\alpha)_5, \quad (5.28)$$

where $\epsilon_{\alpha\beta\gamma\delta}$ is the four-dimensional Levi-Civita symbol, with $\epsilon_{0123} = 1$. We have also defined

$$(\mathcal{A}_t)_5 := \mathcal{M}_0(1, 0)\left[1 + \frac{14}{3}\frac{\tilde{x}}{b}\right]\frac{y}{b}\tilde{r} - 4\mathcal{M}_0(1, 1)\frac{ytb^2}{\tilde{r}^3} - \frac{y}{4}\left[\mathcal{M}(1, 11, -10)\frac{t^2}{b^2} + \mathcal{M}\left(\frac{35}{3}, -\frac{35}{3}, 10\right)\frac{\tilde{x}^2}{b^2} - \mathcal{M}\left(3, -\frac{17}{3}, 6\right)\frac{y^2}{b^2} - \mathcal{M}\left(\frac{5}{3}, \frac{7}{3}, 2\right)\frac{z^2}{b^2} - \mathcal{M}(4, -6, 6)\frac{\tilde{x}}{b} - \mathcal{M}\left(4, \frac{17}{3}, -\frac{17}{3}, 10\right)\frac{m_2}{m}\right],$$
$$(\mathcal{A}_x)_5 := \mathcal{M}_0\left(3, \frac{3}{2}\right)\frac{yt}{b^2}\tilde{r} - \mathcal{K}\left[2 + 3\frac{\tilde{x}}{b}\right]\frac{yt}{\tilde{r}} - \frac{yt}{b}\left[\frac{1}{2}\mathcal{M}(-11, 9, 1)\frac{\tilde{x}}{b} + \mathcal{M}(8, -11, 2, 1)\right],$$
$$(\mathcal{A}_y)_5 := \left[\mathcal{M}_0(2, 0) + \mathcal{M}_0\left(3, -\frac{1}{2}\right)\frac{\tilde{x}}{b}\right]\frac{t}{b}\tilde{r} + 3\mathcal{K}\frac{\tilde{x}^2t}{b\tilde{r}} - \frac{t}{4}\left[\mathcal{M}\left(3, \frac{7}{3}, -\frac{4}{3}\right)\frac{t^2}{b^2} - \mathcal{M}_0(7, 12)\frac{\tilde{x}^2}{b^2} + \mathcal{M}_0(7, 8)\frac{y^2}{b^2} + \mathcal{M}(9, -5, 0)\frac{z^2}{b^2} + \mathcal{M}_0(16, 6)\frac{\tilde{x}}{b} - \mathcal{M}\left(0, \frac{47}{3}, -\frac{17}{3}, 10\right)\frac{m_2}{m}\right] - \mathcal{M}_0(8, 0)\tilde{x}\Big\}, \quad (5.29)$$

and

$$\mathcal{M}(A, B, C, D) := A\left(\frac{m}{m_2}\right)^{3/2} + B\sqrt{\frac{m}{m_2}} + C\sqrt{\frac{m_2}{m}} + D\left(\frac{m_2}{m}\right)^{3/2}, \qquad \mathcal{M}(A, B, C) := A\left(\frac{m}{m_2}\right)^{3/2} + B\sqrt{\frac{m}{m_2}} + C\sqrt{\frac{m_2}{m}},$$
$$\mathcal{M}_0(A, B) := \mathcal{M}(A, -A - B, B) = A\left(\frac{m}{m_2}\right)^{3/2} - (A + B)\sqrt{\frac{m}{m_2}} + B\sqrt{\frac{m_2}{m}}, \qquad \mathcal{K} := \mathcal{M}_0(0, -1) = \sqrt{\frac{m}{m_2}} - \sqrt{\frac{m_2}{m}}, \quad (5.30)$$

where $\mathcal{M}_0(A, B)$ and $\mathcal{K}$ vanish in the limit $m_1 \to 0$ ($\Rightarrow m \to m_2$).

G. Summary of matching results

The final output of the matching is a set of expressions for the tidal fields, which are given explicitly in Eq. (B1), a relation between the mass parameters M and m_1, which we found to be equal [up to uncontrolled remainders of $O(v^4)$], and the coordinate transformation necessary to place the inner zone metric in the same coordinate system as the near zone metric to the order we matched, which we shall discuss further here. To obtain the full coordinate transformation, we start from Eq. (5.1) and insert the various pieces we have read off or chosen. We shall take anything we were unable to fix by matching to be zero; here, this will be C_0 (to all orders), along with $(F_{\alpha\beta})_j$ and $(C_k)_j$ for $j \in \{4, 5\}$. With the results of our matching, this means that we have $C_\alpha = 0$ (to all orders). We took the zeroth-order piece of the coordinate transformation to simply be the expected translation of the origin from the binary's center of mass to hole 1, so

$$(X_\alpha)_0 = \tilde{x}_\alpha := x_\alpha - (m_2/m) b \hat{x}_\alpha. \tag{5.31}$$

With $(C_\alpha)_1 = 0$, we also have

$$(X_\alpha)_1 = (F_{\beta\alpha})_1 \tilde{x}^\beta, \tag{5.32}$$

where

$$(F_{\alpha\beta})_1 = 2\sqrt{\frac{m_2}{m}} \hat{t}_{[\alpha} \hat{y}_{\beta]}. \tag{5.33}$$

Continuing onward, $(X_\alpha)_2$ is given by Eq. (5.13), where $(F_{\alpha\beta})_2 = 0$ and $(C_\alpha)_2 = 0$; $(X_\alpha)_3$ comes from Eq. (5.23), where

$$(F_{\alpha\beta})_3 = \mathcal{M}(0, 5, 3, 1) \hat{t}_{[\alpha} \hat{y}_{\beta]}, \tag{5.34}$$

and $(C_\alpha)_3 = 0$. [$\mathcal{M}(A, B, C, D)$ is defined in Eq. (5.30).] Similarly, $(X_\alpha)_4$ can be obtained from Eq. (5.26), and we take $(F_{\alpha\beta})_4 = 0$ and $(C_\alpha)_4 = 0$. Finally, $(X_\alpha)_5$ is given in Eq. (5.28); again, we set $(F_{\alpha\beta})_5 = 0$ and $(C_\alpha)_5 = 0$.

Looking back over this coordinate transformation, it is possible to gain some physical intuition about what it is accomplishing: The expected Lorentz boost due to the holes' orbital motion is present (through third order, which is the highest order at which we have fixed all the coordinate transformation, up to a possible temporal shift). We also have the lowest-order piece of the transformation between Cook-Scheel and harmonic PN coordinates for an unperturbed Schwarzschild black hole. [This is given by the first term in $(\mathcal{A}_t)_4$ in Eq. (5.27).] The remainder of the coordinate transformation is probably mostly concerned with effecting the transformation from locally inertial coordinates centered on the black hole to PN barycentric coordinates. In addition, as we noted previously, the polynomial and nonpolynomial parts of the full coordinate transformation are related to the individual holes in the expected manner: The nonpolynomial parts are associated with hole 1 and vanish in the limit $m_1 \to 0$. The polynomial pieces are associated with hole 2; indeed, everything except for the piece of the background Cook-Scheel-to-PN-harmonic transformation vanishes in the limit $m_2 \to 0$.

VI. FAR ZONE METRIC

The DIRE approach can be used to compute the full 4-metric $g_{\alpha\beta}$ (in harmonic coordinates) in the far zone. The resulting far zone metric is expressed in terms of derivatives of source multipole moments obtained by integrating the "effective" stress-energy pseudotensor over the near zone. One also obtains nonlinear contributions from integrating over the far zone (known as the outer integral in the DIRE approach), though only two of the resulting terms appear in the metric perturbation $h^{\alpha\beta}$ [defined in Eq. (2.2) of [72]] to the order we are considering.

In this formalism, the metric perturbation in the far zone is given in terms of the source multipoles I^Q and $\mathcal{J}^Q$ (Q is a multi-index)[7] via [Eqs. (5.12) in [72]][8]

$$h^{00} = 4\frac{I}{r} + 2\partial_{kl}\left[\frac{I^{kl}(u)}{r}\right] - \frac{2}{3}\partial_{klm}\left[\frac{I^{klm}(u)}{r}\right] + 7\frac{I^2}{r^2} + O(v^6), \tag{6.1a}$$

$$h^{0k} = -2\partial_l\left[\frac{\dot{I}^{kl}(u)}{r}\right] + 2\epsilon^{lkp}\frac{n^l \mathcal{J}^p}{r^2} + \frac{2}{3}\partial_{lp}\left[\frac{\dot{I}^{klp}(u)}{r}\right] + \frac{4}{3}\epsilon^{lkp}\partial_{ls}\left[\frac{\mathcal{J}^{ps}(u)}{r}\right] + O(v^6), \tag{6.1b}$$

$$h^{kl} = 2\frac{\ddot{I}^{kl}(u)}{r} - \frac{2}{3}\partial_p\left[\frac{\ddot{I}^{klp}(u)}{r}\right] - \frac{8}{3}\epsilon^{ps(k|}\partial_s\left[\frac{\dot{\mathcal{J}}^{p|l)}(u)}{r}\right] + \frac{I^2}{r^2}\hat{n}^k\hat{n}^l + O(v^6). \tag{6.1c}$$

Here, $r := \|\vec{x}\|$ is the distance from the binary's center of mass to the field point, and $\hat{n}^k := x^k/r$ is its associated unit vector. The $(I/r)^2$ terms are the two contributions from the outer integrals mentioned previously. We have included all the terms Pati and Will give, even though some of the ones in the purely temporal and spatial components only contribute terms that are of a higher order than we need here. We do this for completeness and also because we shall need these higher-order terms when we construct the higher-order extension to the data set (the computation of the higher-order far zone metric is sketched in Appendix C).

[7] See, e.g., the discussion following Eq. (2.14) in Pati and Will [72] for the definition of a multi-index.

[8] We have corrected a sign error in Pati and Will's expression for h^{kl}: They give coefficients of $+2/3$ and $+8/3$ for the second and third terms. The correct signs can be obtained from Pati and Will's Eqs. (2.13) and (4.7b) in [72].

The source multipoles $\mathcal{I}^Q$ and $\mathcal{J}^Q$ are defined in Eqs. (4.5) of [72]. With these definitions, the mass monopole $\mathcal{I}$ is simply (a PN corrected version of) the total mass of the system, the dipole moment $\mathcal{I}^k$ is the center-of-mass vector (so it vanishes in our coordinate system), and the current dipole $\mathcal{J}^k$ is the total angular momentum. One can show that these three quantities are conserved up to radiative losses.

The source multipoles can be expanded in the PN approximation to find

$$\mathcal{I} = m_1\left(1 + \frac{1}{2}v_1^2 - \frac{m_2}{2b}\right) + (1 \leftrightarrow 2) + O(bv^4), \tag{6.2a}$$

$$\mathcal{J}^k = \epsilon^{klp} m_1 x_1^l v_1^p + (1 \leftrightarrow 2) + O(b^2v^3), \tag{6.2b}$$

$$\mathcal{I}^{kl} = m_1 x_1^{kl}\left(1 + \frac{1}{2}v_1^2 - \frac{m_2}{2b}\right) + \frac{7}{4}m_1 m_2 b\delta^{kl} + (1 \leftrightarrow 2) + O(b^3v^4), \tag{6.2c}$$

$$\mathcal{J}^{kl} = \epsilon^{kps} m_1 v_1^s x_1^{pl} + (1 \leftrightarrow 2) + O(b^3v^3), \tag{6.2d}$$

$$\mathcal{I}^{klp} = m_1 x_1^{klp} + (1 \leftrightarrow 2) + O(b^4v^2). \tag{6.2e}$$

The first two come from Will and Wiseman's Eqs. (4.16) [74] and the remainder from Pati and Will's Eq. (D1) [73]. (Even though we only need the lowest-order piece of $\mathcal{I}^{kl}$ here, we include the 1PN corrections that Pati and Will give since we need them in our construction of the higher-order extension in Appendix C.) Here, the notation is mostly the same as for the near zone metric and was defined in Sec. IV. The only new definition is $x_1^{kl} := x_1^k x_1^l$ (with similar definitions holding for different vectors, as well as larger collections of indices).

When calculating the metric, we follow the far zone order counting given in Sec. IV C of Pati and Will [72], where each *additional* power of r^{-1} in an expression is treated as $O(v)$. (This is equivalent to the order counting used by Alvi [46].) In obtaining the far zone metric for the $O(v^4)$ data, we modify this prescription slightly to treat factors of r^{-1} that come with factors of G in the far zone's post-Minkowskian expansion as not being "additional," so, e.g., $(\mathcal{I}/r)^2 = O(v^4)$, not $O(v^5)$. The only effect this has is to imply that we keep the outer integral terms in the $O(v^4)$ version of the data instead of dropping them. (We revert back to the pure Pati-Will order counting in the higher-order extensions to the data, as discussed in Appendix C.)

With this order counting, we have $h^{00} = O(v^2)$, $h^{0k} = O(v^4)$, and $h^{kl} = O(v^4)$, so the full 4-metric in the far zone is given by [Eqs. (4.2) in [72]]

$$g_{00} = -\left[1 - \tfrac{1}{2}h^{00} + \tfrac{3}{8}(h^{00})^2\right] + \tfrac{1}{2}h^{kk}, \tag{6.3a}$$

$$g_{0k} = -\left[1 - \tfrac{1}{2}h^{00}\right]h^{0k}, \tag{6.3b}$$

$$g_{kl} = \left[1 + \tfrac{1}{2}h^{00} - \tfrac{1}{8}(h^{00})^2 - \tfrac{1}{2}h^{pp}\right]\delta^{kl} + h^{kl}, \tag{6.3c}$$

with remainders of $O(v^6)$. Here, we have kept the $-(1/2)h^{00}$ term in the expression for g_{0k} for formal consistency (and because we shall need it when we construct the higher-order extension in Appendix C). This term gives a contribution of $O(v^6)$ with our order counting (which we neglect here), but would give terms of $O(v^5)$ if we had used the standard near zone order counting, where $h^{0k} = O(v^3)$. This is the only $O(v^6)$ term in the expression for g_{0k}, so the uncontrolled remainder in that expression is thus actually $O(v^7)$.

We can now easily compute the full metric by taking all the derivatives in the expression for the metric perturbation, Eqs. (6.1). In doing this, it is important to realize that the multipoles depend on retarded time, which must be carefully accounted for when differentiating. Equations (6.3) then give the full metric. In performing this calculation, we assume a (quasi)circular orbit, so we can make the same sorts of simplifications as we did in obtaining the expression for the near zone metric in Sec. IV. After much algebra, we finally obtain the full metric in the far zone:

$$g_{00} + 1 = \frac{2m_1}{r} + \frac{m_1}{r}\left\{v_1^2 - \frac{m_2}{b} + 2(\vec{v}_1\cdot\hat{n})^2 - \frac{2m}{r} + 6\frac{(\vec{x}_1\cdot\hat{n})}{r}(\vec{v}_1\cdot\hat{n}) - \frac{x_1^2}{r^2} + \frac{(\vec{x}_1\cdot\hat{n})^2}{r^2}(3 - 2r^2\omega^2)\right\} + (1 \leftrightarrow 2) + O(v^5), \tag{6.4a}$$

$$g_{0k} = -\frac{m_1}{r}\left\{4(\vec{v}_1\cdot\hat{n}) + 4(\vec{v}_1\cdot\hat{n})^2 - 6(\vec{x}_1\cdot\hat{n})^2\omega^2 + 4\frac{(\vec{x}_1\cdot\hat{n})}{r} + 12\frac{(\vec{x}_1\cdot\hat{n})}{r}(\vec{v}_1\cdot\hat{n}) - 2\frac{x_1^2}{r^2} + 6\frac{(\vec{x}_1\cdot\hat{n})^2}{r^2}\right\}v_1^k + \frac{m_1}{r}\left\{4(\vec{x}_1\cdot\hat{n}) + 8(\vec{x}_1\cdot\hat{n})(\vec{v}_1\cdot\hat{n}) - 2\frac{x_1^2}{r} + 6\frac{(\vec{x}_1\cdot\hat{n})^2}{r}\right\}\omega^2 x_1^k + (1 \leftrightarrow 2) + O(v^6), \tag{6.4b}$$

$$g_{kl} - \delta_{kl} = \frac{2m_1}{r}\delta_{kl} + \frac{m_1}{r}\left\{\left[v_1^2 - \frac{m_2}{b} + 2(\vec{v}_1\cdot\hat{n})^2 + \frac{m}{r} + 6\frac{(\vec{x}_1\cdot\hat{n})}{r}(\vec{v}_1\cdot\hat{n}) - \frac{x_1^2}{r^2} + \frac{(\vec{x}_1\cdot\hat{n})^2}{r^2}(3 - 2\omega^2r^2)\right]\delta_{kl} + \frac{m}{r}\hat{n}^{kl} + 4v_1^{kl} - 4\omega^2 x_1^{kl}\right\} + (1 \leftrightarrow 2) + O(v^5), \tag{6.4c}$$

where everything is evaluated at the retarded time $u := t - r$. [This expression agrees with Alvi's result, given in his Eq. (2.17) [46], though he also includes the $O(v^5)$ terms in the purely temporal and spatial components. We include these

pieces—as well as even higher-order ones—when we construct the extension to the data in Sec. VII and have checked that we agree with Alvi about all the $O(v^5)$ terms.]

A. Evolution of the binary's phase and separation

Even though the effects of radiation reaction on the binary's orbital separation and phase are formally small, only beginning at $O(v^5)$, they produce large corrections to the far zone metric in practice when one is far away from the binary, since the retarded time at which one is evaluating the binary's parameters becomes large. For instance, even as close as $r = 50m$, which is inside the outermost extraction radius (usually well inside) for all the simulations used in the Samurai project [13], the phase difference between a circular orbit [using the 3PN expression for ω given in Eq. (190) of [41]] and 3.5PN inspiral (the computation of which is detailed below) is $\sim$0.015 radians for an equal-mass binary with an instantaneous separation of $10m$. (This phase difference should be compared with the averaged frequency domain phase accuracy required for parameter estimation with Advanced LIGO, viz., 0.007 radians, from [11]. While such a comparison is not really warranted—see [16] for some discussion—it gives a rough idea of the required accuracy.) See Sec. IV A in Kelly *et al.* [48] for further discussion of the necessity of using formally higher-order PN results in obtaining the far zone metric.

We thus use the most accurate (3.5PN) expression for the inspiral, as given by Blanchet [41], who obtains it from an energy balance argument. The phase itself is given by Blanchet's Eq. (234) [41], where it is expressed in terms of the dimensionless time variable Θ, defined in his Eq. (232) [41]. Since we are evaluating everything at the retarded time u, we have $\Theta = (\eta/5m)(t_c - u)$. Here, the "coalescence time" t_c is defined as the time at which the binary's frequency goes to infinity (or, equivalently, its separation goes to zero). One can calculate this in the PN approximation by using the energy balance relation $dE/dt = -\mathcal{L}$, where E and $\mathcal{L}$ are the binary's energy and gravitational wave luminosity, respectively. These are given in terms of $\gamma := m/b$ through 3.5PN in Blanchet's Eqs. (191) and (230) [41], respectively. We can then compute t_c by integrating $dt/db = -(dE/db)/\mathcal{L}$ from $b = 0$ to $b = b_0$ (where b_0 is the binary's separation at $t = 0$). Here, we expand the quotient as a power series (to 3.5PN) rather than using a Padé approximant (or performing any resummation of the energy or luminosity), as is sometimes done in the literature (see, e.g., [93]).

With the 3.5PN expression for t_c in hand, we can simply substitute it (via Θ) into Blanchet's Eq. (234) [41] to obtain the phase as a function of u, making sure to expand to 3.5PN order after substituting. We add a constant to the phase, so it is zero when $t = 0$, to be consistent with our choice of initial phase in the matching (i.e., so the holes initially lie on the x axis, with our expression for the orbit). We also take the freely specifiable gauge constant r'_0 and constant of integration Θ_0 to be m and 1, respectively. The dependence of ω on u is then obtained by differentiating the phase with respect to time.

To obtain the retarded time dependence of b, we use $b = m/\gamma$, along with the expressions for γ in terms of Blanchet's frequency-related parameter $x := (m\omega)^{2/3}$ [Blanchet's Eq. (193) [41]] and x in terms of Θ [Blanchet's Eq. (233) [41]], expanding the quotient consistently to 3.5PN. (Here, Blanchet's x should not be confused with our x coordinate. Also, we take the appearance of b in a logarithm in the expression for γ to consist only of b's lowest-order dependence on Θ, viz., $4m\Theta^{1/4}$.)

We do not display the resulting expressions, as they are quite lengthy, and best handled entirely within a computer algebra system. (We have carried out the calculations in MAPLE and our scripts are available at [39].) Our results can be seen graphically in Fig. 4, where we plot the past history of an equal-mass binary's separation (starting from $b_0 = 10m$) along with the fractional deviations of its phase from $\omega_0 u$. N.B.: The final expansions of the expressions for ϕ and b are important. If they are not performed, then one does not recover the expected values for b and ω at $u = 0$ [viz., b_0 and ω_0, respectively; here, ω_0 is the binary's 3PN angular velocity for $b = b_0$ obtained from Blanchet's Eq. (190) [41]].

Using these high-order phasing relations means that we are effectively using high-order equations of motion. We would have thus liked to include higher-order terms in the relative-to-center-of-mass (relative-to-COM) variable relation as well, for consistency, rather than merely the lowest-order Newtonian relation [given in Eq. (4.3)], which is all that is needed formally in the far zone, even in our extended data. However, the resulting expressions for the far zone metric components are algebraically too complex for

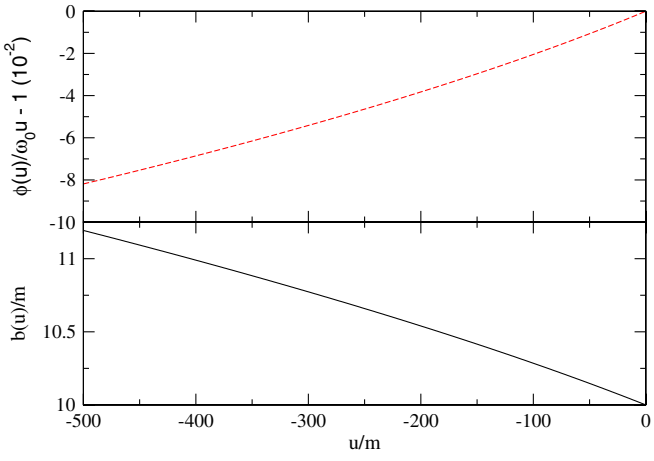

FIG. 4 (color online). The 3.5PN results for the past history of an equal-mass binary's separation, starting from $10m$ at $u = 0$, along with the fractional deviations of its phase from $\omega_0 u$.

MAPLE to handle, so we had to forego including any additional terms. Fortunately, unlike the secular radiation reaction effects in the binary's phase and separation considered above, the neglected PN corrections to the relative-to-COM relation are numerically small in addition to being formally small: They first enter the metric at $O(v^8)$ (in the purely temporal component) and produce corrections of $\sim 5 \times 10^{-7}$ to terms whose uncorrected value is $\sim 10^{-4}$.

We *were* able to include these additional terms in the relative-to-center-of-mass relation in the near zone metric: For consistency, we include the same higher-order terms in the phasing and separation in the near zone metric as in the far zone metric, so it makes sense to attempt to include the higher-order relative-to-COM relation there, even though we were unable to do so in the far zone metric. In fact, these corrections contribute to the near zone metric at one order lower than to the far zone metric [viz., $O(v^7)$ in the spatiotemporal components] and are numerically quite a bit larger: They give corrections of $\sim 2 \times 10^{-3}$ to terms whose uncorrected value is ~ 0.2.

Blanchet and Iyer give these corrections through 3PN in Eqs. (3.11)–(3.14) of [94]. We have specialized their result to a circular orbit by using the 2PN expression for ω to express v in terms of m, b, and η. Blanchet gives this relation specialized to a circular orbit through 2.5PN in Eq. (187) of [41], so we shall just quote the 3PN contribution to $\vec{x}_A$ (which has no A dependence):

$$\vec{x}_A^{\,\mathrm{3PN}} = -\eta \frac{(m_1 - m_2)m^2}{b^3}\left[\frac{7211}{1260} + \eta - \frac{22}{3}\log\left(\frac{b}{r_0''}\right)\right]\vec{b}. \tag{6.5}$$

In this expression, r_0'' is another freely specifiable gauge constant which, though *a priori* different from r_0', we shall take to have the same value, viz., m. [This is equivalent to taking the related gauge constants r_1' and r_2' to both be m; see Eqs. (3.15) and (3.19) in [94].] The expression for the binary's separation vector that we substitute into the resulting relative-to-center-of-mass relation to obtain the trajectories of the point particles is $\vec{b} = b(\hat{x}\cos\phi + \hat{y}\sin\phi)$, where b and ϕ are functions of t (in the near zone) or u (in the far zone).

VII. INCLUDING HIGHER-ORDER TERMS

Here, we construct an extension to our data using various readily available higher-order terms. This extension includes all the $O(v^5)$ terms in the near and far zones, but also includes even higher-order terms that do not improve the data's formal accuracy. The general philosophy is that adding higher-order terms can often improve the quality of the data in practice, even if it does not improve their formal accuracy. As we have seen in the previous section, this is particularly true in the far zone, where the binary's phase evolution depends sensitively on the inclusion of quite high-order radiation reaction terms.

There are also more specific reasons for including certain of these terms: We would like for a putative evolution of our data to be able to be compared directly with Kelly *et al.*'s evolution of their data [60]. (Such a comparison will give an indication of how much of the junk radiation is due to the failure of the initial data to include the correct tidal deformations.) Kelly *et al.* include the $O(v^5)$ pieces of the spatial metric in the near zone [though not the matching $O(v^6)$ pieces of the extrinsic curvature]. The extension we have constructed includes these terms, as well. It also includes (as noted above) the $O(v^5)$ terms in the far zone, along with the $O(v^6)$ terms in the extrinsic curvature in the near and far zones, so the extended data are valid through $O(v^5)$ in those zones. However, we have coded our data in such a way that one can easily produce a data set that only includes the pieces that Kelly *et al.* have, or some other subset of the pieces in the extension.

We would have liked to include the $O(v^5)$ terms in the inner zone as well, for completeness, but it is not possible to obtain initial data in that zone that are formally $O(v^5)$ while still including the quadrupole pieces with the inner zone metric we have: We would need the $O(v^6)$ pieces of (the spatiotemporal components of) the inner zone metric. The quadrupole parts of these include hexadecapole tidal fields, and knowledge of how those fields enter the inner zone metric requires nonlinear black hole perturbation theory (this has since been carried out by Poisson and Vlasov [66]). However, we *are* able to calculate the polynomial parts of the fourth and fifth order octupole pieces, and we actually carried out the calculation for the fourth-order pieces. We present the results in Appendix B 2 and include these additional contributions in the extension. (These pieces include the 1PN correction to the electric octupole tidal field.)

Moreover, we are also able to include the full time dependence of the tidal fields (up to radiation reaction effects); see Appendix B 1. It seems desirable to include these terms, since some of them are necessary for obtaining the pieces of the extrinsic curvature that describe how the tidal fields evolve. We already have the necessary, linear-in-t pieces for the lowest-order quadrupole fields, but not for their 1PN corrections, the explicit appearance of their time derivatives, or any of the octupole fields. We discuss the specifics of how we include this time dependence and what exactly we are neglecting in its inclusion in Appendix D. We have *not* attempted to obtain the full time dependence of the coordinate transformation, since this is a rather more involved task than obtaining that of the tidal fields. Moreover, our rationale for including the tidal fields' full time dependence was to improve the evolution of the tidal perturbations: Including the full time dependence of the coordinate transformation would only improve the agreement of the inner and near zone metrics in the buffer zone, while the largest effect of the tidal perturbations (e.g., in reducing the high-frequency junk radiation) presumably comes from closer to the horizons.

The other higher-order pieces we have added are all in the purely temporal components of the near and far zone metrics. We have included these since Blanchet, Faye, and Ponsot [61] give an explicit expression for the purely temporal component of the near zone metric through $O(v^7)$, and it is easy enough to calculate the matching terms in the far zone. The specifics of where we obtained all the extra terms are given in Appendix C, along with the accompanying caveats and new order counting in the far zone. We refer to these ''state-of-the-art'' versions of the near and far zone metrics as the full extended versions.

We have considered the effects of these additional terms on how well the metrics stitch together by putting together four versions of the data, shown in Table II. While the versions in the table are given the labels we use for the corresponding MAPLE scripts and *C* code (available at [39]), we shall usually refer to them by the order of their near and far zone metrics [i.e., as $O(v^4)$, $O(v^5)$, and full extended]. This will not cause confusion, since we will almost always consider just the right-most three. While the O4_NOOCT version is important, since it contains only the pieces that can be included consistently in the matching (except for the higher-order terms necessary to obtain the phasing in the far zone accurately and the analogous terms in the near zone), we only consider it in one portion of the next section. Thus, when we refer to the $O(v^4)$ version without any qualifiers, we mean O4, the version including the fourth-order octupole pieces. See Appendix D for the specific details of how all of these metrics are calculated. (N.B.: The near zone metrics in all of these versions contain the background resummation detailed in Sec. VIII A.)

As we shall see in the next section, including the additional terms reduces the resulting data's constraint violations, or at least does not affect them adversely. The only exception to this is the addition of the full time dependence in the inner zone, which increases the constraint violations in the inner zone. However, it does not increase them by much, and they were originally quite small. Our philosophy is thus to include these terms, which we think will improve the data's evolution, even at the cost of slightly higher constraint violations. (Kelly *et al.* [60] have also seen that including more physics—from the transverse-traceless piece of the metric—increases the constraint violations.)

VIII. NUMERICAL CONSIDERATIONS

To gain some feel for how well the matching is working numerically, along with the differences between the various versions of the initial data, we plot the volume elements of the various 4-metrics in the vicinity of their buffer zones. The volume element is, of course, coordinate dependent, but is nevertheless a very convenient quantity to use, particularly when comparing the matching of different versions of the data. We display the differences between the volume elements of various versions of the constituent metrics in the inner-to-near transition in Fig. 5, and the volume elements themselves in the near-to-far transition in Fig. 6, along with the volume element of the merged metric. Of course, we first transform the inner zone metric using the coordinate transformation obtained from the algebraic matching above.

To obtain a simple, easily interpreted plot, we choose the test system $b = 10m$, $m_1 = m_2$ (the mass is in arbitrary units) and restrict our attention to the $t = 0$ time slice and the x axis (i.e., we consider the spatial slice along the separation between the holes), concentrating on the portion near hole 1. We expect this slice to provide the most stringent test of the matching, since it contains the portions of the buffer zones where the field is strongest and changes most rapidly. Additionally, an initial separation of $10m$ is large enough that it is reasonable to expect that the ingredients making up the construction are valid. But it is also small enough to test the ingredients near the edge of their region of validity, and to be comparable to the initial separations used in most current numerical relativity simulations. We shall thus use this setup (or slight modifications thereof) for all of our later examples. In all of these plots, we use the full extended version of the data discussed in the previous section, unless otherwise noted.

The inner zone metric we display here contains the fourth-order octupole pieces discussed in Appendix B 2. To avoid clutter, we did not plot the ''plain'' version without these additional pieces: It agrees very closely with the version we have plotted near and inside the horizon, but bends away from the near zone metric further away from the hole. The differences between the versions of the inner zone with full and perturbative time dependence would not appear in this plot, since we are looking at the $t = 0$ time slice. We display the differences between the $O(v^4)$, $O(v^5)$, and full extended far zone metrics in

TABLE II. An overview of the contents of the various data sets we considered.

Zone	Attribute	Versions			
		O4_NOOCT	O4	O5	ALL
Inner	Time dependence	Perturbative	Perturbative	Full	Full
Inner	Fourth-order octupoles	No	Yes	Yes	Yes
Near, Far	Metric order	$O(v^4)$	$O(v^4)$	$O(v^5)$	Full extended

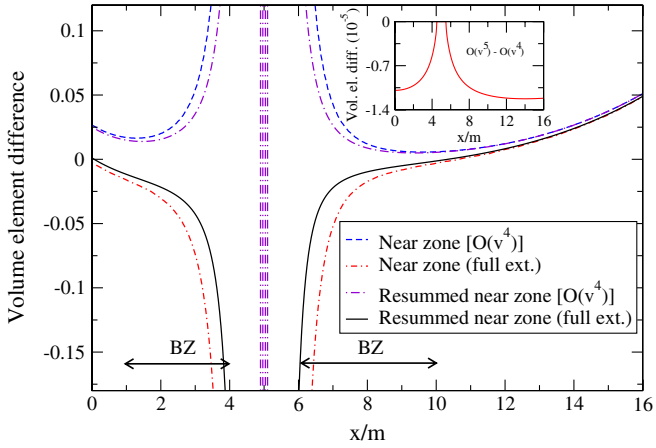

FIG. 5 (color online). The differences between the volume elements of various near zone metrics and the volume element of the full extended inner zone metric. We have indicated the rough locations of the intersection of the x axis with hole 1's inner-to-near buffer zone (BZ) using double-headed arrows. We have also displayed the differences between the volume elements of the $O(v^4)$ and $O(v^5)$ resummed metrics in the inset.

Fig. 7, considering a binary with mass ratio 3:1 so these differences are more pronounced. (In this plot, we have concentrated on the portion of the x axis to the right of the more massive hole, for clarity: The relations between the various metrics are qualitatively the same to the left of the less massive hole, except for differences in relative amplitude.)

In the near zone metric, the extension adds certain terms that become large when evaluated close to the holes (e.g.,

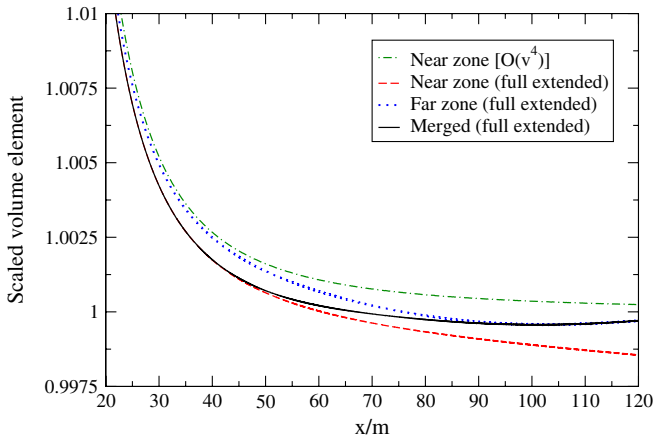

FIG. 6 (color online). The scaled volume elements of the (resummed) near zone [both $O(v^4)$ and extended], far zone, and merged metrics. These are calculated for our equal-mass test system and plotted along the x axis in the portion of the near-to-far transition region that lies to the right of hole 1. To obtain a less crowded plot, we have scaled these by the contribution to the volume element of the lowest-order nontrivial pieces of the far zone metric, viz., $(1 + 2m/r)\sqrt{1 - 4m^2/r^2}$. The buffer zone is roughly the region in which we transition, which, in turn, is roughly the region plotted.

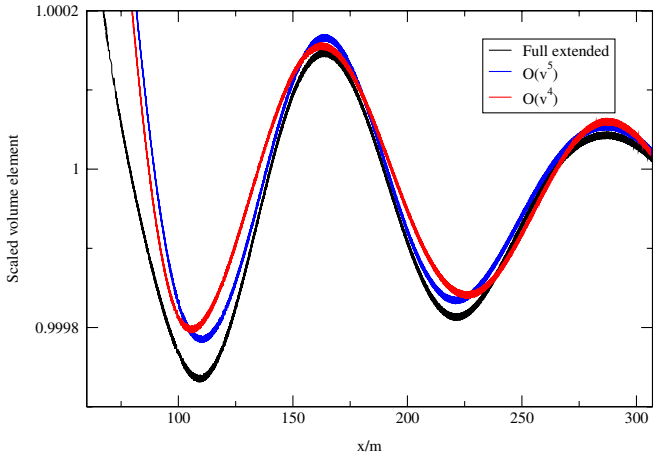

FIG. 7 (color online). The scaled volume element of the far zone metric for a binary with a separation of $10m$ and a mass ratio of 3:1 along the x axis to the right of hole 1 (the more massive hole). We display this for the extended data (the darkest curve in greyscale) as well as the $O(v^5)$ and $O(v^4)$ versions of the data (the medium and lightest curves in greyscale, respectively) to illustrate their differences. (We considered an unequal-mass binary to make these differences more pronounced.) As before, we have scaled these volume elements by the contribution from the lowest-order nontrivial piece of the metric, viz., $(1 + 2m/r)\sqrt{1 - 4m^2/r^2}$.

$4m_1^2m_2/r_1^3$ in g_{00}, which equals $1/2$ at $r_1 = m$ for our test system) and others that grow rapidly as one moves away from the holes (e.g., $-m_1^2m_2r_1^3/4b^6$, also in g_{00}, which is about -0.03 at $r_1 = 100m$ for our test system). The terms that become large near the holes cause the $t = 0$ time slice of the near zone metric to no longer be spacelike in a region that extends outside the horizon. However, for this separation, the time slice is still spacelike in the buffer zone, so its bad behavior closer to the holes does not cause any problems in the merged metric.

N.B.: The unperturbed horizon is $m_1[1 - m_2/b + O(m_2^2/b^2)]$ away from the point particle associated with hole 1 in the new coordinates. For the test system, the correction is small, so hole 1's unperturbed horizon intersects the x axis at $\sim 4.5m$ and $\sim 5.5m$ in the new coordinates. There are also corrections due to the tidal distortion, but for the test system these are even smaller than those due to the new coordinates; see Sec. VIII in Taylor and Poisson [75] for a study of the effects of the lowest-order quadrupole tidal distortion on the horizon.

The Newman-Penrose scalar ψ_4 gives a coordinate-independent (though still tetrad-dependent) measure of the success of the matching. (It also gives a measure of the data's gravitational wave content in the far zone.) Compared to the volume element, ψ_4 is also more sensitive to the specifics of the transition functions, since it contains first and second derivatives of the metric. We plot ψ_4 for the merged and constituent full extended metrics in the inner-to-near and near-to-far transitions in Figs. 8 and 9,

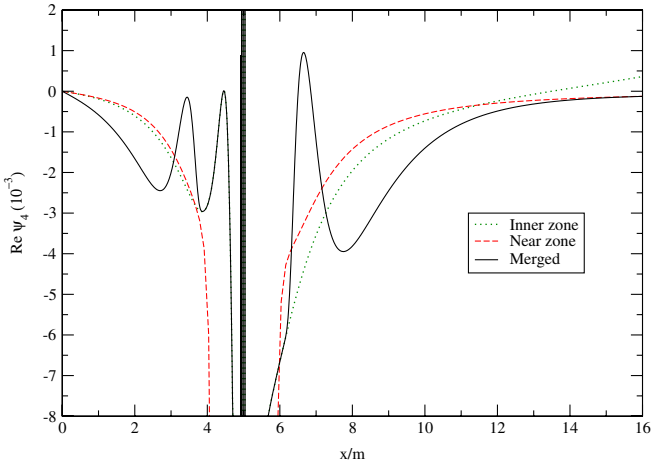

FIG. 8 (color online). The real part of the Newman-Penrose scalar ψ_4 of the inner, near, and merged metrics computed for our equal-mass test system and displayed in the vicinity of the inner-to-near transition.

respectively. (We computed ψ_4 using BAM [95,96]; its built-in tetrad is discussed in Sec. III A of [95]. Additionally, we only plot the real part of ψ_4, because the imaginary part is several orders of magnitude smaller.)

In the inner-to-near transition, the volume elements and ψ_4 generally behave in the expected manner: They differ when considered either too near or too far from the hole and approach each other in the buffer zone. Things look a bit more unusual in the near-to-far transition, since the two volume elements agree better in the region between $20m$ to $30m$ than they do further away from the holes, and ψ_4 actually agrees (somewhat) better even further in. However, this should not be surprising: The reduced wavelength of the gravitational radiation is $\sim 16m$ for the equal-mass test system, and the difference between the near zone metric's perturbative treatment of retardation and the far zone metric's full treatment should become quite apparent beyond that radial distance. In fact, the oscillations we see in the far zone metric's volume element and ψ_4 (in Figs. 7 and 9, respectively) are due to the far zone metric's dependence on retarded time. (Even though the metric contains gravitational radiation, this is not the only source of the oscillations of the volume element. However, it does contribute to them, as expected. The oscillations in ψ_4 can likely be identified with gravitational radiation, though we are probably not quite far enough from the binary to do so completely unambiguously.) The former plot also illustrates the phase differences between the various versions of data.

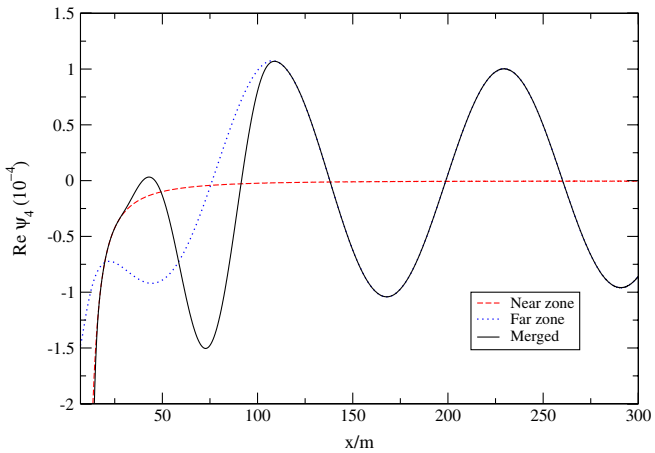

FIG. 9 (color online). The real part of the Newman-Penrose scalar ψ_4 of the near, far, and merged metrics computed for our equal-mass test system and displayed in the vicinity of the near-to-far transition, as well as the far zone proper, and even some of the inner-to-near transition (included to show how the near and far zone metrics compare close to the binary).

A. Background resummation

In the inner-to-near transition (as shown in Fig. 5), the volume elements of the original (unresummed) metrics do not agree as closely as we might like. In fact, the agreement is *worse* near the hole with the higher-order extended version of the near zone metric than it is with the original $O(v^4)$ version (though the agreement further away from the hole and outside the orbit is slightly better). However, even the agreement with the original version is not much better than that found in Paper II (see its Fig. 2), even though we have matched to higher order.[9] Part of the resolution of this apparent problem is that we have not yet used one of the "tricks" from Paper II, namely, background resummation.

The idea of background resummation is to add higher-order terms to the near zone metric in order to improve its strong-field behavior. If one considers the limit $m_2 \to 0$ ($\Rightarrow v_1 \to 0$) of the near zone metric, then one finds that it reduces to the far field asymptotic expansion of the unboosted Schwarzschild metric (with mass parameter m_1) in PN harmonic coordinates. This expansion, however, lacks the causal structure of the Schwarzschild metric—it has no horizon.

One method to restore this causal structure is to resum the PN metric. This resummation consists of adding an infinite number of higher-order terms, such that the metric reduces identically to the full unboosted Schwarzschild metric in PN harmonic coordinates in the limit $m_2 \to 0$. *A priori*, there is no reason to suspect that adding such higher-order terms would increase the accuracy of the PN metric. *A posteriori*, however, it is usually the case that such resummed metrics are indeed closer to the exact

[9]The figures are not directly comparable, since the one in Paper II plots the xx components of the metrics, not their volume elements. However, the plot of just the xx components of this paper's inner and near zone metrics displays the same behavior as that of the volume elements, including roughly the same numerical values for the difference between the metrics.

solution, as was seen in Paper II. Moreover, we should stress that these higher-order terms are not arbitrary, but guided by the physical requirement of restoring the apparent horizons. Such physically informed resummations have met with great success in general relativity, notably in the effective one-body formalism (see, e.g., [97]).

It would also be possible to resum the far zone metric: One can calculate its Newtonian part without making a multipole decomposition by proceeding in the same manner as in the calculation of the Liénard-Wiechert 4-potential in electrodynamics (as given in, e.g., Sec. 14.1 in Jackson [98]). However, we have not pursued this line of investigation further. Simone *et al.* [40] performed a related resummation of the Newtonian pieces of the luminosity of an extreme mass-ratio binary, though they did this by first calculating the multipole expansion and then resumming directly, while the resummation of the metric we are suggesting here would involve computing the integral directly, with no multipole expansion of the Newtonian part.

With these points in mind, let us now describe the near zone resummation in detail, exemplifying it using the purely temporal component of the metric. In PN harmonic coordinates, this component of the Schwarzschild metric takes the form $-(R-M)/(R+M)$. Here, R is the harmonic radial coordinate, and M is the hole's mass. (As our use of "R" indicates, this is the same radial coordinate as in Cook-Scheel harmonic coordinates; see Appendix A for a comparison of the two coordinate systems.) We expect to have $m_1 \to M$ and $r_1 \to R$ as $m_2 \to 0$, which suggests that the purely temporal component of the PN metric should approach $-(r_1 - m_1)/(r_1 + m_1)$ as $m_2 \to 0$. The far field asymptotic expansion of this metric component (i.e., for $r_1 \gg m_1$) is given by

$$-1 + \frac{2m_1}{r_1} - \frac{2m_1^2}{r_1^2} + O\left(\left[\frac{m_1}{r_1}\right]^3\right). \tag{8.1}$$

This identically reproduces all of the terms in the PN near zone metric in the limit $m_2 \to 0$. We then resum the PN near zone g_{00} by taking

$$g_{00} - g_{00}^{\text{old}} = -\frac{r_1 - m_1}{r_1 + m_1} - \left(-1 + \frac{2m_1}{r_1} - \frac{2m_1^2}{r_1^2}\right) + (1 \leftrightarrow 2), \tag{8.2}$$

where g_{00}^{old} is the version of this component without resummation, given in Eq. (4.1a).

A similar procedure can be applied to the spatial sector of the metric. Carrying this out, we obtain

$$\begin{aligned} g_{kl} - g_{kl}^{\text{old}} = {} & \frac{r_1 + m_1}{r_1 - m_1} n_{kl}^{(1)} + \left(1 + \frac{m_1}{r_1}\right)^2 [\delta_{kl} - n_{kl}^{(1)}] \\ & - \left[\left(1 + \frac{2m_1}{r_1} + \frac{m_1^2}{r_1^2}\right)\delta_{kl} + \frac{m_1^2}{r_1^2} n_{kl}^{(1)}\right] \\ & + (1 \leftrightarrow 2), \end{aligned} \tag{8.3}$$

where $n_{kl}^{(1)} := x_1^k x_1^l / r_1^2$ and g_{kl}^{old} is given by Eq. (4.1c). One can check that g_{kl} reduces to g_{kl}^{old} identically as $m_2 \to 0$.

We have used the Schwarzschild metric in PN harmonic coordinates to resum the PN metric here, since it is this background that the PN metric approaches in the $m_2 \to 0$ limit. We thus cannot resum the spatiotemporal components of the metric, since they already match the background in this limit. If we had first transformed the PN metric to Cook-Scheel coordinates, then we would have been able to resum the background so it exactly matched that of the inner zone metric. This would have guaranteed a better agreement and would have probably also given a merged metric with smaller constraint violations, since there would be no coordinate singularity at the horizons in the resummed near zone metric.

However, if we had chosen this route, we would have had to pick some region surrounding the buffer zone for each hole in which to perform this transformation. This would have introduced further complications that we thought it best to avoid in this implementation, even at the possible cost of somewhat poorer matching. Moreover, the background resummation procedure that we have implemented has indeed improved the matching, as can be seen in Fig. 5: The improvement is particularly striking for the extended version of the near zone metric, where the region in which the $t = 0$ slice is no longer spacelike moves closer to the horizon and the graph of its volume element now crosses that of the near zone in the buffer zone outside of the orbit. But resummation also improves the matching of the original data: The resummed version of the $O(v^4)$ near zone metric agrees more closely with the inner zone metric than does the unresummed version.

B. Transition functions

We now turn to the process of stitching the inner and near zone metrics together numerically. It is necessary to interpolate between the various metrics in *transition regions* (located inside the buffer zones) in order to stitch the metrics together with no discontinuities. A simple way to do this is to use a weighted average of the metrics, where the precise way this average is carried out is determined by a C^∞ *transition function* F_{AB}: $\mathbb{R}^3 \to [0, 1]$. This function should have the property that $F_{AB}(\vec{x}) = 0$ if $\vec{x} \in C_A \cap O_{AB}^{\mathsf{c}}$ and $F_{AB}(\vec{x}) = 1$ if $\vec{x} \in C_B \cap O_{AB}^{\mathsf{c}}$. Here, O_{AB}^{c} is the complement of the buffer zone between zones C_A and C_B. (These conditions guarantee that the transition takes place completely inside the buffer region.) If we just consider two metrics, $g_{\alpha\beta}^{(A)}$ and $g_{\alpha\beta}^{(B)}$, for simplicity, then the resulting merged metric is given by $[1 - F_{AB}]g_{\alpha\beta}^{(A)} + F_{AB} g_{\alpha\beta}^{(B)}$. (We have suppressed the position dependence of the transition functions and metrics, for notational convenience.)

In principle, these conditions are all one would impose on possible transition functions. (One might also want to stipulate that F_{AB} be "increasing as one moves from C_A to

C_B,'' where this would have to be interpreted in some appropriate sense.) One could then contemplate minimizing some appropriate norm of the constraint violations of the resulting merged metric (outside, say, the apparent horizons) over all possible transition functions satisfying these requirements [99]. Our approach will be significantly less ambitious, leaving a systematic study of transition functions to later work, probably the work that accompanies an evolution of the data.

However, as Yunes [38] realized, one can exclude from consideration *a priori* any transition functions that would induce larger (formal) constraint violations in the data than those due to the uncontrolled remainders of the individual metrics. The so-called Frankenstein theorems enunciated in [38] provide conditions on the transition functions that are sufficient to exclude all such functions that lead to this undesirable behavior. These conditions are that the first and second derivatives of F_{AB} be $O(\epsilon_A, \epsilon_B)$ and $O(\epsilon_A^0, \epsilon_B^0)$, respectively. (Here, ϵ_A represents the small parameters associated with zone A.) As discussed in Sec. I A, the theorems imply that initial data obtained using transition functions satisfying these conditions will satisfy the constraint equations to the same formal order as the constituent pieces of the initial data do. We shall explicitly verify that our transition functions respect these conditions.

We have made simple choices for the geometry of the transition regions, using spherical symmetry whenever possible, even though neither the binary nor the holes are spherically symmetric. We have implicitly acknowledged the latter in the inner-to-near transitions by introducing another transition function (called f_{near} and discussed below) that only depends on x, the Cartesian coordinate along the axis passing through the holes at $t = 0$. While we do not have to worry about our transition functions' lack of time dependence (which one would expect to be present, because the transition regions change position as the binary evolves), since we perform all our stitching-together on the initial hypersurface, this time dependence would affect the results if one chose to obtain initial data from the merged 4-metric.

Moreover, we shall only consider one particular form for the transition functions, viz., the same form used in Papers I and II:

$$f(r, r_0, w, q, s) := \begin{cases} 0, & r \le r_0, \\ \frac{1}{2}(1 + \tanh\{(s/\pi)[\chi(r, r_0, w) - q^2/\chi(r, r_0, w)]\}), & r_0 < r < r_0 + w, \\ 1, & r \ge r_0 + w, \end{cases} \tag{8.4}$$

where $\chi(r, r_0, w) := \tan[\pi(r - r_0)/2w]$. The effects the parameters have on f is discussed after Eq. (16) in Vega *et al.* [100] (Vega *et al.*'s x_0 corresponds to our r_0). Additionally, despite its piecewise definition, f is in fact C^∞ if $s > 0$: One can check directly that f itself is continuous; all of its derivatives are continuous, since all the derivatives of tanh vanish at infinity. The full merged metric is thus

$$\begin{aligned} g_{\alpha\beta} = {} & [1 - f_{\text{far}}(r)](f_{\text{near}}(x)\{f_{\text{inner},1}(r_1) g^{(3)}_{\alpha\beta} \\ & + [1 - f_{\text{inner},1}(r_1)] g^{(1)}_{\alpha\beta}\} + [1 - f_{\text{near}}(x)]\{f_{\text{inner},2}(r_2) g^{(3)}_{\alpha\beta} \\ & + [1 - f_{\text{inner},2}(r_2)] g^{(2)}_{\alpha\beta}\}) + f_{\text{far}}(r) g^{(4)}_{\alpha\beta}, \end{aligned} \tag{8.5}$$

where $g^{(A)}_{\alpha\beta}$ denotes the metric that lives in zone A (see Fig. 2 for the numbering system, and recall that we obtain $g^{(2)}_{\alpha\beta}$ from $g^{(1)}_{\alpha\beta}$ using the transformation given at the beginning of Sec. V A), and

$$\begin{aligned} f_{\text{far}}(r) &:= f(r, \lambda/5, \lambda, 1, 2.5), \\ f_{\text{near}}(x) &:= f(x, 2.2m_2 - m_1 b/m, b - 2.2m, 1, 2.5), \\ f_{\text{inner},A}(r_A) &:= f(r_A, 0.256 r_A^T, 3.17(m^2 b^5)^{1/7}, 0.2, b/m). \end{aligned} \tag{8.6}$$

Here, x denotes the near zone (PN harmonic) x coordinate, $\lambda = \pi\sqrt{b^3/m}$ is the Newtonian wavelength of the binary's gravitational radiation, and $r_A^T = (m_A^3 b^5/m)^{1/7}$ is the ''transition radius,'' obtained by requiring that the leading orders of the uncontrolled remainders be comparable in the inner and near zones $[(m/b)(r_A^T/b)^4 = (m_A/r_A^T)^3]$. For convenience, we shall refer to the value of a parameter appearing in a particular transition function by transferring that transition function's subscript to the parameter's name, e.g., $w_{\text{inner},A} := 3.17(m^2 b^5)^{1/7}$.

With these choices for the parameters, the transition functions satisfy the hypotheses of the first Frankenstein theorem, given above. For instance, the nth spatial derivatives of f_{near} and f_{far} scale as $w_{\text{near}}^{-n} \propto b^{-n} \propto v^{2n}$ and $w_{\text{far}}^{-n} = 1/\lambda^n \propto v^n$, respectively. Matters are a bit more complicated for $f_{\text{inner},A}$: It satisfies the hypotheses, since its spatial derivatives decrease rapidly when $v \to 0$. This occurs, because these derivatives involve sech with an argument that goes to infinity as $v \to 0$ [since $s_{\text{inner},A} \propto v^{-2}$] and sech is rapidly decreasing at infinity.

We determined the parameters we use for the transition functions by experimenting with different choices. We found that the values given in Eq. (8.6) produced the smallest overall constraint violations along the x axis for our equal-mass test system (with $b = 10m$) of all the choices we tried. Except for the near-to-far zone transition, which is completely new, these choices are very similar to those in Paper II. (In fact, despite the way it is written, our f_{near} agrees exactly with its analogue from Paper II, the function

G.) The most important difference is the scaling of the transition width, $w_{\text{inner},A}$. Both Papers I and II took $w_{\text{inner},A}$ to scale with r_A^T, so it depends on the system's mass ratio; in particular, it goes to zero as $m_A \to 0$. (Note that our $f_{\text{inner},A}$ corresponds to F_A in Papers I and II.) We have found that this choice for $w_{\text{inner},A}$ results in large transition-induced constraint violations near the smaller black hole for unequal mass ratios. These constraint violations appear to increase without bound as the mass of the smaller hole goes to zero. This is as one would expect, since the gradient of the transition function blows up as the transition width goes to zero, leading to an unbounded increase in constraint violations; see [38] and the above discussion of the Frankenstein theorems.

We can obtain a better-behaved transition function by freezing the dependence of $w_{\text{inner},A}$ on the mass ratio, as we have done here. (We also have a slightly different coefficient of r_A^T than in Paper II, even for an equal-mass system.) The other differences between our $f_{\text{inner},A}$ and Paper II's F_A are a slightly different coefficient of the transition radius in $r_{0,\text{inner},A}$, in addition to a new transition radius that reflects the higher-order matching that we have performed here. (The transition radius, r_A^T, was slightly misleadingly called the matching radius and referred to as r_A^M in Paper II.)

The choices for the transition functions' parameters determine effective boundaries for the various zones. These are given in Table III for our equal-mass test binary. This table displays both the formal boundaries (i.e., the numerical values of the boundaries given in Sec. II) as well as the effective boundaries (i.e., the boundaries determined by our choices of parameters for the transition functions). What we call the complete effective boundaries are determined by the entire region in which we use a given metric, even if the coefficient of the metric (due to the transition functions) is very small in a portion of the region. What we refer to as the practical effective boundaries are cut off when the coefficient of the metric becomes smaller in magnitude than 10^{-4} [i.e., much smaller than the magnitude of the uncontrolled remainders, which are $\sim(b/m)^{-5/2} \simeq 3 \times 10^{-3}$].

The effective inner zone boundaries given in Table III are not quite correct: Since even the practical effective boundaries of the inner zones are greater than half the distance between the holes for $b = 10m$ (as they are for an equal-mass binary, with our choice of transition functions, for $b \lesssim 165m$), one needs to introduce a third transition function, here called f_{near}, to effect the transition between the holes. (See Sec. VI B of Paper I for further discussion; this function is referred to as G in Papers I and II.) With our choice of parameters, f_{near} cuts off the complete effective inner zone when the x coordinate is closer than $1.1m$ to (the x coordinate of the point particle associated with) the other hole. The practical effective inner zone is cut off when the x coordinate is $1.93m$ away from the other hole.

In f_{far}, one might be concerned that even the practical effective transition region extends well outside of the standard outer boundary of the near zone, viz., $r \simeq \lambda\!\!\!^{-}$. Indeed, it is quite possible that blending in the near zone metric in a region where its perturbative treatment of retardation is not warranted will introduce significant phase errors in the binary's outgoing wave train. However, our choice of transition region is justified (at least for this preliminary construction of transition functions) by the (relatively) large constraint violations of the far zone metric at the inner edge of our transition region, as is shown in Fig. 10.

The matching is illustrated in our plots of ψ_4 for the merged and constituent metrics, given in Figs. 8 and 9. (Recall that we use the full extended version of the data in all plots unless otherwise noted.) It is clear that the transition functions have introduced undesirable features into the initial data. Some of this is probably unavoidable at a separation of $b = 10m$, which is relatively close for this construction. However, it seems likely that one could choose transition functions that would stitch the metrics together with (at least somewhat) smaller additional features, though we have not investigated this here.

TABLE III. The zone boundaries for our equal-mass test binary ($b = 10m$).

Zone	Formal boundaries	Effective boundaries	
		Complete	Practical
Inner	$r_A \ll 10m$	$r_A \leq 17.4m$	$r_A \leq 11.2m$
Near	$r_A \gg 0.5m$, $r \lesssim 15.8m$	$r_A \geq 0.985m$, $r \leq 119m$	$r_A \geq 1.27m$, $r \leq 109m$
Far	$r \gtrsim 15.8m$	$r \geq 19.9m$	$r \geq 30.4m$

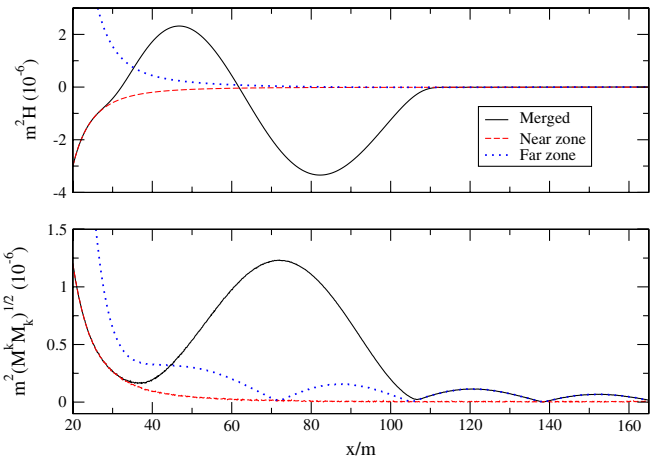

FIG. 10 (color online). The constraint violations of the merged, near zone, and far zone metrics. These are plotted along the x axis in a region including the portion of the near-to-far transition region to the right of hole 1. As usual, this is done for our standard equal-mass test binary.

C. Constraint violations

The constraint violations provide a more sensitive check on how well the transition functions are working than the previous subsection's plots, in addition to giving a measure of the accuracy of the entire initial data construction. We compare the constraint violations (computed using BAM [95,96]) of the individual metrics to those of the merged metric for our equal-mass test system along the x axis in Figs. 10 and 11. (We have checked that the constraint violations behave roughly similarly—and are not significantly worse—in the y and z directions.) For the norm of the momentum constraint, M_k, we have chosen $\sqrt{M^k M_k}$, where the index is raised using the (merged) metric. [See, e.g., Eqs. (14)–(15) in [24] for expressions for the constraint equations; we denote the Hamiltonian constraint by H.] N.B.: While the plots we display do not cover the entire inner-to-near transition, the constraint violations' behavior in the portion we do not show is analogous to the portion we do show.

All of the constraint violations decrease at least as rapidly as $b^{-5/2}$, the expected scaling of the largest uncontrolled remainders. (The expected scaling of the uncontrolled remainders in the near and far zones is b^{-3}, due to the additional terms added in Sec. VII, and the constraint violations decrease more rapidly than this in those regions.) This is illustrated in Figs. 12 and 13 in the inner and near zones, and in Fig. 14 in the far zone. In fact, one can see that the decrease of the maximum constraint violations in a given region is *much* more rapid than $b^{-5/2}$ (or b^{-3}, in the near and far zones), proceeding at b^{-n}, with $n \gtrsim 5$, for everything except the Hamiltonian constraint in the inner-to-near transition. For the latter, it is only slightly more rapid (n slightly larger than $5/2$). This is, in fact, the region (outside of the horizons) where the merged metric has the largest constraint violations. These are likely due in part to the near zone metric's large constraint violations near the horizons, which themselves are primarily attributable to the coordinate singularity at the horizons. (Recall that the horizons are approximately $.5m$ away from the positions of the point particles in our test system—the effects of the new coordinates and tidal distortion are small.) However, it is not clear why the momentum constraint violations in the inner-to-near transition decrease so much faster with b than do the Hamiltonian constraint violations.

The much faster decrease of the constraint violations with increasing b than naïve scaling arguments would predict is not unexpected, at least for the far zone metric,

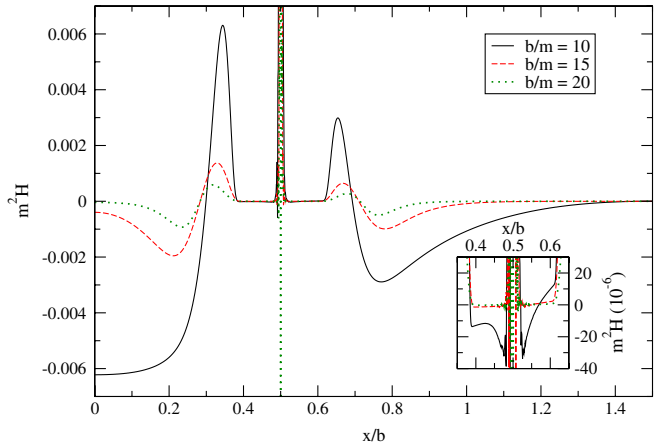

FIG. 12 (color online). The Hamiltonian constraint around hole 1 for an equal-mass binary with separations of $10m$, $15m$, and $20m$. For ease of comparison, we have scaled the x axis by b so that (the point particle associated with) hole 1 is always at the same position. In the inset, we zoom in to show how the inner zone constraint violations vary with b.

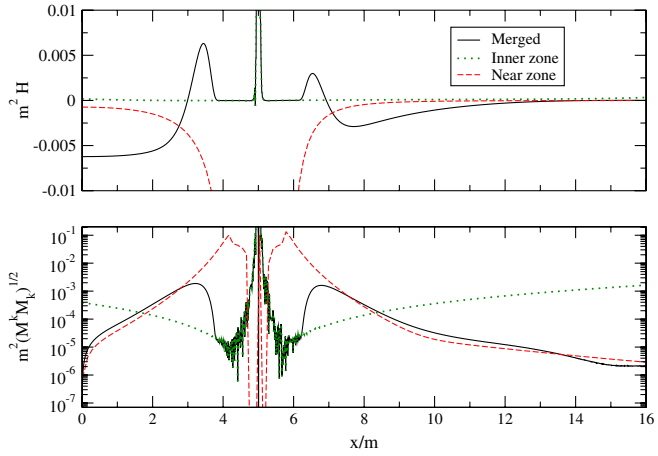

FIG. 11 (color online). The constraint violations of the merged, inner zone, and near zone metrics. These are plotted along the x axis around hole 1 for our standard equal-mass test system.

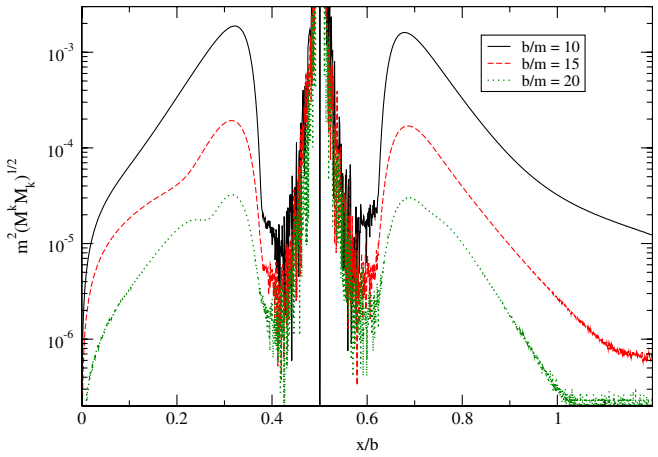

FIG. 13 (color online). The norm of the momentum constraint around hole 1 for an equal-mass binary with separations of $10m$, $15m$, and $20m$. For ease of comparison, we have scaled the x axis by b so that (the point particle associated with) hole 1 is always at the same position.

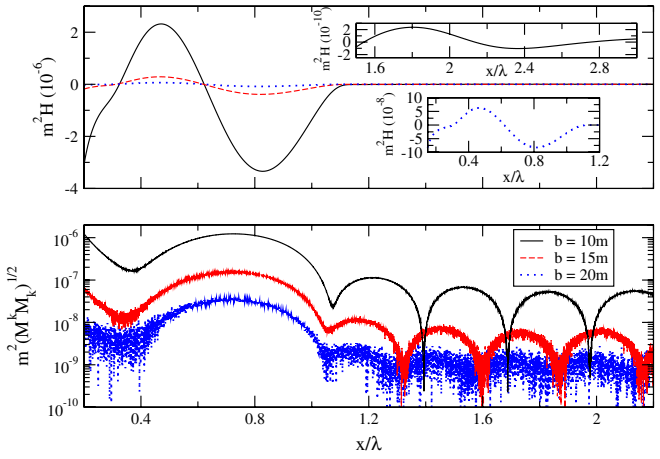

FIG. 14 (color online). The constraint violations along the x axis in the portion of the near-to-far transition and far zone proper that lies to the right of hole 1. These are computed for an equal-mass binary with separations of $10m$, $15m$, and $20m$. For ease of comparison, we have scaled the x axis by $\lambda = \pi\sqrt{b^3/m}$, the Newtonian wavelength of the binary's gravitational radiation. In the two insets, we zoom in to better illustrate the behavior of the Hamiltonian constraint in two situations: In the lower inset, we consider the $b = 20m$ data in the transition region. In the upper inset, we consider the $b = 10m$ data in the far zone proper. (The other data sets also display similar oscillations in their Hamiltonian constraint in the far zone, though the amplitude of these oscillations is too small to be visible on the scale we use to display the oscillations of the $b = 10m$ data's Hamiltonian constraint.)

though the reasonably simple arguments we have tried cannot quite reproduce the scaling we observe, just predicting a decrease that is faster than the naïve prediction. In the far zone metric, all the uncontrolled remainders come with a factor of m/r, and since the inner boundary of the far zone scales as $b^{3/2}$ [see the discussion in Sec. II and around Eq. (8.6)], this leads to a leading-order scaling of $b^{-9/2}$ in the constraint violations, coming from two spatial derivatives acting (via retarded time dependence) on the v^4 part of uncontrolled remainders of the form $(m/r)v^4$. The observed scaling is b^{-n}, with $n \gtrsim 6.5$. It is possible that at least some of this faster decrease than the naïve prediction is due to the addition of all of the higher-order terms (discussed in Sec. VII).

For a separation of $10m$, the relatively large constraint violations of the merged initial data compared to those of the individual metrics' initial data are an indication that this separation is close to the minimum for which the hypotheses underlying the data's construction are valid. For instance, as seen above, for this separation (and an equal-mass binary), the two inner-to-near transition regions overlap between the holes, meaning that much of the inner-to-near transition is effected by f_{near}; see Table III and the surrounding discussion. Moreover, as we have seen previously, the $t = 0$ slice of the near zone metric is not even spacelike at some points outside the holes' horizons for $b = 10m$. However, this does not adversely affect the merged metric with our choices of transition regions. If one tries closer separations, things are significantly worse. For instance, for a separation of $6m$, the maximum constraint violations are larger than those for $10m$ by a factor of 10 or more. Furthermore, the points at which the near zone metric's $t = 0$ time slice is no longer spacelike can cause problems for such small separations with our transition functions if one obtains the initial data by merging the individual metrics' initial data sets, as we have done. (However, if one obtains data directly from the merged 4-metric, then the $t = 0$ slice remains spacelike with our transition functions for initial separations at least as small as $5m$ [101].)

We compared the constraint violations of the new data with the old data (for our standard test system) in Fig. 1 and Table I in Sec. I A, though we deferred a more detailed discussion until now. First, it is important to realize that the comparison could be somewhat misleading, since each paper's data are in a different coordinate system. (The data from Paper I are in the same harmonic coordinate system as this paper's data in the near zone. However, this is only true perturbatively in the inner zone, where the black hole background is in a coordinate system that is not horizon penetrating.)

Second, while our data's Hamiltonian constraint violations are not appreciably better than those of the data from Paper II, even though we have matched to higher order, this is not unexpected: Even though we used horizon-penetrating coordinates for the black hole metrics, we used standard PN harmonic coordinates for the PN metric; these coordinates are singular at the horizon. While the merged metric has no coordinate singularities, the PN metric's coordinate singularity increases the constraint violations in the transition regions, making them comparable to those from Paper II: Paper II's data use a PN metric with no coordinate singularity as well as even further resummation of the black hole backgrounds than we have employed here, leading to particularly small constraint violations.

Finally, if one compares Fig. 1 with, e.g., Figs. 14 and 17 in Paper II, then one notices differences in the behavior of the data from Papers I and II close to the hole (and inside the horizon). This is because we have generated the plot using higher-order finite differencing (fourth order vs second order) and a higher resolution ($0.002m$ vs $0.008m$) in computing the constraint violations here than we did in first computing them in Paper II. It was necessary to do this to accurately resolve the constraint violations in the inner zone, since the metric components diverge rapidly there. Additionally, we have used the version of Paper II's metric that is in horizon-penetrating coordinates, while Figs. 14 and 17 in Paper II were generated using the version of the data without that additional coordinate transformation: The transformation to horizon-penetrating coordinates introduces further structure in the data's constraint violations.

We can also compare the constraint violations of the full extended data with those of the $O(v^4)$ and $O(v^5)$ versions. We do this in the inner-to-near transition in Fig. 15 for a binary with a mass ratio of 3:1, and in the near-to-far transition (along with the far zone proper) for that binary, as well as an equal-mass binary, in Fig. 16. [We consider a unequal-mass binary to make the differences between the $O(v^4)$ and $O(v^5)$ versions more pronounced: Most of the $O(v^5)$ terms in the far zone metric vanish for an equal-mass binary.]

In the latter plot (Fig. 16), we do not show the differences between the $O(v^4)$ and full extended versions' Hamiltonian constraint in the far zone proper, as they agree up to the level of numerical truncation error. We also do not show the differences between the $O(v^5)$ and full extended versions of the data. These two sets only differ substantially in the far left-hand portion of the transition region, and even there the differences are several orders of magnitude less than those between the $O(v^4)$ and full extended versions. Additionally, we do not show the behavior of the constraint violations to the left of the smaller hole (hole 2): It is qualitatively similar to their behavior to the right of the larger hole shown here, except that for an equal-mass binary, the $O(v^4)$ version of the data has smaller Hamiltonian constraint violations than the full extended version in that region, and for a mass ratio of 3:1, there is no oscillation in the transition region in the $O(v^4)$ data's momentum constraint violations.

We compare the constraint violations of the different inner zone versions in Fig. 17 for binaries with mass ratios of 1:1 and 3:1. In this plot, we do not include the version of the inner zone with no fourth-order octupole pieces, as the inclusion of those terms does not affect the constraint violations in the inner zone proper at a level above numerical truncation error. However, these terms *do* have a noticable effect on the constraint violations in the inner-to-near transition, as can be seen in Fig. 18, which compares the $O(v^4)$ data with and without the fourth-order octupole terms in the inner zone. (The fact that including the fourth-order octupole terms in the inner zone metric makes a much larger difference in the merged metric than in the inner zone metric itself in the transition regions suggests that the additional terms that have the most significant

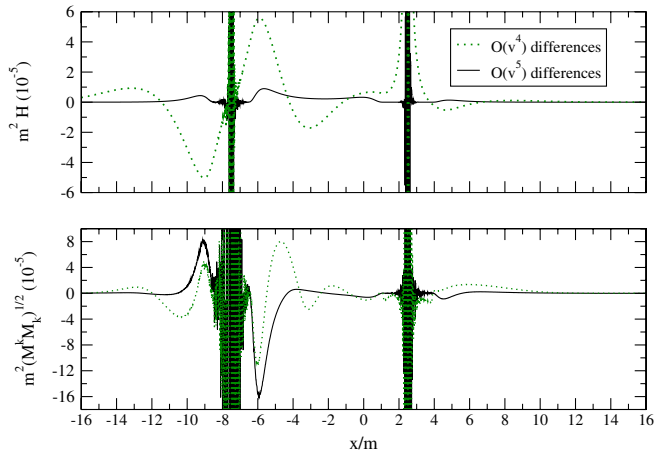

FIG. 15 (color online). The constraint violations of the $O(v^4)$ and $O(v^5)$ sets of data minus those of the full extended set of data. These are computed along the x axis in the inner-to-near transition region for a binary with $b = 10m$ and a mass ratio of 3:1. (The more massive hole is on the right.)

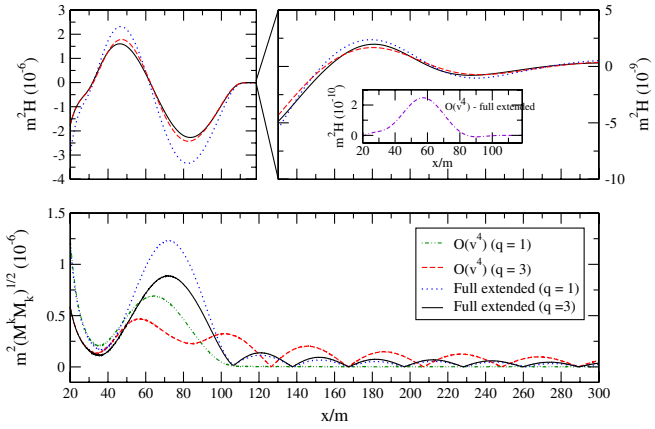

FIG. 16 (color online). The constraint violations of the $O(v^4)$ and full extended sets of data. These are computed along the x axis in the near-to-far transition region (and far zone proper) to the right of hole 1 for binaries with $b = 10m$ and mass ratios of 1:1 and 3:1 (here, $q := m_1/m_2$). (The more massive hole is on the right.) In the right-hand panel, we zoom in to show the differences in the oscillation of the Hamiltonian constraint in the far zone proper. In the inset, we show the difference between the Hamiltonian constraint violations of the $O(v^4)$ and full extended versions of the data in the near-to-far transition for an equal-mass binary.

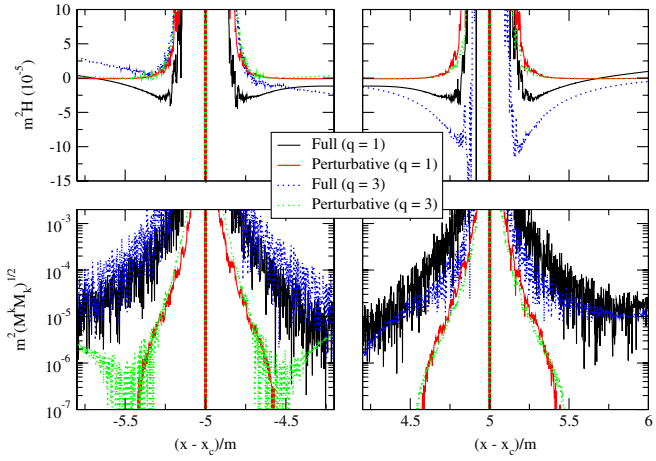

FIG. 17 (color online). The constraint violations of the versions of the inner zone metric with perturbative and full time dependence for binaries with $b = 10m$ and mass ratios of 1:1 and 3:1. We display these in the vicinity of both holes, which we shift in the 3:1 case, so their associated point particles lie at $x = \pm 5m$. [In the figure, $x_c := [1/(q+1) - 1/2]b$, $q := m_1/m_2$.]

effect are the ones in the coordinate transformation, not those in the tidal fields.)

It is also interesting to consider how accurate the data are for different mass ratios. One finds that the constraint violations do not behave quite as well as might be desired in the inner-to-near transition regions as one increases the mass ratio. This is shown in Figs. 19 and 20, which plot the Hamiltonian constraint and norm of the momentum constraint for mass ratios of 1:1, 3:1, 5:1, and 10:1. The worst behavior is that of the momentum constraint in the transition region near the more massive hole (hole 1), which increases as the mass of that hole increases. The Hamiltonian constraint also increases with mass ratio in the inner zones around both holes. (This is due to the inclusion of the full time dependence of the tidal fields—the inner zone constraint violations decrease with mass ratio if one only uses the version of the inner zone metric with perturbative time dependence.) The behavior of the other constraint violations is nonmonotonic. When one looks at the near-to-far transition and far zone proper, one finds much better behavior: The constraint violations decrease with increasing mass ratio in all of those regions, except for a slight increase in the momentum constraint violations in the far zone proper for unequal mass ratios. This is visible for a mass ratio of 3:1 in Fig. 16; we do not display the results for higher mass ratios, since they are not particularly interesting.

This behavior in the transition regions is primarily attributable to the choices we have made for the transition functions. For instance, it is possible to choose parameters, so the momentum constraint violations *decrease* around the more massive hole as its mass increases. This can be accomplished by taking $w_{\mathrm{inner},A} \propto r_A^T$, as in Papers I and II. However, with this choice, the decrease in momentum constraint violations around hole 1 occurs at the cost of

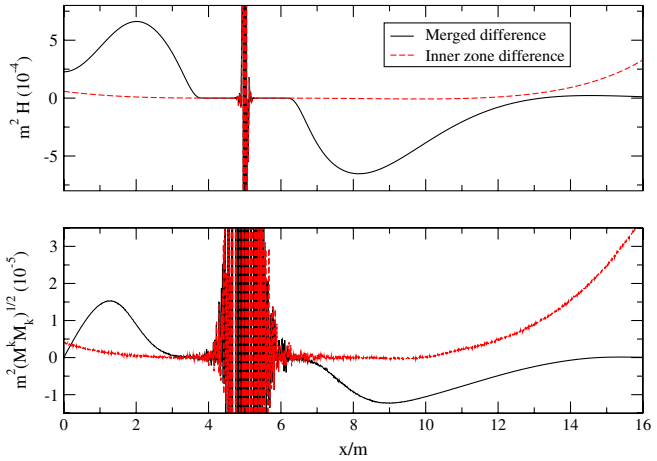

FIG. 18 (color online). The differences between the constraint violations of the version of the $O(v^4)$ data that omits the fourth-order octupole terms (O4_NOOCT) in the inner zone metric and the version including those terms (O4). We show them along the x axis near hole 1 for our standard test binary.

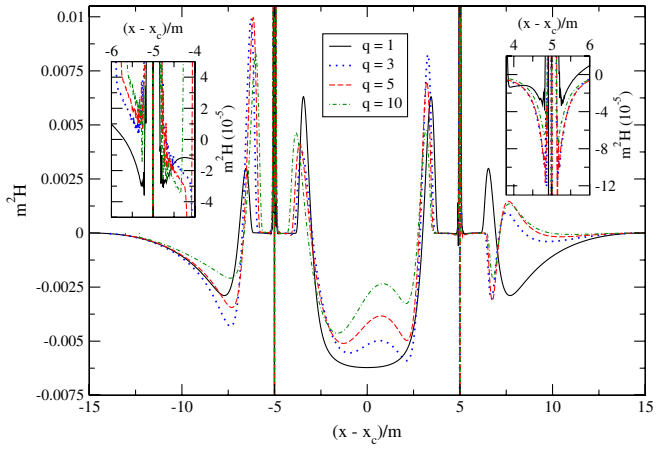

FIG. 19 (color online). The Hamiltonian constraint along the x axis for a binary with a separation of $10m$ and mass ratios of 1:1, 3:1, 5:1, and 10:1 ($q := m_1/m_2$). (The more massive hole—hole 1—is on the right, and the less massive hole—hole 2—is on the left.) For ease of comparison, we have shifted all of the data so the point midway between the two particles is at $x = 0$. [In the figure, $x_c := [1/(q+1) - 1/2]b$.] In the two insets, we zoom in to show how the inner zone metric's constraint violations vary with q, looking at the region around each hole in the inset closest to it.

the aforementioned extreme increase in constraint violations around hole 2 as its mass goes to zero. It should be possible to combine the two choices for $w_{\mathrm{inner},A}$ to obtain better behavior for unequal mass ratios, but we have chosen to leave such fine-tuning of transition functions to future work, contenting ourselves with providing examples of workable transition functions here.

It is instructive to compare our data's constraint violations with the constraint violations that occur in an evolu-

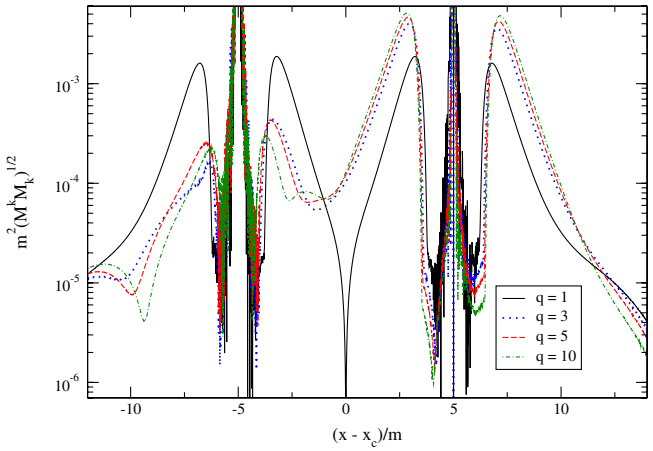

FIG. 20 (color online). The norm of the momentum constraint along the x axis for a binary with a separation of $10m$ and mass ratios of 1:1, 3:1, 5:1, and 10:1 ($q := m_1/m_2$). (The more massive hole—hole 1—is on the right, and the less massive hole—hole 2—is on the left.) For ease of comparison, we have shifted all of the data so the point midway between the two particles is at $x = 0$. [In the figure, $x_c := [1/(q+1) - 1/2]b$.]

tion of the data. Of course, one expects that the highly accurate simulations that will provide templates for parameter estimation with Advanced LIGO and LISA will have much smaller evolution-induced constraint violations than current simulations. (And, of course, the constraint violations do not themselves give an indication of the data's astrophysical realism.) However, current simulations' constraint violations give a convenient scale against which to compare the constraint violations of our data.

The evolution with which we will compare is the equal-mass nonspinning run from the set of 10 runs used in [30] to fix the spin coefficients. It starts at a coordinate separation of $\sim 6.79M$, where M is the binary's mass. (We use M since this mass is in general different from our data's PN mass, m.) The initial constraint violations in this evolution have a maximum magnitude (scaled by M^2) outside the apparent horizons of at least $\sim 10^{-5}$ for the Hamiltonian constraint and $\sim 5 \times 10^{-6}$ for the norm of the momentum constraint. After a quarter of an orbit, the constraint violations have already increased to $\sim 3 \times 10^{-4}$ for both the Hamiltonian constraint and the norm of the momentum constraint. The maximum Hamiltonian constraint violations (outside the apparent horizons) remain at about this level for the remainder of the evolution. The momentum constraint violations relax to smaller values as the evolution proceeds, with maxima (outside the apparent horizons) rapidly approaching $\sim 10^{-5}$.

N.B.: Since the apparent horizons were not located numerically in this evolution, we have simply excluded a ball of radius M about each hole. It appears that the apparent horizons of the individual black holes are roughly balls of coordinate radius $M/2$ in an equal-mass evolution with the same computational setup (see Fig. 12 in [95]), but we exclude more of the spacetime to err on the side of caution. We are thus only able to quote lower bounds on the maximum constraint violation outside the apparent horizons.

For an initial separation of $10m$ (which is, admittedly, larger than the comparison run's initial separation), the constraint violations of our data are smaller than the evolution-induced constraint violations in that run everywhere except in the inner-to-near transition, where they are much larger. See, e.g., the sup norms given in Table I, along with Figs. 12–14. Our data's constraint violations decrease rapidly with increasing separation in the inner-to-near transition, as is shown in the first two figures, and the momentum constraint violations become smaller than the maximal evolution-induced violations discussed above—indeed, close to the "equilibrium" value of $\sim 10^{-5}$—for an initial separation of $20m$. However, even for such a (relatively) large initial separation, our data's maximum Hamiltonian constraint violations are still $\sim 10^{-3}$, close to an order of magnitude larger than the maximum evolution-induced constraint violations seen in the run discussed above.

This is not unexpected, since we are only guaranteed that the constraint violations will decrease as $b^{-5/2}$, due to the uncontrolled remainders in our approximations. As we saw above, the constraint violations actually decrease much more rapidly than this everywhere except for the Hamiltonian constraint in the inner-to-near transition, where the maximum constraint violations (for the three initial separations we considered) are given roughly by $2b^{-5/2}$ (in units of m^{-2}). Thus, for the maximum constraint violations to be $\sim 3 \times 10^{-4}$, we would need an initial separation of $\sim 34m$. (This is not a completely unreasonable initial separation: It leads to a merger time that is ~ 24 times the longest binary black hole simulation to date, that of [8]. Moreover, it is still small enough that it is unlikely that simulations starting from that initial separation and using conformally flat initial data would be accurate enough to provide templates for parameter estimation with Advanced LIGO and LISA, since $v^4_{\text{initial}} \simeq 2 \times 10^{-3}$.)

IX. CONCLUSIONS

A. Summary

We have constructed approximate initial data for a nonspinning black hole binary in a quasicircular orbit. This data set has uncontrolled remainders of $O(v^5)$ throughout the time slice (including the far zone), along with remainders of $O(v^3[R/b]^4, v^5[R/b]^3)$ in the inner zone. We have verified the scaling of the uncontrolled remainders with v by checking that the constraint violations decrease at least as rapidly as they should when the binary's orbital separation is increased. We constructed this data set by asymptotically matching perturbed black hole metrics onto a PN metric and creating transition functions to smoothly interpolate between the various metrics. The resulting data do not assume conformal flatness and contain the binary's outgoing radiation in addition to the tidal deformations on the holes. (We have included the quadrupole deformations through 1PN along with the lowest-order octupole deformations.)

The results of the matching are given in Sec. V G and Eqs. (B1): Sec. V G gives directions for how to put together the coordinate transformation necessary to place the inner zone metric in the same coordinate system as the near zone metric (to the order we have matched). Equations in (B1) give explicit expressions for the tidal fields we obtained. [We also found that the inner and near zone mass parameters—i.e., M and m_1—agree through at least $O(v^3)$.] These tidal fields are then inserted into Detweiler's perturbed black hole metric, given in Cook-Scheel coordinates in Eqs. (3.2) and (3.3), to give the inner zone metric. The near and far zone metrics are given in Eqs. (4.1) and (6.4), respectively. We describe our method of computing the binary's past phase evolution, needed for the far zone metric, in Sec. VI A, and the specifics of how we put together the various zones' metrics in Appendix D.

Workable (though surely not optimal) transition functions that smoothly interpolate between the various zones' metrics are given in Sec. VIII B.

We have also constructed an extension of these data that is accurate through $O(v^5)$ in the near and far zones. Additionally, this extension includes the additional terms in the purely temporal component of the near zone metric that Blanchet, Faye, and Ponsot [61] give, as well as the matching terms in that component of the far zone metric. (We sketch the computation of these additional terms in Appendix C.) We also calculated the fourth-order octupole pieces of the tidal fields (and the associated piece of the coordinate transformation)—see Appendix B 2—and included them, as well. (The 1PN correction to the electric octupole tidal field is among the terms we calculated and add here.) Additionally, we calculated the full time dependence of the tidal fields (for times much less than the radiation reaction time scale) and included it in the inner zone metric. This is discussed in Appendices B 1 and D. See Table II (in Sec. VII) for an overview of the different versions of the metrics we considered in the paper. N.B.: While we did not include this in the table, for the sake of clarity, we considered all the versions of the near zone metrics with and without background resummation, displaying the resulting differences in the volume elements [for the $O(v^4)$ and full extended versions] in Fig. 5. We found the full extended (ALL) data set (including background resummation in the near zone) to be the best, overall, considering constraint violations as well as the inclusion of terms that we expect to improve evolutions.

In the process of obtaining these data, we have developed a method of fixing the matching parameters when matching a black hole onto a PN background that differs from that presented by Taylor and Poisson [75] and is more automatable. We have also obtained the 1PN corrections to the magnetic quadrupole and electric octupole for a circular orbit using this method, neither of which Taylor and Poisson computed.

The accurate description of the tidal deformations on the holes contained in these data should substantially reduce the high-frequency component of the initial spurious radiation; the use of a high-order PN metric should do the same for the low-frequency component. (The combination of the high-order PN metric, including accurate expressions for the trajectories, and the reduced junk radiation should also give a much better quasicircular orbit; see, e.g., [18,20].) If these data do indeed reduce the initial spurious radiation, then they can be used to directly quantify the effects of using the conformally flat initial data currently employed, as opposed to data that include many more of the system's expected physical properties. In addition, the waveforms generated using these data would be ideal for the construction of hybrid numerical relativity/post-Newtonian waveforms (as in [102]): Since the initial data are directly connected to the PN approximation, the PN parameters and phasing that are input into the initial data should accurately describe the subsequent evolution.

Of course, one needs to evolve the data to see whether these putative improvements are indeed realized. We have already coded this data set into MAPLE scripts, which were then converted to *C* code. Both the scripts and codes are freely available online at [39] to anyone who is interested in evolving or otherwise studying the data. Any evolutions of these data will need to use either excision [33,34] or the turducken approach [37]: The black hole perturbations are not valid all the way to the holes' asymptotically flat ends, preventing the use of standard puncture methods. Additionally, since the data only satisfy the constraint equations approximately, one may want to project them onto the constraint hypersurface before evolution. To do this, one would need to use a code such as [50,62,103,104]: The standard solver for puncture data [105] requires conformal flatness. However, evolutions of data that only approximately solve the constraints are possible; see, e.g., [60,64].

B. Possibilities for future initial data constructions with this method

With this work, the asymptotic matching method for generating initial data for nonspinning black hole binaries in a quasicircular orbit first essayed by Alvi [46], and further developed in Papers I and II, has been taken to the highest order possible without further development in its constituent parts: Including higher multipole orders in the inner zone would require the input of nonlinear black hole perturbation theory (the requisite calculation has now been carried out by Poisson and Vlasov [66]). Iterating to higher orders in v would not only require the higher multipoles, but also an explicit expression for the $O(v^6)$ pieces of the purely spatial components of the near zone metric. Determining the higher-order-in-v pieces of the far zone metric would either require calculation of further contributions from the outer integrals in the DIRE approach [72], or obtaining the far zone metric via matching, following the post-Minkowskian approach of [78].

Nevertheless, it might still be possible to improve the initial data at the (formal) order presented here, as was done in Paper II for the data in Paper I. For instance, one could contemplate converting the near zone metric to Cook-Scheel coordinates (or some other horizon-penetrating coordinate system) in a neighborhood of each black hole. This would regain the complete agreement between background coordinates, with no coordinate singularity at the horizon in the near zone metric, that was found to improve the numerical agreement of the metrics in Paper II. One could also further tweak the transition functions, though this is not likely to produce any dramatic improvements in constraint violations. However, it is possible that different choices for the transition functions could improve the data's properties in evolutions. For

instance, in the current near-to-far transition, the near zone metric is used (blended with the far zone metric) for $r \gg \lambda$, where its perturbative treatment of retardation leads to large phasing errors. It might thus be preferable to transition closer to the binary, even at the cost of greater constraint violations. (Resumming the far zone metric is a possibility for reducing these constraint violations, as was discussed briefly in Sec. VIII A.)

The prospects for generalizing this construction to include eccentricity or spin are good: The ingredients are nearly all readily available in the literature. Such a generalization—particularly the inclusion of spin—would be an obvious next step if this initial data set indeed significantly reduces the spurious radiation. Including eccentricity would be straightforward, though algebraically involved, and can be carried out with the ingredients we have used here, perhaps supplemented with the results from [75]. (The evolution of the binary's phase and separation needed in the far zone metric can be obtained through 3PN order using the results of [106].)

However, it would only be possible to obtain the generalization of these data for a spinning binary to $O(v^2)$, formally, while still including all the formal quadrupole pieces in the inner zone. This is true even though the generalization of Blanchet, Faye, and Ponsot's metric to include spin (and spin-orbit coupling) is available [107],[10] as are the expressions for the source multipoles necessary to obtain the matching far zone metric [109]. (The binary's evolution under radiation reaction is also known through 2.5PN [110].) The bottleneck is the available tidally perturbed Kerr metric [111], which only includes the quadrupole perturbations. We have seen that knowledge of the octupole perturbations is necessary to carry out the matching of all the formal quadrupole pieces at $O(v^4)$ [which one would need to do to obtain data that are formally valid through $O(v^3)$]. However, one could use the same philosophy we did when computing our extension and add the higher-order terms in the near and far zones without computing the matching inner zone terms.

ACKNOWLEDGMENTS

We would like to thank Luc Blanchet, Steven Detweiler, Lee Lindblom, Eric Poisson, Frans Pretorius, and Clifford Will for useful discussions and clarifications. Additionally, we owe special thanks to Erik Schnetter for giving us an invaluable outsider's perspective on the usability of our codes, thus helping us catch a few typos and correct some unclear exposition. We also wish to thank the anonymous referee for suggesting the plots of ψ_4. This work was supported by the Penn State Center for Gravitational Wave Physics under NSF cooperative agreement PHY-0114375, by NSF Grants No. PHY-0555628 and No. PHY-0855589 to Penn State, Grants No. PHY-0652874 and No. PHY-0855315 to FAU, and Grant No. PHY-0745779 to Princeton, as well as the Eberly research funds of Penn State.

APPENDIX A: COMPARING COOK-SCHEEL AND PN HARMONIC COORDINATES

In the quasi-Cartesian form of Cook-Scheel coordinates [67], the Schwarzschild metric is

$$g_{00}^{\mathrm{CS}} = -\frac{R-M}{R+M}, \qquad g_{0k}^{\mathrm{CS}} = \frac{4M^2}{(R+M)^2}\frac{X_k}{R},$$
$$g_{kl}^{\mathrm{CS}} = \left(1+\frac{M}{R}\right)^2\delta_{kl} + \frac{M^2}{R^2}\frac{R-M}{R+M}\left[1+\frac{4MR}{(R+M)^2}\right]\frac{X_kX_l}{R^2}. \tag{A1}$$

[The transformation from Schwarzschild to Cook-Scheel coordinates is given in Eq. (3.1).] For comparison, the Schwarzschild metric in PN harmonic coordinates is

$$g_{00}^{\mathrm{har}} = -\frac{R-M}{R+M},$$
$$g_{kl}^{\mathrm{har}} = \left(1+\frac{M}{R}\right)^2\left(\delta_{kl}-\frac{X_kX_l}{R^2}\right) + \frac{R+M}{R-M}\frac{X_kX_l}{R^2}, \tag{A2}$$

where $g_{0k}^{\mathrm{har}} = 0$. (One obtains PN harmonic coordinates from Schwarzschild coordinates by $R = \mathcal{P} - M$, where $\mathcal{P}$ is the Schwarzschild radial coordinate. This is just the spatial part of the Schwarzschild-to-Cook-Scheel transformation.) Obviously, these coordinates have preserved the coordinate singularity of the Schwarzschild metric in Schwarzschild coordinates.

Note that the purely temporal component of the Cook-Scheel version has the same form as in PN harmonic coordinates, but all of the other components are different. In particular, the Cook-Scheel version has nonzero spatiotemporal components as well as a slightly more involved nondiagonal piece of the spatial components. Explicitly, the differences between the PN harmonic and Cook-Scheel versions of the Schwarzschild metric components are

$$g_{00}^{\mathrm{CS}} - g_{00}^{\mathrm{har}} = 0, \qquad g_{0k}^{\mathrm{CS}} - g_{0k}^{\mathrm{har}} = \frac{4M^2}{(R+M)^2}\frac{X_k}{R},$$
$$g_{kl}^{\mathrm{CS}} - g_{kl}^{\mathrm{har}} = -\frac{16M^4}{(R-M)(R+M)^3}\frac{X_kX_l}{R^2}. \tag{A3}$$

(Of course, this must be interpreted purely algebraically, since we are subtracting components in different coordinate systems.) The difference of the purely spatial components scales as $O([M/R]^4)$ as $M/R \to 0$, which is clearly higher order in the near zone. However, the difference of the spatiotemporal components is $O([M/R]^2)$, which is of the same order as the terms we do keep in the spatial metric. And, indeed, the first term in this expansion appears in our coordinate transformation—see Sec. V G.

[10]Errata for the potentials and equations of motion in [107] are given in footnotes 6 and 7 of [108], respectively.

APPENDIX B: TIDAL FIELDS

1. Comparison with Taylor and Poisson's results

To facilitate the comparison of our expressions for the tidal fields with those obtained by Taylor and Poisson [75], we collect the results of our matching here. These include the results of the fourth-order octupole matching from the next subsection and are all put together using Eqs. (5.3) to give explicit expressions for the tidal fields about hole 1:

$$\mathcal{E}_{kl}(t) = \frac{m_2}{b^3}\left\{\left[1 - \frac{1}{2}\frac{m_2}{b}\right][\delta_{kl} - 3\hat{x}_k\hat{x}_l] + \frac{1}{2}\frac{m}{b}[4\hat{x}_k\hat{x}_l - 5\hat{y}_k\hat{y}_l + \hat{z}_k\hat{z}_l] - 6\sqrt{\frac{m}{b}}\frac{t}{b}\hat{x}_{(k}\hat{y}_{l)} + O\left(\left[\frac{m_2}{b}\right]^2, \frac{t^2}{b^2}\right)\right\}, \tag{B1a}$$

$$\mathcal{B}_{kl}(t) = \frac{m_2}{b^3}\sqrt{\frac{m_2}{b}}\left\{\left[-6\sqrt{\frac{m}{m_2}} + \frac{m_2}{b}\left\{5\left(\frac{m}{m_2}\right)^{3/2} + 7\sqrt{\frac{m}{m_2}} - 3\sqrt{\frac{m_2}{m}}\right\}\right]\hat{x}_{(k}\hat{z}_{l)} - 6\frac{m}{m_2}\sqrt{\frac{m_2}{b}}\frac{t}{b}\hat{y}_{(k}\hat{z}_{l)} + O\left(\left[\frac{m_2}{b}\right]^{3/2}, \frac{t^2}{b^2}\right)\right\}, \tag{B1b}$$

$$\mathcal{E}_{klp}(t) = \frac{m_2}{b^4}\left\{\left[1 - 3\frac{m_2}{b}\right][15\hat{x}_k\hat{x}_l\hat{x}_p - 9\delta_{(kl}\hat{x}_{p)}] - 3\frac{m}{b}[\hat{x}_k\hat{x}_l\hat{x}_p - 4\hat{y}_{(k}\hat{y}_l\hat{x}_{p)} + \hat{z}_{(k}\hat{z}_l\hat{x}_{p)}] + O\left(\left[\frac{m_2}{b}\right]^2, \frac{t}{b}\right)\right\}, \tag{B1c}$$

$$\mathcal{B}_{klp}(t) = \frac{9}{2}\frac{m_2}{b^4}\sqrt{\frac{m}{b}}\left\{5\hat{x}_{(k}\hat{x}_l\hat{z}_{p)} - \delta_{(kl}\hat{z}_{p)} + O\left(\left[\frac{m_2}{b}\right]^{1/2}, \frac{t}{b}\right)\right\}. \tag{B1d}$$

Here, for the purposes of comparison with Taylor and Poisson's results, we have included the time dependent pieces we know in the quadrupole fields (the time dependence falls into the uncontrolled remainders in the octupole fields). These are ordinarily contained in $\dot{\mathcal{E}}_{kl}$ and $\dot{\mathcal{B}}_{kl}$, since we usually treat them as independent tidal fields.

Taylor and Poisson give explicit expressions for the quadrupole tidal fields for a binary in a circular orbit in their Eqs. (1.10)–(1.14) [and with alternate notation in Eqs. (7.25)–(7.29)]. The parts of the quadrupole fields that Taylor and Poisson and we have both computed agree: These consist of the electric quadrupole (including its 1PN corrections), the time derivative of the electric quadrupole with no corrections, and the magnetic quadrupole with no corrections, all evaluated at $t = 0$. In fact, we can recover all of Taylor and Poisson's expressions for the tidal fields, including the full time dependence, if we evaluate our expressions for the tidal fields at $t = 0$ and then make the substitutions $\hat{x}_k \to \hat{x}_k \cos\omega t + \hat{y}_k \sin\omega t$ and $\hat{y}_k \to -\hat{x}_k \sin\omega t + \hat{y}_k \cos\omega t$. (This is, of course, only accurate for times much less than the radiation reaction time scale.) Thus, even though we are not given the full time dependence directly from the matching, we can obtain it from our results, since they are true for any point in the orbit.

While we have computed certain higher-order contributions to the tidal fields that Taylor and Poisson did not, we cannot improve upon the formal accuracy of their 1PN result for the tidal heating: The 2PN correction to the expression for the tidal heating involves the unknown 2PN correction to the electric quadrupole.

We can also check that the lowest-order pieces of all the tidal fields we found are the expected Newtonian ones: The Newtonian pieces of the tidal fields can be computed independently using Eqs. (5.45), (5.50), and (5.56) in [89], along with the obvious generalization of that reference's Eqs. (5.45) and (5.50) for the magnetic octupole, viz., $\mathcal{B}^{\rm Newt}_{klp} = -(3/8)\epsilon^{su}{}_{(k}\partial_{lp)s}\beta_u$, where β^k is given by Eq. (5.56b) of [89]. (To reproduce our results exactly, one needs to evaluate all of these expressions for the Newtonian parts of the tidal fields at $r_1 = 0$. Also, since these expressions for the Newtonian parts of the tidal fields are valid in the rest frame of hole 1, we need to use the relative velocity of the holes in calculating β^k.) Our expression for the 1PN correction to the magnetic quadrupole can be checked in the extreme mass-ratio limit against that computed by Poisson in [112]: This result is given in an appropriate form for comparison in an unnumbered equation in Sec. VII E of Taylor and Poisson [75] and agrees with our computation.

2. 1PN corrections to the fourth-order octupole fields

Even though we cannot obtain all the inner zone octupole pieces at fourth and fifth orders without including the hexadecapole fields (since these will give octupole contributions to the nonpolynomial part at these orders), it *is* possible to match only the polynomial parts, and, in doing so, to read off the 1PN corrections to the octupole tidal fields. As an illustration, we shall read off the 1PN correction to the electric octupole (along with the lowest-order piece of the time derivative of the magnetic quadrupole) by matching the octupole parts of the polynomial pieces at fourth order.

Except for the added algebraic complication of keeping higher-order multipole terms, this calculation proceeds precisely analogously to the fourth-order calculation involving the quadrupole-and-lower multipoles of the polynomial part in Sec. V F. The only subtlety that we should mention is one that was already present in our original fourth-order calculation. However, it was not a potential source of confusion there, because we were computing both the polynomial and nonpolynomial parts at once. Now that we want to compute the polynomial part by itself, we need to bear in mind that two nonpolynomial pieces can produce a polynomial piece when multiplied together (e.g., $\tilde{r}$ is a nonpolynomial piece, but $\tilde{r}^2$ is a polynomial piece). Therefore, contributions to the near zone metric involving terms such as $n_1^{(k}n_{12}^{l)}/S^2$ will contain polynomial pieces,

since n_1^k contains a factor of $1/\tilde{r}$, and $1/S^2$ contributes a factor of $\tilde{r}$. The final results are

$$(\dot{\bar{\mathcal{E}}}_{kl})_2 = 0, \qquad (\bar{\mathcal{E}}_{klp})_2 = 9[3\delta_{(kl}\hat{x}_{p)} - 5\hat{x}_k\hat{x}_l\hat{x}_p] - 3\frac{m}{m_2}[\hat{x}_k\hat{x}_l\hat{x}_p - 4\hat{y}_{(k}\hat{y}_l\hat{x}_{p)} + \hat{z}_{(k}\hat{z}_l\hat{x}_{p)}], \tag{B2a}$$

$$(\dot{\bar{\mathcal{B}}}_{kl})_1 = -6\frac{m}{m_2}\frac{1}{b}\hat{y}_{(k}\hat{z}_{l)}, \qquad (\bar{\mathcal{B}}_{klp})_1 = 0, \tag{B2b}$$

with an accompanying polynomial piece of the coordinate transformation of

$$\begin{aligned}(X^{\mathrm{P}}_{\alpha})_{4,3} = {} & \frac{\tilde{x}t}{b^3}\left\{\left[\frac{3}{2}\frac{m}{m_2} - 2\right]\tilde{x}^2 - \frac{m}{m_2}\frac{t^2}{6} + \left(\frac{3}{2} - \frac{9}{2}\frac{m}{m_2}\right)y^2 + \frac{1}{2}\left(1 - \frac{m}{m_2}\right)z^2\right\}\hat{t}_\alpha + \frac{1}{b^3}\left\{\left[\frac{m}{m_2}\left(\frac{t^2}{4} + \frac{\tilde{x}^2}{8} + y^2 - \frac{3}{2}z^2\right) + y^2 + z^2\right]\tilde{x}^2\right. \\ & \left. - \frac{m}{m_2}\left[\frac{t^4}{24} + \frac{y^4 - z^4}{8} + \frac{(y^2+z^2)t^2}{4}\right] - \frac{(y^2+z^2)^2}{4}\right\}\hat{x}_\alpha + \frac{\tilde{x}y}{b^3}\left\{3\tilde{x}^2 - \frac{9}{4}(y^2+z^2) + \frac{m}{m_2}\left[\frac{t^2}{2} - \frac{5}{2}\tilde{x}^2 + \frac{9}{4}y^2 + \frac{3}{4}z^2\right]\right\}\hat{y}_\alpha \\ & + \frac{\tilde{x}z}{b^3}\left\{3\tilde{x}^2 - \frac{9}{4}(y^2+z^2) + \frac{m}{m_2}\left[\frac{t^2}{2} - \frac{\tilde{x}^2}{2} + \frac{7}{4}y^2 + \frac{z^2}{4}\right]\right\}\hat{z}_\alpha.\end{aligned} \tag{B3}$$

Continuing on to fifth order to obtain the 1PN corrections to the magnetic octupole and time derivative of the electric quadrupole would be algebraically more complicated, but would otherwise proceed as above. At sixth order, we are not so fortunate. If we tried to carry out even the quadrupole part of the sixth order polynomial matching, so as, e.g., to read off the 2PN correction to the electric quadrupole, we would be stymied by our lack of knowledge of $(X^{\mathrm{NP}}_{\alpha})_{4,3}$: The $\tilde{r}$-times-a-polynomial-in-$\tilde{x}^\alpha$ pieces of $(X^{\mathrm{NP}}_{\alpha})_{4,3}$ (which we expect to be present, as there have been such terms at all lower multipole orders) will contribute to $(h^{\mathrm{P}}_{\alpha\beta})_6$ via the $b(1/R)_4$ term.

APPENDIX C: EXTENDED FAR ZONE METRIC

As discussed in Sec. VII, we were not able to use all of the PN near zone metric provided by Blanchet, Faye, and Ponsot [61] in our matching, but chose to include the higher-order terms [viz., the $O(v^6)$ and $O(v^7)$ terms in g_{00} and the $O(v^6)$ terms in g_{0k}] in an extension to our data. Here, we describe how we obtain the matching additional terms in the far zone, following Pati and Will [72,73], as in Sec. VI.

The requisite ingredients are nearly all readily available, and the ones that are not are almost all quite easily calculable: We need to know how to obtain the metric from the metric perturbation, and the expression Pati and Will give for this [in, e.g., Eqs. (4.2) of [72]] is of sufficiently high order for our purposes. We also need to know how to obtain the metric perturbation by differentiating multipoles: Here, we need to add on to Pati and Will's result [reproduced in our Eq. (6.1)] by computing the $O(v^6)$ and $O(v^7)$ pieces of h^{00}, which are

$$\frac{1}{6}\partial_{klps}\left[\frac{\mathcal{I}^{klps}(u)}{r}\right] - \frac{1}{30}\partial_{klpsv}\left[\frac{\mathcal{I}^{klpsv}(u)}{r}\right], \tag{C1}$$

and the $O(v^6)$ pieces of h^{0k}, which are

$$-\frac{1}{6}\partial_{lps}\left[\frac{\dot{\mathcal{I}}^{klps}(u)}{r}\right] + \frac{1}{2}\epsilon^{lkp}\partial_{psv}\left[\frac{\mathcal{J}^{lsv}(u)}{r}\right]. \tag{C2}$$

These were obtained by substituting the expressions for M^Q (in terms of $\mathcal{I}^Q$ and $\mathcal{J}^Q$) from Pati and Will's Eqs. (4.7) into their Eq. (2.13) (both from [72]). (Recall that Q is a multi-index.)

In these expressions, we have omitted the nonlinear terms arising from the outer integral. While it would be, in principle, reasonably straightforward to compute them, following the procedure given by Pati and Will [72], the calculation would be involved enough that we do not attempt it here. In fact, if we change our order counting to the strict Pati-Will order counting [i.e., disregarding post-Minkowskian powers of G, so *all* powers of $1/r$ after the first are counted as $O(v)$], then we can ignore the unknown outer integral term that would contribute to g_{0k} at $O(v^6)$ if we used the order counting we used in the $O(v^4)$ version of the data (detailed in Sec VI): This term comes from the first term of Eq. (4.4b) in [72],[11] and looks, schematically, like $\mathcal{I}\mathcal{J}^k/r^3$, which is $O(v^7)$ with the strict Pati-Will order counting. This new order counting does not cause us to drop any of the outer integral terms that we were previously keeping, and with it, we have consistent $O(v^5)$ initial data in both the near and far zones.

However, even with the new order counting, there are still some unknown $O(v^7)$ outer integral terms in h^{00}, e.g., ones that look like $\mathcal{I}\ddot{\mathcal{I}}^{kl}\hat{n}^{\langle kl\rangle}/r^2$ [see Eq. (6.5a) in [72]]. We shall simply neglect these terms here: Since we are adding the $O(v^7)$ terms to the initial data without regard to formal accuracy, it does not make sense to go to the trouble of

[11] It is not present in the more specific expression Pati and Will give in Eq. (6.5b) of [72], because they have specialized that expression—using their "quick and dirty" rule—to look at contributions to the near zone, where this term does not contribute until a much higher order than they are considering.

calculating the $O(v^7)$ outer integral terms. This is particularly true since we are not even sure that we have all the terms we need in the 1PN correction to the mass octupole, as we shall discuss below.

Finally, we need expressions for all of the source multipoles, to the appropriate PN order: We need I to 2PN, which we can obtain from the expression Blanchet gives for the system's binding energy in Eq. (170) of [41] (to which we add the mass of the point particles to get I). We also need $\mathcal{J}^k$, I^{kl}, and I^{klp} to 1PN. The first of these can be obtained from the expression Kidder, Will, and Wiseman give for the system's angular momentum in Eq. (2.13b) of [113]. The second is given in Eq. (6.2c). However, the third has to be obtained from the three-index Epstein-Wagoner (EW) moment $I^{klp}_{\rm EW}$, given in, e.g., Eq. (6.6b) in Will and Wiseman [74]: The result is $I^{klp} = m_1 x_1^{klp}(1 + v_1^2/2 - m_2/2b) + (1 \leftrightarrow 2) + O(v^4)$, up to possible terms of the form $m_1^2 b \delta^{(kl} x_1^{p)} + (1 \leftrightarrow 2)$. The caveat is due to Will and Wiseman's omission of the terms in $I^{klp}_{\rm EW}$ that are pure traces in the first two indices (since they were just interested in computing the waveform, which is trace-free). Fortunately, we do not need to know the 1PN correction to I^{klp} to obtain consistent $O(v^5)$ data, though it is necessary to obtain the even higher-order terms we include in the purely temporal component of the far zone metric.

The given expression for I^{klp} comes from the relation $\dot{I}^{klp} = 3I^{(klp)}_{\rm EW}$, which itself comes from taking a time derivative of the definition of I^{klp} [given in, e.g., Eq. (4.5b) in [72]], using the conservation law $\partial_\beta \tau^{\alpha\beta} = 0$ to write $\partial_0 \tau^{\alpha 0} = -\partial_k \tau^{\alpha k}$, and integrating the result by parts. The result is an expression that equals $3I^{(klp)}_{\rm EW}$ up to surface terms [see the definition of $I^{klp}_{\rm EW}$ in Eq. (2.19b) of [74]]. To obtain the given result for I^{klp}, we merely antidifferentiate $3I^{(klp)}_{\rm EW}$ with respect to t. We have to worry about missing terms that are constant in time (up to radiative effects) when doing this, but it turns out that any such terms are zero for a circular orbit. This follows from considering all possible constant-in-time 1PN contributions to I^{klp} and finding that they vanish for a circular orbit, because $\vec{A}$, the Laplace-Runge-Lenz vector, does. (The only other vectorial Newtonian constant of the motion is the binary's angular momentum, and that cannot contribute to I^{klp} at 1PN since it is odd under time reversal, while I^{klp} is even.)

Finally, we need $\mathcal{J}^{klp}$, I^{klps}, and I^{klpsv} to Newtonian order: These can be obtained from Eq. (D1) in [73]. With all of these ingredients, we can put together the far zone metric in the same way as we did in Sec. VI. We thus obtain its various components to the same order as we are keeping the near zone metric (with the above caveats about missing terms), viz., with uncontrolled remainders of $O(v^8)$ in the purely temporal component, $O(v^7)$ in the spatiotemporal components, and $O(v^6)$ in the purely spatial components.

APPENDIX D: COMPUTATION OF THE METRICS

Here, we detail exactly how the metrics are computed in the MAPLE scripts that were used (along with BAM) to compute the constraint violations and create the plots. The scripts themselves and the resulting C code (based on MAPLE's C output) are available online at [39].

1. Inner zone

To compute the inner zone metric around hole 1, we substitute in the tidal fields given in Eq. (B1) into the expression for Detweiler's perturbed Schwarzschild metric in Cook-Scheel coordinates that we give in Eqs. (3.2) and (3.3), taking $M = m_1$. We then transform using the coordinate transformation given in Sec. V G. The resulting metric thus includes terms through $O(v^5)$ all components, though, as discussed in Sec. I C 1, initial data derived from this metric will only have a formal accuracy of $O(v^4)$. We also do not perform any expansions after substituting the tidal fields and performing the coordinate transformation, so the final, transformed metric also contains various other higher-order-in-v terms. The inner zone metric around hole 2 is obtained by the same procedure, along with the transformations detailed at the beginning of Sec. V A.

We have considered three versions of the inner zone metric: The first version (contained in O4_NOOCT) comes directly from the matching performed in Sec. V and only contains the pieces that we were able to match onto the near zone metric while including all of the multipolar contributions at a given order [i.e., up to octupole order through $O(v^3)$ and then only up to quadrupole order through $O(v^5)$]. The second version (contained in O4) also incorporates the results of the fourth-order octupole matching carried out in Appendix B 2—this includes the 1PN correction to the electric octupole, but only the polynomial part of the accompanying coordinate transformation. The third version (contained in O5 and ALL) adds on the time dependence of all of the tidal fields (for a circular orbit), obtained in the manner described in Appendix B 1, though it still uses the same coordinate transformation as before. (We use the 1PN expression for ω when substituting for the unit vectors in obtaining the full time dependence. We leave off the known higher-order corrections to ω here, since the expressions for the tidal fields we obtained by matching came from using the 1PN version of ω.)

We calculate the third version by substituting $T\dot{\mathcal{E}}_{kl} \to (T - t)\dot{\mathcal{E}}_{kl}(0)$ and similarly for $\dot{\mathcal{C}}_{klp}$ in Eqs. (3.2) and (3.3) before substituting in the tidal fields (with full time dependence). These substitutions are necessary, because the $T\dot{\mathcal{E}}_{kl}$ and $T\dot{\mathcal{C}}_{klp}$ terms in Eqs. (3.2) and (3.3) come from the expansions of $\mathcal{E}_{kl}$ and $\mathcal{C}_{klp}$ (with full dependence on V, the ingoing Eddington-Finkelstein coordinate) about $V = 0$. We, however, are only including the full time dependence on t, the near zone time coordinate, in the tidal fields,

due to our method of obtaining this dependence. These expressions will thus only contain the $t\dot{\mathcal{E}}_{kl}$ and $t\dot{\mathcal{C}}_{klp}$ pieces (when expanded about $t = 0$), so we make the above substitutions to retain the linear T dependence given by the matching while not including the linear t dependence twice. (We experimented with including the full time dependence of the tidal fields using T instead of t and found that the constraint violations increased.)

This method of computing the metric deliberately does not include the effects of the full time dependence on the spatial variation of the tidal fields' contributions to the metric [due to their dependence on V; see the discussion following Eq. (3.3)], since these would enter at the same order as the unknown time derivatives of the tidal fields (second derivatives of the quadrupole fields, and first derivatives of the octupole fields). Of course, the terms we are keeping are higher order as well, but since they would enter with explicit factors of t in the multipole expansion, they would not be entangled with the explicit appearances of unknown time derivatives. (This follows because the Schwarzschild metric is time independent in the coordinates we use.) What we have done is equivalent to repeating the matching we have performed at each value of (near zone time) t, up to orbital shrinkage effects, which are higher order than the terms we are considering here. (We also have not attempted to include the full time dependence of the coordinate transformation for the reasons discussed in Sec. VII.)

2. Near zone

We compute the near zone metric by substituting the trajectories for the point particles [obtained in the manner discussed in Sec. VI A] into Blanchet, Faye, and Ponsot's metric [given in Eqs. (7.2) of [61]], including the background resummation given in Sec. VIII A. Here, there are, again, three versions of the metric, one giving $O(v^4)$ data, one $O(v^5)$ data, and one containing the complete 2.5PN metric.[12] N.B.: In order to perform background resummation on the purely temporal component of the complete 2.5PN metric, one needs to also subtract the $O([m_1/r_1]^3)$ portion of the expansion of the background, viz., $2m_1^3/r_1^3$, in Eq. (8.2). All of these versions are constructed by truncating the metric components to the desired order before substituting in the trajectories. No expansions are performed after that substitution, since we do not want to drop the higher-order terms that we are keeping in the trajectories (discussed in Sec. VI A) for conformity with the far zone metric. Because of an oversight, we did not include the 3PN corrections to the relative-to-COM relation in the $O(v^4)$ version of the near zone metric used to obtain the plots given in this paper, but have included them in the version available online at [39].

3. Far zone

The calculation of the far zone metric follows the DIRE approach, detailed in Sec. VI, differentiating multipole moments to obtain the metric. We have the same three versions of the far zone metric as for the near zone metric and obtain them in the same manner: We expand to the desired order after performing all of the substitutions except for ϕ, ω, and b (i.e., the contributions that vary due to secular radiation reaction effects and are discussed in Sec. VI A). We also do not include any of the terms due to derivatives acting on b: These would give nonzero contributions, due to the separation's retarded time dependence from orbital shrinkage, but these terms are quite small, both formally and practically—unlike those due to the radiation reaction effects in the phase or undifferentiated separation—so we neglect them. [For instance, the lowest-order contribution due to the nonzero time derivative of b in the $\partial_{kl}[\mathcal{I}^{kl}(u)/r]$ contribution to g_{00} is formally $O(v^9)$. It is also numerically small: The largest contribution has a magnitude of $\sim 10^{-7}$ when evaluated at the intersection of the x axis and the inner boundary of the near-to-far transition for our equal-mass test binary, viz., $x \simeq 20m$; see Sec. VIII B. For comparison, the contribution of the uncorrected $(m_1/r)v_1^2 + (1 \leftrightarrow 2)$ term in that situation is $\sim 10^{-4}$.]

The $O(v^4)$ version uses a slightly different order counting than the $O(v^5)$ and full extended versions. As discussed in Sec. VI, we choose to keep the outer integral terms—here, these are the terms that look like $(m/r)^2$—in the $O(v^4)$ data due to post-Minkowskian considerations, even though those terms are $O(v^5)$ if one interprets the Pati-Will order counting strictly. However, as mentioned in Appendix C, we do not know any of the higher-order outer integral terms, so we simply drop them [using the strict Pati-Will order counting to justify doing so in the $O(v^5)$ data].

[12] Recall that one needs all of the components through $O(v^4)$ [resp. $O(v^5)$] in addition to the $O(v^5)$ [resp. $O(v^6)$] terms in the spatiotemporal components in order to obtain $O(v^4)$ [resp. $O(v^5)$] data.

[1] F. Pretorius, Phys. Rev. Lett. **95**, 121101 (2005).
[2] M. Campanelli, C. O. Lousto, P. Marronetti, and Y. Zlochower, Phys. Rev. Lett. **96**, 111101 (2006).
[3] J. G. Baker, J. Centrella, D.-I. Choi, M. Koppitz, and J. van Meter, Phys. Rev. Lett. **96**, 111102 (2006).
[4] F. Pretorius, in *Physics of Relativistic Objects in Compact*

Binaries: From Birth to Coalescence, edited by M. Colpi, P. Casella, V. Gorini, U. Moschella, and A. Possenti (Springer-Verlag, Berlin, 2009).
[5] J. G. Baker, W. D. Boggs, J. Centrella, B. J. Kelly, S. T. McWilliams, and J. R. van Meter, Phys. Rev. D **78**, 044046 (2008).
[6] J. A. González, U. Sperhake, and B. Brügmann, Phys. Rev. D **79**, 124006 (2009).
[7] E. Berti, V. Cardoso, J. A. Gonzalez, U. Sperhake, M. Hannam, S. Husa, and B. Brügmann, Phys. Rev. D **76**, 064034 (2007).
[8] M. A. Scheel, M. Boyle, T. Chu, L. E. Kidder, K. D. Matthews, and H. P. Pfeiffer, Phys. Rev. D **79**, 024003 (2009).
[9] S. Husa, J. A. González, M. Hannam, B. Brügmann, and U. Sperhake, Classical Quantum Gravity **25**, 105006 (2008).
[10] B. P. Abbott *et al.* (LIGO Scientific Collaboration), Rep. Prog. Phys. **72**, 076901 (2009).
[11] L. Lindblom, B. J. Owen, and D. A. Brown, Phys. Rev. D **78**, 124020 (2008).
[12] P. Bender *et al.*, Report No. ESA-SCI, 11, 2000, http://www.srl.caltech.edu/lisa/documents/sts_1.05.pdf.
[13] M. Hannam *et al.*, Phys. Rev. D **79**, 084025 (2009).
[14] B. Aylott *et al.*, Classical Quantum Gravity **26**, 165008 (2009).
[15] M. Boyle, D. A. Brown, L. E. Kidder, A. H. Mroué, H. P. Pfeiffer, M. A. Scheel, G. B. Cook, and S. A. Teukolsky, Phys. Rev. D **76**, 124038 (2007).
[16] L. Lindblom, Phys. Rev. D **80**, 064019 (2009).
[17] H. P. Pfeiffer, D. A. Brown, L. E. Kidder, L. Lindblom, G. Lovelace, and M. A. Scheel, Classical Quantum Gravity **24**, S59 (2007).
[18] S. Husa, M. Hannam, J. A. González, U. Sperhake, and B. Brügmann, Phys. Rev. D **77**, 044037 (2008).
[19] B. Walther, B. Brügmann, and D. Müller, Phys. Rev. D **79**, 124040 (2009).
[20] T. Bode, D. Shoemaker, F. Herrmann, and I. Hinder, Phys. Rev. D **77**, 044027 (2008).
[21] J. A. González, U. Sperhake, B. Brügmann, M. Hannam, and S. Husa, Phys. Rev. Lett. **98**, 091101 (2007).
[22] G. Lovelace, Y. Chen, M. Cohen, J. D. Kaplan, D. Keppel, K. D. Matthews, D. A. Nichols, M. A. Scheel, and U. Sperhake, arXiv:0907.0869 [Phys. Rev. D (unpublished)].
[23] T. Chu, H. P. Pfeiffer, and M. A. Scheel, arXiv:0909.1313.
[24] G. B. Cook, Living Rev. Relativity **3**, 5 (2000), http://www.livingreviews.org/lrr-2000-5.
[25] E. Gourgoulhon, J. Phys. Conf. Ser. **91**, 012001 (2007).
[26] S. Brandt and B. Brügmann, Phys. Rev. Lett. **78**, 3606 (1997).
[27] P. Marronetti, W. Tichy, B. Brügmann, J. González, M. Hannam, S. Husa, and U. Sperhake, Classical Quantum Gravity **24**, S43 (2007).
[28] P. Marronetti, W. Tichy, B. Brügmann, J. González, and U. Sperhake, Phys. Rev. D **77**, 064010 (2008).
[29] W. Tichy and P. Marronetti, Phys. Rev. D **76**, 061502(R) (2007).
[30] W. Tichy and P. Marronetti, Phys. Rev. D **78**, 081501(R) (2008).
[31] W. Tichy, B. Brügmann, and P. Laguna, Phys. Rev. D **68**, 064008 (2003).
[32] W. Tichy and B. Brügmann, Phys. Rev. D **69**, 024006 (2004).
[33] M. A. Scheel, H. P. Pfeiffer, L. Lindblom, L. E. Kidder, O. Rinne, and S. A. Teukolsky, Phys. Rev. D **74**, 104006 (2006).
[34] D. Shoemaker, K. Smith, U. Sperhake, P. Laguna, E. Schnetter, and D. Fiske, Classical Quantum Gravity **20**, 3729 (2003).
[35] G. B. Cook and H. P. Pfeiffer, Phys. Rev. D **70**, 104016 (2004).
[36] A. Ashtekar and B. Krishnan, Living Rev. Relativity **7**, 10 (2004), http://www.livingreviews.org/lrr-2004-10.
[37] D. Brown, O. Sarbach, E. Schnetter, M. Tiglio, P. Diener, I. Hawke, and D. Pollney, Phys. Rev. D **76**, 081503(R) (2007).
[38] N. Yunes, Classical Quantum Gravity **24**, 4313 (2007).
[39] See EPAPS Document No. E-PRVDAQ-80-080922 for the MAPLE scripts and *C* codes that generate the data. For more information on EPAPS, see http://www.aip.org/pubservs/epaps.html.
[40] L. E. Simone, S. W. Leonard, E. Poisson, and C. M. Will, Classical Quantum Gravity **14**, 237 (1997).
[41] L. Blanchet, Living Rev. Relativity **9**, 4 (2006), http://www.livingreviews.org/lrr-2006-4.
[42] N. Yunes, W. Tichy, B. J. Owen, and B. Brügmann, Phys. Rev. D **74**, 104011 (2006).
[43] N. Yunes and W. Tichy, Phys. Rev. D **74**, 064013 (2006).
[44] A. Garat and R. H. Price, Phys. Rev. D **61**, 124011 (2000).
[45] J. A. Valiente Kroon, Classical Quantum Gravity **21**, 3237 (2004).
[46] K. Alvi, Phys. Rev. D **61**, 124013 (2000).
[47] S. Nissanke, Phys. Rev. D **73**, 124002 (2006).
[48] B. J. Kelly, W. Tichy, M. Campanelli, and B. F. Whiting, Phys. Rev. D **76**, 024008 (2007).
[49] L. Blanchet, Phys. Rev. D **68**, 084002 (2003).
[50] W. Tichy, B. Brügmann, M. Campanelli, and P. Diener, Phys. Rev. D **67**, 064008 (2003).
[51] G. Lovelace, Classical Quantum Gravity **26**, 114002 (2009).
[52] G. Lovelace, R. Owen, H. P. Pfeiffer, and T. Chu, Phys. Rev. D **78**, 084017 (2008).
[53] R. A. Matzner, M. F. Huq, and D. Shoemaker, Phys. Rev. D **59**, 024015 (1998).
[54] P. Marronetti and R. A. Matzner, Phys. Rev. Lett. **85**, 5500 (2000).
[55] P. Marronetti, M. Huq, P. Laguna, L. Lehner, R. A. Matzner, and D. Shoemaker, Phys. Rev. D **62**, 024017 (2000).
[56] U. Sperhake, Phys. Rev. D **76**, 104015 (2007).
[57] M. Hannam, S. Husa, B. Brügmann, J. A. González, and U. Sperhake, Classical Quantum Gravity **24**, S15 (2007).
[58] H. P. Pfeiffer, G. B. Cook, and S. A. Teukolsky, Phys. Rev. D **66**, 024047 (2002).
[59] H.-J. Yo, J. N. Cook, S. L. Shapiro, and T. W. Baumgarte, Phys. Rev. D **70**, 084033 (2004).
[60] B. J. Kelly, W. Tichy, Y. Zlochower, M. Campanelli, and B. F. Whiting (unpublished).
[61] L. Blanchet, G. Faye, and B. Ponsot, Phys. Rev. D **58**, 124002 (1998).
[62] H. P. Pfeiffer, L. E. Kidder, M. A. Scheel, and S. A. Teukolsky, Comput. Phys. Commun. **152**, 253 (2003).

[63] M. Holst, L. Lindblom, R. Owen, H. P. Pfeiffer, M. A. Scheel, and L. E. Kidder, Phys. Rev. D **70**, 084017 (2004).
[64] T. Bode, P. Laguna, D. M. Shoemaker, I. Hinder, F. Herrmann, and B. Vaishnav, Phys. Rev. D **80**, 024008 (2009).
[65] N. Jansen and B. Brügmann (unpublished).
[66] E. Poisson and I. Vlasov, arXiv:0910.4311.
[67] G. B. Cook and M. A. Scheel, Phys. Rev. D **56**, 4775 (1997).
[68] S. Detweiler, Classical Quantum Gravity **22**, S681 (2005).
[69] E. Poisson, Phys. Rev. Lett. **94**, 161103 (2005).
[70] K. S. Thorne and J. B. Hartle, Phys. Rev. D **31**, 1815 (1985).
[71] X.-H. Zhang, Phys. Rev. D **34**, 991 (1986).
[72] M. E. Pati and C. M. Will, Phys. Rev. D **62**, 124015 (2000).
[73] M. E. Pati and C. M. Will, Phys. Rev. D **65**, 104008 (2002).
[74] C. M. Will and A. G. Wiseman, Phys. Rev. D **54**, 4813 (1996).
[75] S. Taylor and E. Poisson, Phys. Rev. D **78**, 084016 (2008).
[76] P. Musgrave, D. Pollney, and K. Lake, computer code GRTENSORII (1996), http://grtensor.phy.queensu.ca/.
[77] C. M. Bender and S. A. Orszag, *Advanced Mathematical Methods for Scientists and Engineers* (McGraw-Hill, New York, 1978).
[78] O. Poujade and L. Blanchet, Phys. Rev. D **65**, 124020 (2002).
[79] S. Detweiler (private communication).
[80] R. Rieth, in *Mathematics of Gravitation. Part II: Gravitational Wave Detection*, edited by A. Królak, Banach Center Publications Vol. 41 (Polish Academy of Sciences, Institute of Mathematics, Warsaw, 1997), pp. 71–74, nearly identical to arXiv:gr-qc/9603043.
[81] T. Damour, P. Jaranowski, and G. Schäfer, Phys. Rev. D **62**, 084011 (2000).
[82] J. A. Isenberg, Int. J. Mod. Phys. D **17**, 265 (2008).
[83] J. R. Wilson, G. J. Mathews, and P. Marronetti, Phys. Rev. D **54**, 1317 (1996).
[84] H. Stephani, D. Kramer, M. MacCallum, C. Hoenselaers, and E. Herlt, *Exact Solutions of Einstein's Field Equations* (Cambridge University Press, Cambridge, United Kingdom, 2003), 2nd ed.
[85] J. A. Schouten, *Ricci-Calculus: An Introduction to Tensor Analysis and its Geometrical Applications* (Springer-Verlag, Berlin, 1954), 2nd ed.
[86] L. Blanchet (private communication).
[87] G. Schäfer, Ann. Phys. (N.Y.) **161**, 81 (1985).
[88] L. Blanchet, Phys. Rev. D **47**, 4392 (1993).
[89] J. B. Hartle, K. S. Thorne, and R. H. Price, in *Black Holes: The Membrane Paradigm*, edited by K. S. Thorne, R. H. Price, and D. A. Macdonald (Yale University Press, New Haven, CT, 1986).
[90] N. Straumann, *General Relativity: With Applications to Astrophysics* (Springer-Verlag, Berlin, 2004), rev. ed.
[91] L. Blanchet and T. Damour, Ann. Inst. Henri Poincaré Phys. Théor. **50**, 377 (1989).
[92] S. Weinberg, *Gravitation and Cosmology: Principles and Applications of the General Theory of Relativity* (Wiley, New York, 1972).
[93] T. Damour, B. R. Iyer, and B. S. Sathyaprakash, Phys. Rev. D **63**, 044023 (2001).
[94] L. Blanchet and B. R. Iyer, Classical Quantum Gravity **20**, 755 (2003).
[95] B. Brügmann, J. A. González, M. Hannam, S. Husa, U. Sperhake, and W. Tichy, Phys. Rev. D **77**, 024027 (2008).
[96] B. Brügmann, W. Tichy, and N. Jansen, Phys. Rev. Lett. **92**, 211101 (2004).
[97] T. Damour, Int. J. Mod. Phys. A **23**, 1130 (2008).
[98] J. D. Jackson, *Classical Electrodynamics* (Wiley, New York, 1999), 3rd ed.
[99] J. Pullin (private communication).
[100] I. Vega, P. Diener, W. Tichy, and S. Detweiler, Phys. Rev. D **80**, 084021 (2009).
[101] E. Schnetter (private communication).
[102] P. Ajith *et al.*, Classical Quantum Gravity **24**, S689 (2007).
[103] W. Tichy, Classical Quantum Gravity **26**, 175018 (2009).
[104] F. Pretorius (unpublished).
[105] M. Ansorg, B. Brügmann, and W. Tichy, Phys. Rev. D **70**, 064011 (2004).
[106] K. G. Arun, L. Blanchet, B. R. Iyer, and S. Sinha, Phys. Rev. D **80**, 124018 (2009).
[107] H. Tagoshi, A. Ohashi, and B. J. Owen, Phys. Rev. D **63**, 044006 (2001).
[108] G. Faye, L. Blanchet, and A. Buonanno, Phys. Rev. D **74**, 104033 (2006).
[109] C. M. Will, Phys. Rev. D **71**, 084027 (2005).
[110] L. Blanchet, A. Buonanno, and G. Faye, Phys. Rev. D **74**, 104034 (2006); **75**, 049903(E) (2007).
[111] N. Yunes and J. A. González, Phys. Rev. D **73**, 024010 (2006).
[112] E. Poisson, Phys. Rev. D **70**, 084044 (2004).
[113] L. E. Kidder, C. M. Will, and A. G. Wiseman, Phys. Rev. D **47**, 3281 (1993).